COAL-BASED CARBON QUANTUM DOTS SYNTHESIS SIMULATION

SIMULATION OF THE EFFECT OF SHEAR STRESS ON COAL PARTICLE IN THE PREPARATION OF COAL-BASED CARBON QUANTUM DOTS BY BALL MILLING

By LU (SONIA) TAI, B.A.

A Thesis Submitted to the School of Graduate Studies in Partial Fulfilment of the
Requirements for the Degree Master of Applied Science

McMaster University MASTER OF APPLIED SCIENCE (2024) Hamilton, Ontario

Department of Materials Science and Engineering, Engineering Graduate Program

TITLE: Simulation of the Effect of Shear Stress on Coal Particle in the Preparation of Coal-based Carbon Quantum Dots by Ball Milling

AUTHOR: Lu (Sonia) Tai, B.A. (Beijing Jiaotong University, University of Waterloo)

SUPERVISOR: Professor Gu Xu

NUMBER OF PAGES: xiv, 114

Abstract

Since carbon quantum dots were discovered in 2004, they have received significant attention. So far, the synthesis and applications of carbon quantum dots are still in the early stage of development. Among the synthesis methods, ball milling garnered widespread attention. However, there is controversy regarding whether ball milling can be employed for large-scale production of carbon quantum dots from coal. Whether van der Waals bonds between graphite layers in coal particles can be broken during ball milling is the key to the feasibility of using ball milling to synthesize coal-based carbon quantum dots. Therefore, in this study, we simulated this microscopic process with a two-dimensional model. After applying shear stress, the proportions of broken van der Waals bonds in anthracite and bituminous coal particles were found to be 53.26% and 74.55% at 2500th iterations, respectively. The graphite layers in anthracite coal particles could not be exfoliated sufficiently due to the larger size of graphite layers in anthracite coal compared to that of bituminous coal. This study explores the feasibility of preparing carbon quantum dots from coal by ball milling and offers guidance for the selection of raw materials.

Acknowledgement

I would like to express my heartfelt gratitude to my supervisor Professor Gu Xu for his exceptional academic expertise and the invaluable support he has provided throughout my graduate studies. Professor Xu has been a source of inspiration, offering valuable guidance and assistance not only in academic matters but also in personal challenges. His support has played an indispensable role in my academic and personal growth.

Furthermore, I would like to extend my appreciation to my committee members and all the other staff members and professors who have supported me in various ways throughout the process of completing this thesis. Their guidance and assistance have been instrumental in the completion of this work.

Finally, I am also sincerely thankful to my colleagues, Dr. Ryan T. Wang, Dr. Alex F. Xu, and Kelly Q. Wang, for their invaluable contributions and collaboration. Despite their busy schedules, they have always been willing to lend a helping hand and offer valuable insights, enhancing the quality of our work. Additionally, I would like to thank Kevin Xu for his help with my programming.

.

Table of contents

List of Figures

List of Abbreviations and Symbols

CQDs	carbon quantum dots
QDs	quantum dots
PL	photoluminescence
PEG	polyethylene glycol
QY	quantum yield
N-CDs	nitrogen-doped carbon dots
AuNPs	unmodified gold nanoparticles
SCN^-	thiocyanate
LED	light emitting diodes
UV	ultraviolet
P3HT:PCBM	poly(3-hexylthiophene):[6,6]-phenyl-C61-butyric acid methyl ester
UV-VIS	ultraviolet-visible
vdW	van der Waals

1 Introduction

1.1 Background information of carbon quantum dots

1.1.1 Properties and applications

The first description of carbon quantum dots (CQDs) appeared in an article by Xu's group in 2004. Xu and his group isolated a fluorescent product during the purification process of single-walled carbon nanotubes using the electrophoretic method (Xu et al., 2004). This kind of fluorescent product was then identified as 'CQDs' by Sun about two years later (Sun et al., 2006).

CQDs are quasi-spherical nanomaterials with sizes smaller than 10nm (Wang & Hu, 2014). Most CQDs exhibit a synthesis-dependent core-shell structure, with the core being amorphous to nanocrystalline with predominantly sp^2 carbon and about 2-3nm in size (Zhang et al., 2015), whereas the shell consists of various polar or apolar groups, encompassing both tiny functional units and extended atomic structures (Lim et al., 2015; Sciortino et al., 2018), as shown in **Figure 1.1**.

The small size and diverse core-shell structure make CQDs have reliable and various properties, leading to significant attention in the scientific community. Furthermore, with the increasing research about CQDs, their wide-ranging applications continue to be discovered.

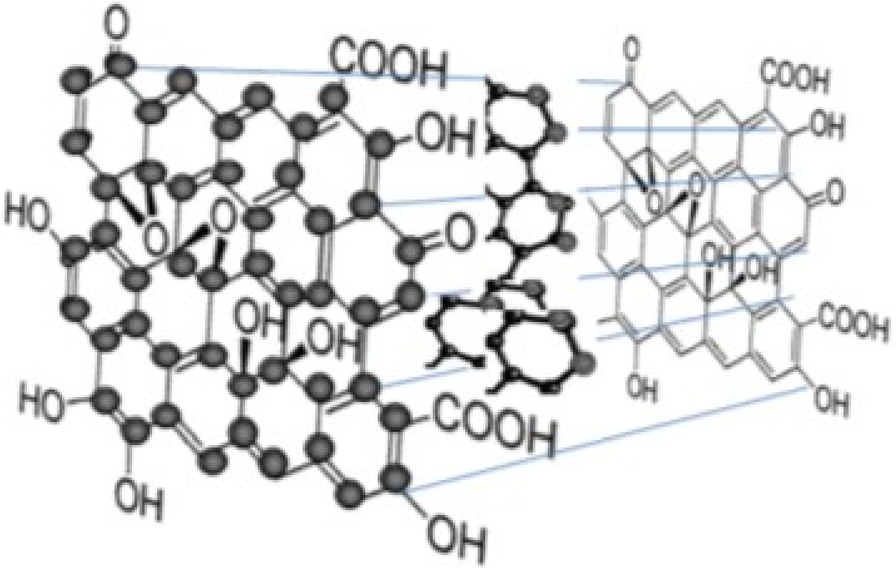

Figure 1.1 Chemical structure of CQDs. Reprinted from (Demchenko & Dekaliuk, 2013). Copyright 2013, with permission from IOP Publishing Ltd.

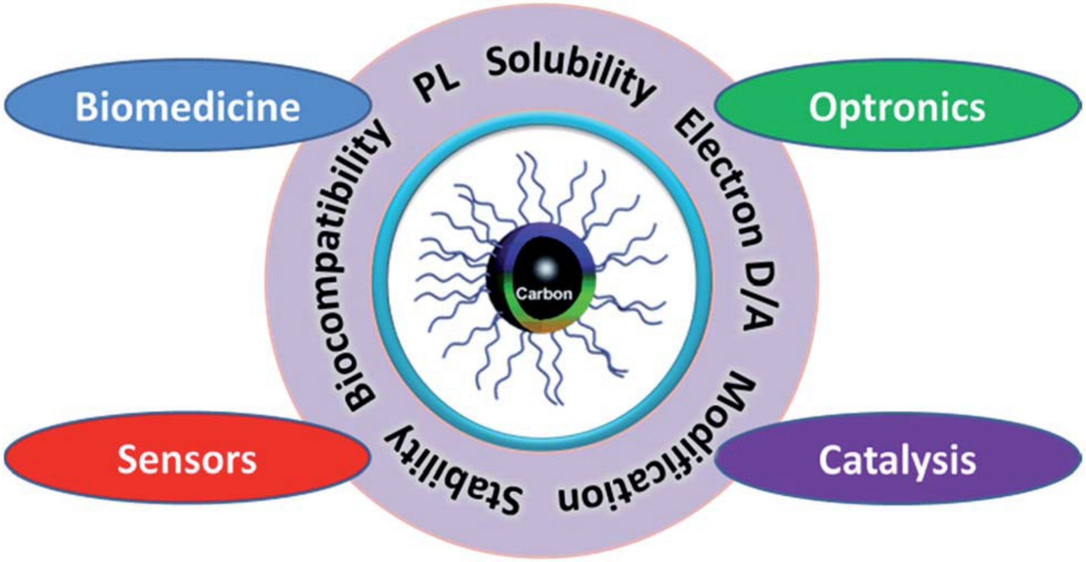

Figure 1.2 The various properties of CQDs and prospective utilization in biomedicine, sensors, optronics, and catalysis (Wang & Hu, 2014).

As is widely known, organic dyes have been commonly used for cellular visualization, while inorganic semiconductor quantum dots (QDs) have typically been employed for bioimaging purposes. However, challenges such as photobleaching and low extinction coefficients in organic dyes, as well as issues like limited solubility and intrinsic toxicity associated with semiconductor QDs restrict applications. By contrast, CQDs, with notable properties including photoluminescence (PL), low cytotoxicity, facile modification, good biocompatibility, high solubility, and high resistance to photobleaching, demonstrate considerable promise in fields such as biomaterials, optoelectronics, catalysis, and chemical sensors, as shown in **Figure 1.2** (Wang & Hu, 2014; Younis et al., 2020).

With the explosive growth of research on CQDs, there are numerous articles discussing their applications in various fields mentioned before, which cannot be exhaustively detailed. In the following paragraphs, only one to two typical examples are provided for each application area, aiming to offer a general picture of the potential applications of CQDs.

1.1.1.1 Biological applications

The key to the biological applications of nanomaterials lies in their biotoxicity and biological effects. Nanomaterials with core-shell structures, including Ag^+, Eu^{3+}, and semiconductor QDs like CdSe, have been recorded for their utilization in both *in vitro* and *in vivo* bioimaging (Rawat et al., 2023). Nevertheless, the utilization of heavy metals presents multiple health and environmental risks, limiting their applicability in biological fields. CQDs exhibit high PL, photostability, the ability to be excited and emit within visible spectrum, along with minimal toxicity in both *in vivo* and *in vitro* assessments, emerge as promising contenders for utilization in bioimaging, biosensors, and the delivery of biomolecules or drugs (Rawat et al., 2023).

Sun's group took the first step to explore the application of CQDs in bioimaging both i*n vitro* (Sun et al., 2006) and *in vivo* (Yang et al., 2009). Polyethylene glycol (PEG) functionalized CQDs, with high quantum yield (QY) of more than 10% at 400nm excitation, were injected into mice. Characteristics, such as strong fluorescence *in vivo*, biocompatibility, and nontoxicity were observed as a result.

In the following years, in the research focusing on the application of CQDs in bioimaging, researchers tried to develop red-emitting carbon dots that could be excited at long wavelengths, allowing for deep tissue penetration without harm to the target cell, tissue, or organ. Karakoçak et al. illustrated a straightforward synthesis, the pyrolysis of ethylenediamine and citric acid with the assistance of microwave, to produce carbon dots doped with nitrogen (N-CDs) emitting deep red light (600–700 nm) (Karakoçak et al., 2018). The synthetic process diagram is shown in **Figure 1.3 (a)**. Ex vivo porcine ocular globes images (**Figure 1.3 (b)-(d)**) and post-mortem whole-body mice images (**Figure 1.3 (e)-(i)**) illustrated the suitability and low toxicity of N-CDs. In the ex vivo test, 50 μL of N-CDs were injected into porcine ocular globes by post intravitreal injection. According to **Figure 1.3 (b)-(d)**, N-CDs were excited at 650nm and emitted 700nm light. N-CDs exhibited the ability to travel from the vitreous to cornea in under 30 minutes. Besides, the images obtained after local subcutaneous injection of N-CDs into post-mortem mice demonstrate sufficient contrast, which further proved the utility of N-CDs in bioimaging.

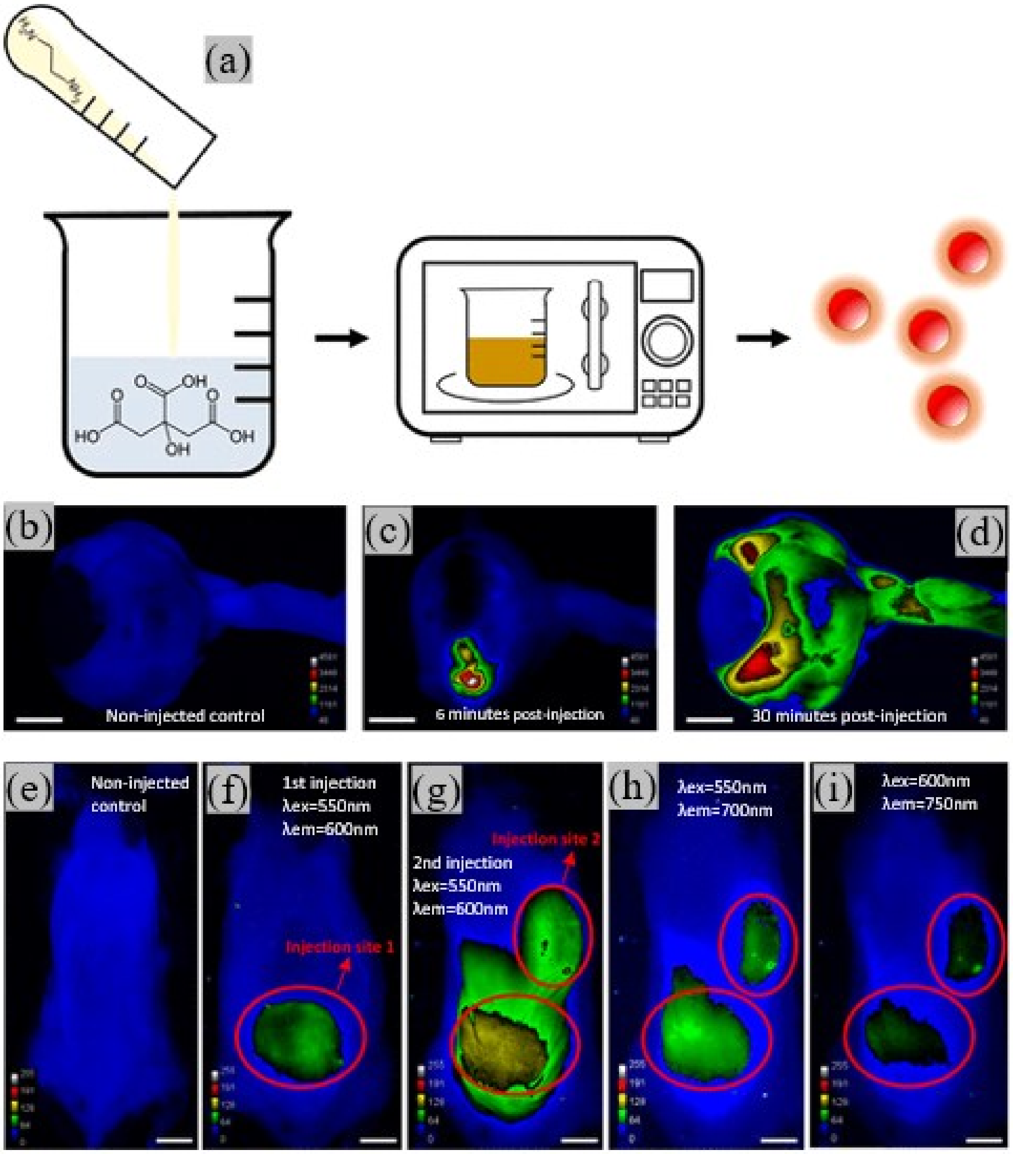

Figure 1.3 (a) The synthetic process diagram of N-CDs with red light emission. (b–d) *Ex vivo* porcine ocular globes images (λ_{ex} = 650 nm, λ_{em} = 700 nm). (e–i) Images of post-mortem whole-body mice after injection with N-CDs. All injections were N-CDs. The scale bar is 1 cm. Reprinted with permission from (Karakoçak et al., 2018). Copyright 2018 American Chemical Society.

Furthermore, by combining bioimaging with medical therapy, CQDs could play a role in biomedicine delivery systems. Linked with functional groups, CQDs could target drug delivery and help track the process by fluorescence (Kim et al., 2013; Zheng et al., 2014). The working principle of the utilization of CQDs in biosensing is similar to that in chemical sensing, which is going to be introduced in section 1.1.1.2, but higher requirement of the nontoxicity and biocompatibility (Rawat et al., 2023; Wang & Hu, 2014).

1.1.1.2 Chemical sensors

Generally, the working principle of chemical sensors using CQDs as fluorescent probes relies on the variation of the physicochemical properties of CQDs, such as QY, intensity, longevity, etc., when the surrounding environment undergoes alterations. These changes can result in either enhancement or quenching of the emission of CQDs (Gao et al., 2016). These alterations can selectively indicate the presence and quantity of analytes. The sensitivity of detection can be exceptionally high, with the ability to detect ions at concentrations as low as femtomolar levels (Liu et al., 2013).

According to research, CQDs could serve as sensors for temperature (Hu et al., 2022), pH detection (Mondal et al., 2019), and DNA (Li, Zhang, et al., 2011). CQDs could also be used to detect chemicals such as Hg^{2+}, Cu^{2+}, and Fe^{3+}, etc. (Gao et al., 2016; Li, Zhai, et al., 2011; Liu et al., 2013; Q. Qu et al., 2012; Qu et al., 2013; Zhou et al., 2012). However, the number of reports about applying CQDs in sensing anions is relatively low. This may be attributed to the fact that CQDs typically carry negative charges. To sense anions, CQDs might need to first bind with cations, resulting in the quenching, followed by the subsequent binding of anion analytes in the environment to recover and prevent the quenching of CQDs (Sciortino et al., 2018).

In Zhao et al.'s work, a dual readout, i.e. fluorometric and colorimetric, sensor with fluorescent CQDs and unmodified gold nanoparticles (AuNPs) serving as detector was developed to detect thiocyanate (SCN^-) (Zhao et al., 2015). In the absence of SCN^-, amino-functionalized CQDs (**Figure 1.4 (a)**) could easily bind to AuNPs stabilized by citrate, resulting in the clustering of AuNPs and the quenching of CQDs. This was the off state, at which the sensing solution was in blue, as shown in the upper line of **Figure 1.4 (b)**. However, with the presence of SCN^-, SCN^- had the priority to bind with AuNPs compared with CQDs, thus preventing the aggregation of AuNPs and remaining CQDs unquenching. At this light-on state, the sensing solution was red, with the intensity of the red color being dependent on the concentration of SCN^-, as shown in the lower line of **Figure 1.4 (b)**. Both the fluorometric and colorimetric signals could be obtained, as shown in **Figure 1.4 (c)**. In the assessment about sensing the quantity of SCN^- in saliva and tap water samples, this kind of sensor based on CQDs produced accurate and precise results (Zhao et al., 2015).

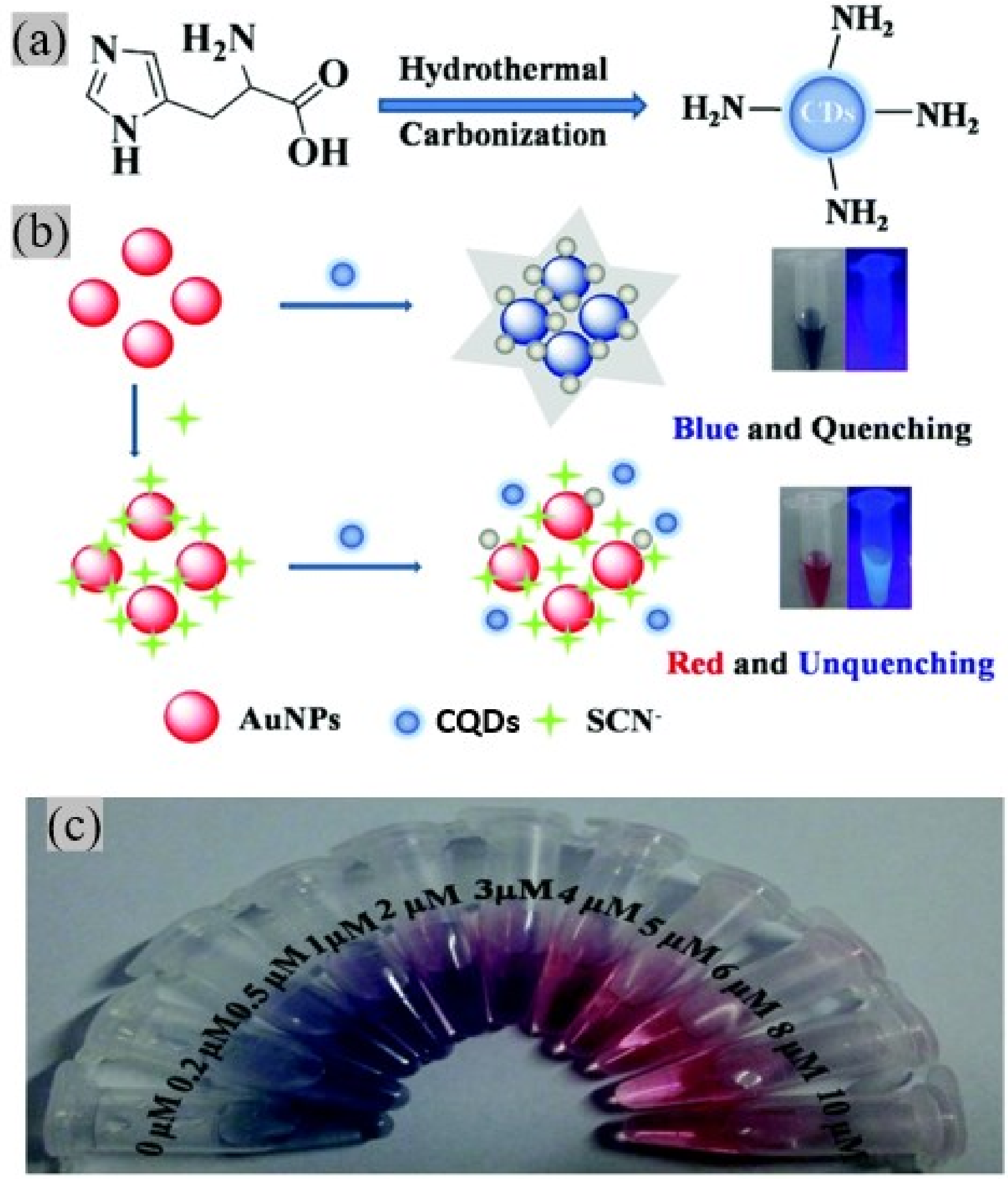

Figure 1.4 The diagrams of (a) the procedure for producing amino-functionalized CQDs and (b) the working principle of SCN^- sensor. (c) A photograph illustrating colorimetric responses corresponding to various concentrations of SCN^-. Reprinted from (Zhao et al., 2015). Copyright 2015, with permission from Royal Society of Chemistry.

1.1.1.3 Optronics

CQDs show promise for utilization in optoelectronics because of their strong absorption, down conversion PL, tunable emission, and the capabilities to donate and/or accept electrons (Sikiru et al., 2023). CQDs could serve as the active layer (Ding et al., 2017) or fluorescent downconverters (Chen et al., 2013) in light emitting diodes (LED). In the former, CQDs exhibited electroluminescence properties when used as the emitting layer within a multilayer structure upon external charge injection. The latter operated on the features of CQDs emitting visible light when excited by ultraviolet (UV) and blue light, while the tunable emission and high QY facilitated the obtaining of white LED (Sciortino et al., 2018). CQDs could also be applied to supercapacitors (Chen et al., 2016; Xu et al., 2016; Zhu et al., 2013) because of their ability to improve the electrical conductivity and specific surface area of the materials. Another important application of CQDs in optronics is solar cells (Jin et al., 2017; Zhu et al., 2019). For example, the harvesting spectrum of the solar cell was 480-650nm originally. After coating a polysiloxane layer containing CQDs on the cover glass of a P3HT:PCBM based solar cell, the spectrum 380-480nm could also be harvested, resulting in a 12% power conversion efficiency increase, as shown in **Figure 1.5** (Huang et al., 2014). This significant improvement illustrated the feasibility of applying CQDs in solar cells.

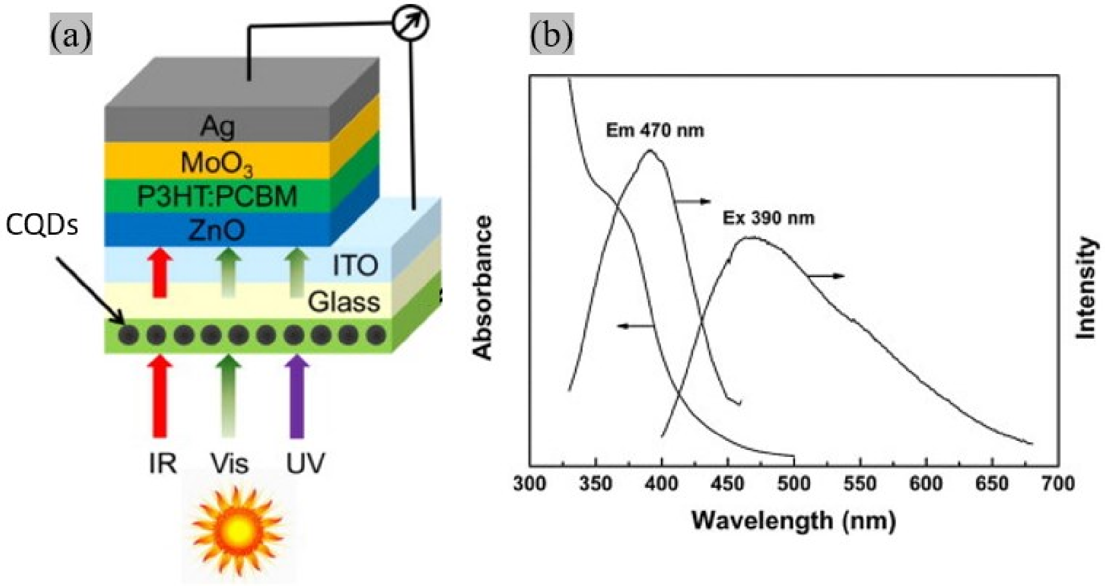

Figure 1.5 (a) The diagram of P3HT:PCBM based solar cell with CQDs filled polysiloxane composite coating. (b) The UV-VIS absorption and PL spectra of the polysiloxane composite filled with CQDs coated on glass. Reprinted from (Huang et al., 2014). Copyright 2014, with permission from Elsevier.

1.1.1.4 Photocatalysis

In general, photocatalysis includes energy conversion based on semiconductors and has been considered a viable method to alleviate energy crisis. Catalytic activity plays a crucial role in influencing photon utilization rate and photocatalytic efficiency. By coupling CQDs with semiconductor materials such as TiO_2 (Ke et al., 2017; Xie et al., 2014), Fe_2O_3 (Zhang et al., 2011), CdS (Zhang et al., 2020), SiO_2 (Li et al., 2010), etc., the shortages of low absorption capacity, low light utilization, and high charge recombination, commonly found in traditional photocatalysts could be improved (Zhao et al., 2023). These improvements took advantage of the features of CQDs decorated photocatalysts such as the enhanced light absorption extending to near-infrared wavelengths, improved separation of electron-hole pairs due to good electron transport ability, and good stability of CQDs coupled composite (Zhao et al., 2023).

Hydrogen production is a common application of CQDs photocatalysts. For instance, in Zhao et al.'s work, a type of CQDs modified TiO_2 composite prepared by hydrothermal method was utilized for the photoreforming of glucose to simultaneously produce H_2 and arabinose under neutral condition. The hydrogen production efficiency of this CQD/TiO_2 composite material was over 7 times higher than the material without CQDs, owning to the improved electron-hole separation capability with the increasing size of CQDs (Zhao et al., 2022). The potential photocatalytic mechanism is shown in **Figure 1.6**. When exposed to irradiation, electrons were stimulated to conduction band, thereby generating holes in valence band. Some of these electrons were harvested by CQDs and subsequently initiated the production of H_2 by proton reduction, while the remaining electrons participated in the production of radical $\cdot O^{2-}$ from absorbed oxygen. On the other hand, the photogenerated holes were used to produce radical $\cdot OH$ from absorbed H_2O. At the final step of the process, glucose reacted with these reactive oxygen species to obtain arabinose and CO as side products (Zhao et al., 2022). In this mechanism, CQDs served as the accepter or electron sink to help carry electrons from semiconductor surface to substances and subsequently facilitated the dissociation of electron-hole pairs, which corresponded to **Figure 1.7 (a)**. Furthermore, CQDs could be utilized as semiconductors to generate electrons and holes leading to the increase of light absorption and photocatalytic activity of photoelectrochemical cells, as shown in **Figure 1.7 (b)** (Xie et al., 2014).

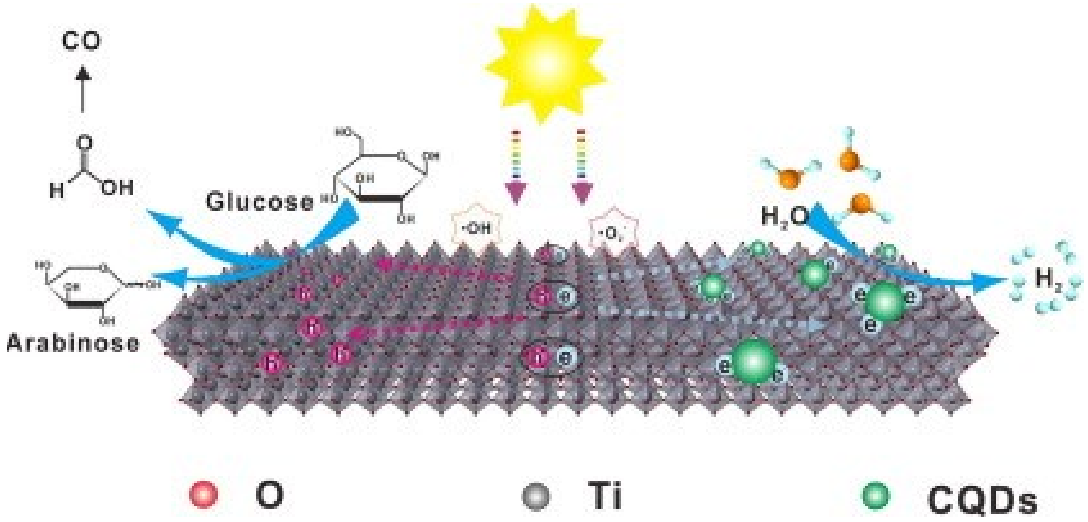

Figure 1.6 A schematic diagram of the possible reaction mechanism for glucose photoreforming. Reprinted from (Zhao et al., 2022). Copyright 2022, with permission from Elsevier.

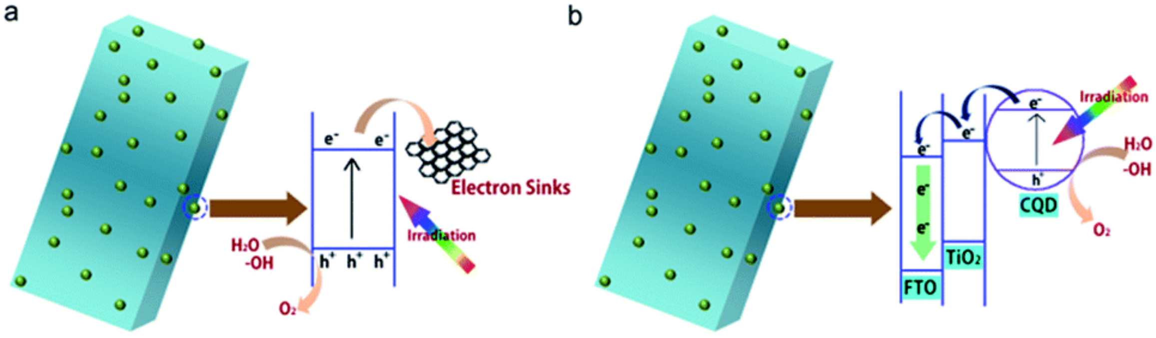

Figure 1.7 In CQD/TiO$_2$ photocatalysts, CQDs could serve as (a) acceptor or electron sinks and (b) a semiconductor. Reprinted from (Xie et al., 2014). Copyright 2013, with permission from Royal Society of Chemistry.

In addition, the applications of CQDs modified photocatalysts are not restricted in the production of hydrogen, researchers illustrated the possibility of its application in CO_2 conversion (Gao et al., 2019; Gao et al., 2021; Li et al., 2019), degradation of pollutants (Kooshki et al., 2019; Tian et al., 2017) and antibacterial (Kuang et al., 2019).

The CQDs-based devices currently being developed and tested are still limited to laboratory environments. Extensive research is still needed to explore their commercialization and industrial-scale production (Sciortino et al., 2018).

1.1.2 Photoluminescence mechanism

The characteristics of CQDs including high solubility, PL, low cytotoxicity, etc. make CQDs have a wide-ranged application. Among these properties, PL is the essential and crucial one. Therefore, the study of PL mechanism holds significance in improving the performance of CQDs in various application fields. In PL, an electron in the molecule is exited instantaneously from the ground state to a higher energy state by absorbing photons. The energy state to which the electron is exited is associated with the energy, or wavelength, of the absorbed photon. At this time, the excited state is unstable, thus the electron will relax back to the ground state with the emission of photon. The emitted wavelength is determined by the energy difference between the ground state and the excited state. The emission wavelength is usually longer than the absorption wavelength under normal circumstances because electrons experience some energy loss. PL can be further subdivided into two types. The first type of PL is fluorescence. Fluorescence is an immediate PL that happens in a very short time scale after photoexcitation. The other one is phosphorescent. A substance with phosphorescent property can be PL continuously after photoexcitation. Both kinds of PL could be observed in CQDs, although the reports about phosphorescence are rare (Zhang et al., 2022).

Since the fluorescent properties of CQDs vary from different raw materials, synthetic methods, and following modifications, the mechanism of fluorescence becomes complicated. With decades of study, the fluorescent mechanism of CQDs has matured. Three theories are widely accepted recently, namely, size effect, surface state, and molecular state (Zhang et al., 2022; Zhu et al., 2015).

Size effect is the first fluorescent mechanism of CQDs. It means that the PL outcome of CQDs becomes size-dependent when their size is reduced below the exciton radius, namely the Bohr radius. CQDs are nanomaterials with sizes smaller than 10nm, which fall in the quantum size range (Wang & Hu, 2014). As the size of CQDs increases, the band gap becomes narrow, leading to the red shifting of the emission band, referring to the PL process introduced before. Li’s group developed a series of CQDs with sizes ranging from 1.2 to 3.8nm which exist clear size-dependent PL (Li et al., 2010). According to **Figure 1.8 (a)**, the PL energy of CQDs dropped sharply with the increasing particle size: from UV light to near-infrared light. Correspondingly, the band gap decreased as the size of CQDs grew bigger, as shown in **Figure 1.8 (b)**. Li and coworkers’ work provided evidence for the size effect mechanism. However, the size effect mechanism is not the most common as many reports do not show data to support it or even obtain opposite results (Mintz et al., 2019; Sciortino et al., 2018).

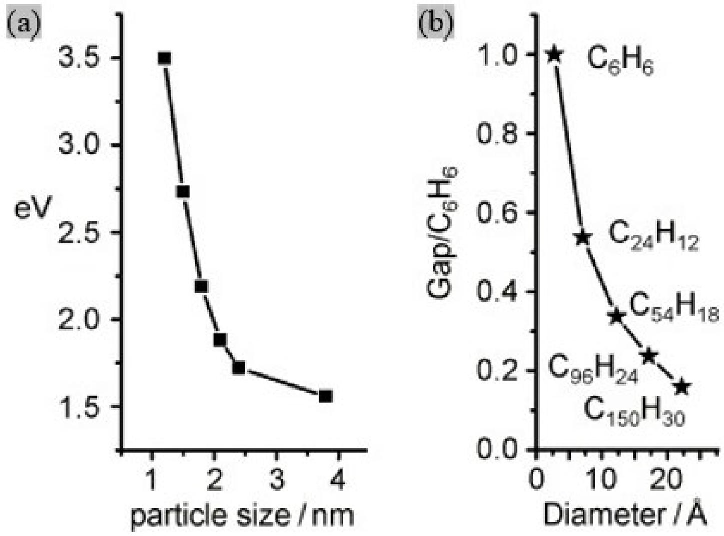

Figure 1.8 (a) Size dependent PL properties of CQDs. (b) Relations between band gaps and the size of CQDs. Reprinted from (Li et al., 2010). Copyright 2010, with permission from John Wiley and Sons.

Secondly, surface state PL is a widely accepted fluorescent mechanism. The surface states of CQDs are linked to the hybridization of functional groups and carbon backbones (Zhang et al., 2022). The surface defects, surface charge traps, and functional groups could result in the existence of extrinsic surface states, while intrinsic surface states depend on the size of the crystal itself (Mintz et al., 2019). The alignment of intrinsic and extrinsic states controls the PL outcome of CQDs. The mechanism was described in Zhu et al.'s work, where the energy levels of four kinds of CQDs with different sizes were compared (Zhu et al., 2014). According to **Figure 1.9,** when a system was photoexcited, the electrons were excited to the intrinsic states. If the energy level of edge states was lower than the intrinsic states, the electrons relax to the edge states and therefore the energy of emission photon corresponded to the energy difference between edge states and the ground state. On the other hand, if the energy level of edge states was higher than intrinsic states, edge states were not involved in the emission. In addition, the PL properties of CQDs with surface passivation are strong evidence supporting the surface state mechanism. In Sun et al.'s work, CQDs synthesized through laser ablation showed almost no PL property but fluoresced after surface passivation with PEG, because PEG could stabilize the surface defects of CQDs (Mintz et al., 2019; Sun et al., 2006; Zhang et al., 2022).

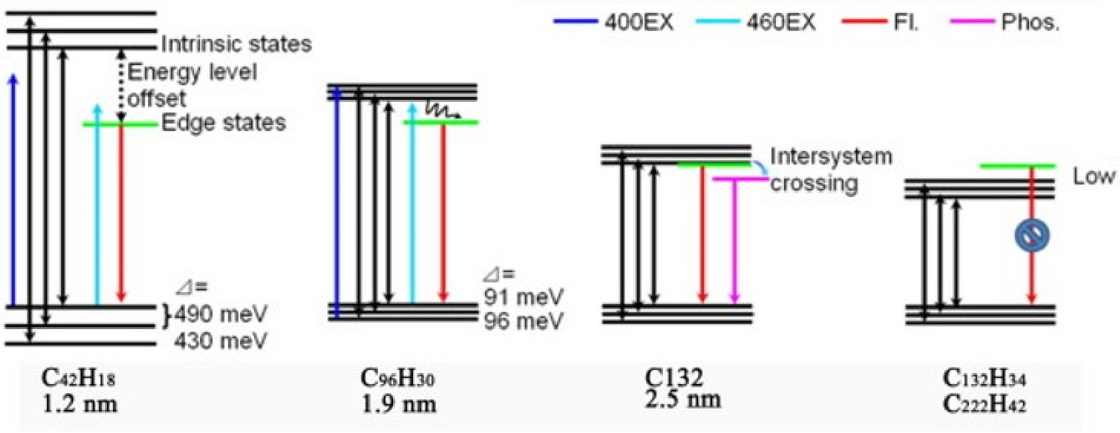

Figure 1.9 The energy level structures, including intrinsic states and edge states, of CQDs of different sizes. Reprinted from (Zhu et al., 2014). Copyright 2014, with permission from Elsevier.

The last fluorescent mechanism of CQDs is molecular states. It means that fluorescent molecular fragments are formed during the synthetic process of CQDs caused by side reactions and the attachment of these fluorophores to the surface of CQDs endows the emission characteristics of the products (Zhang et al., 2022; Zhu et al., 2015). Molecular states commonly happen in the synthetic process through bottom-up routes. Researchers used citric acid as a carbon source to produce a series of CQDs by hydrothermal and microwave methods (Essner et al., 2018). After comparing the optical properties of the purification products, they demonstrated the existence of fluorophores in the products synthesized by bottom-up routes. Meanwhile, they illustrated that these fluorophores play a predominant role in the fluorescence of CQD products, leading to a significant overestimation of the PL performance of CQDs prepared by bottom-up routes (Essner et al., 2018).

Phosphorescence, as another type of PL, is a less common property found in CQDs. When CQDs are scattered in room-temperature polyvinyl alcohol and excited with UV light, phosphorescence can be observed (Zhang et al., 2022).

1.1.3 Synthesis methods

The synthesis methods of CQDs are divided into two approaches: bottom-up and top-down. As the name implies, bottom-up approaches refer to synthesizing CQDs from small precursors, while top-down approaches break large carbon sources into small pieces to obtain CQDs (**Figure 1.10**).

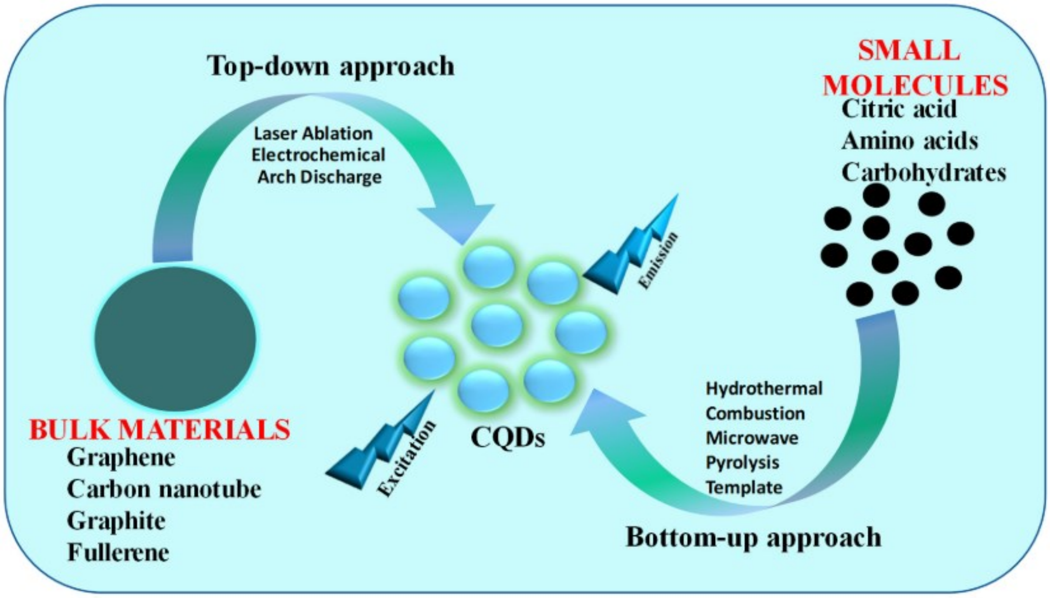

Figure 1.10 Bottom-up and top-down approaches to synthesize CQDs (Yadav et al., 2023).

1.1.3.1 Bottom-up approaches

Bottom-up approaches involve the utilization of small precursors such as citric acid, carbohydrates, amino acids, etc. (Bourlinos et al., 2008; Jamila et al., 2022; Peng & Travas-Sejdic, 2009; S. N. Qu et al., 2012) to form CQDs through techniques such as hydrothermal/solvothermal (Ran et al., 2020; Zhang et al., 2010), microwave-assisted (Jeong et al., 2021), template method (Gu et al., 2017), etc. The mechanism of bottom-up approaches involves the precursor materials undergoing low-temperature carbonization, which is essentially a slow pyrolysis process, to form CQDs (Das et al., 2018).

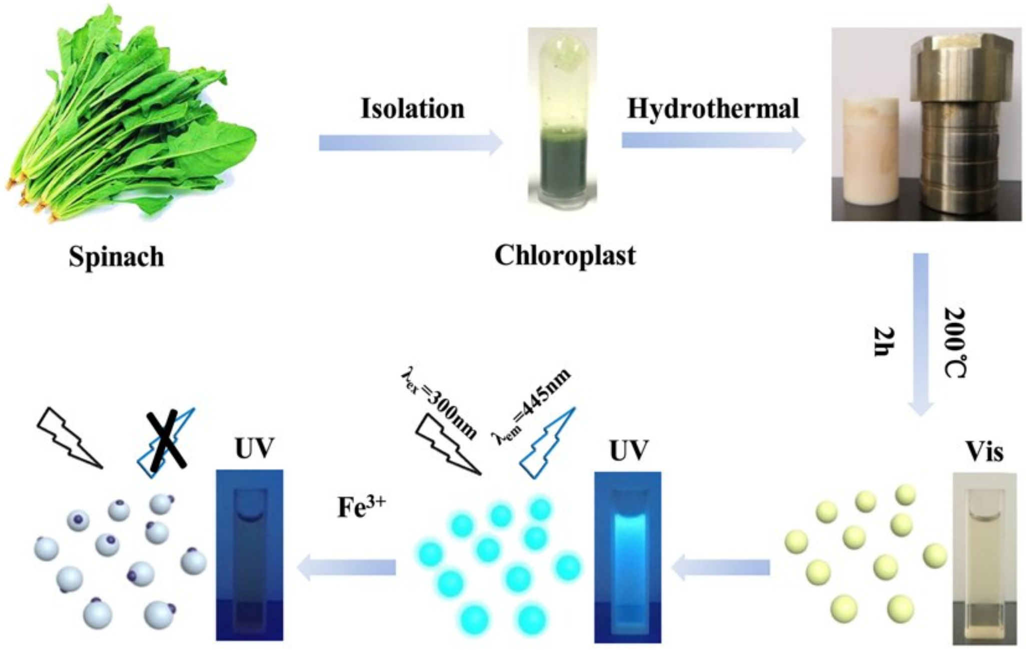

Figure 1.11 A schematic process of using chloroplast to synthesize CQDs and the application of Fe^{3+} sensing. Reprinted form (Ran et al., 2020). Copyright 2020, with permission from John Wiley and Sons.

The carbon precursors could also be nature source since the ‘green’ synthesis of CQDs has become a trend (Das et al., 2018; Yadav et al., 2023). For instance, Ran and coworkers treated the chloroplast extracted from fresh green leaves with hydrothermal treatment to synthesize CQDs, as shown in **Figure 1.11**. The resulting CQDs had an emission wavelength of 445nm when excited under UV light. The possibility of the application in Fe^{3+} sensing was demonstrated (Ran et al., 2020). However, the produced CQDs had a relatively low QY of about 0.68%, which may be attributed to the purification and separation processes of CQDs (Ran et al., 2020).

Although bottom-up approaches are typically facile, direct, and highly controllable methods, the challenges of purification, difficulties for large-scale production, and the effects of side reactions mentioned earlier in the 1.1.2 section are unavoidable disadvantages of bottom-up approaches (Essner et al., 2018; Ran et al., 2020).

1.1.3.2 Top-down approaches

The carbon source of top-down approaches involves graphite, carbon nanotubes, fullerene, active carbon, and other bulk materials containing similar chemical structures in CQDs (Sciortino et al., 2018; Zhang et al., 2022; Zhou et al., 2007).

Laser ablation technique could be used to synthesize CQDs by irradiating the surface of the target carbon source with a high energy laser beam (Cui et al., 2020; Sun et al., 2006). A sample instrument setup diagram of laser ablation which used graphite as target is shown in **Figure 1.12** (Yang et al., 2021). Electrochemical oxidation is another top-down technique. As shown in **Figure 1.13**, in the presence of a reference electrode, larger carbon sources are cut into small fragments and then generate CQDs (Liu et al., 2016; Zhou et al., 2007). In addition, chemical oxidation method is based on the exfoliation of carbon source by strong oxidizing agents and concentrated acids (Thambiraj & Shankaran, 2016).

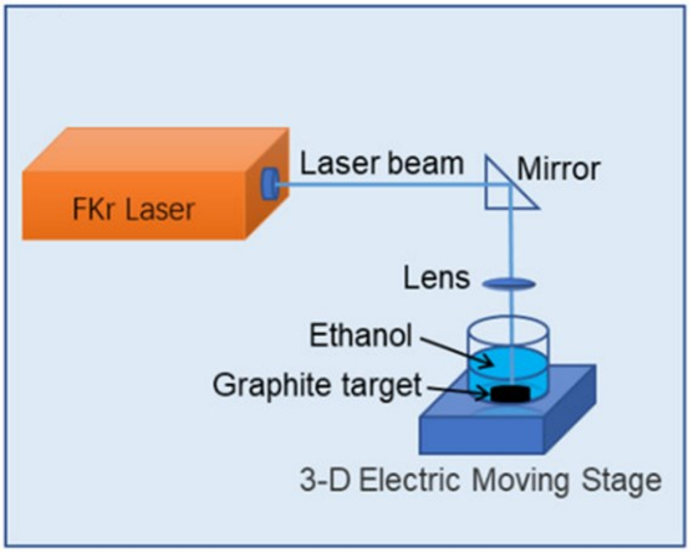

Figure 1.12 The schematic instrument setup diagrams of laser ablation approach. Reprinted from (Yang et al., 2021). Copyright 2021, with permission from John Wiley and Sons.

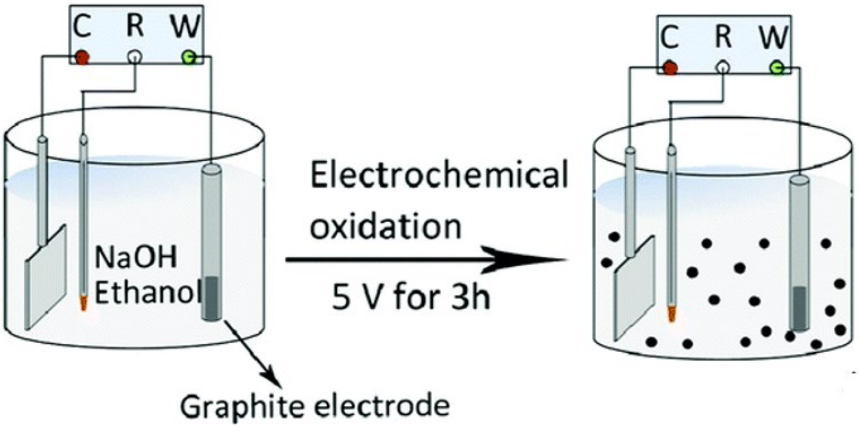

Figure 1.13 The schematic instrument setup diagrams of electrochemical oxidation approach. Reprinted from (Liu et al., 2016). Copyright 2016, with permission from Royal Society of Chemistry.

Moreover, ball milling, a mechanical method, has been developed. In Han et al.'s work, the mixture of cellulose and Mg powder was ball milled together with ZrO_2 balls at a speed of 360 rpm for 28 hours. CQDs were obtained after the centrifugation and dialysis of the ball milled products. The produced CQDs exhibited an average size of 4.8nm and could be used for Fe^{3+} sensing (Han et al., 2019). Carbon black is another carbon source that can be used in ball milling methods. In Youh et al.'s work, carbon black powder with a diameter of 20-30nm, sodium carbonate, and ZrO_2 balls with sizes of 100μm were milled together at a speed of 500rpm for 24 hours. The size of the produced CQDs centered at 3.0nm. The ultraviolet-visible (UV-VIS) spectrum (**Figure 1.14 (a)**) and PL spectra (**Figure 1.14 (b)**) showed that the maximum peak intensity of emission appeared at 430nm when excited at 320nm (Youh et al., 2021). CQDs synthesized by other raw materials such as active carbon and coal particles, etc., have wide-ranged applications as well (Hu et al., 2016; Wang et al., 2015).

Compared with bottom-up methods, top-down approaches face the challenges of broad size distribution and low efficiency. Nonetheless, its raw materials are less costly, and the technique is more suitable for large-scale production (Al Jahdaly et al., 2021).

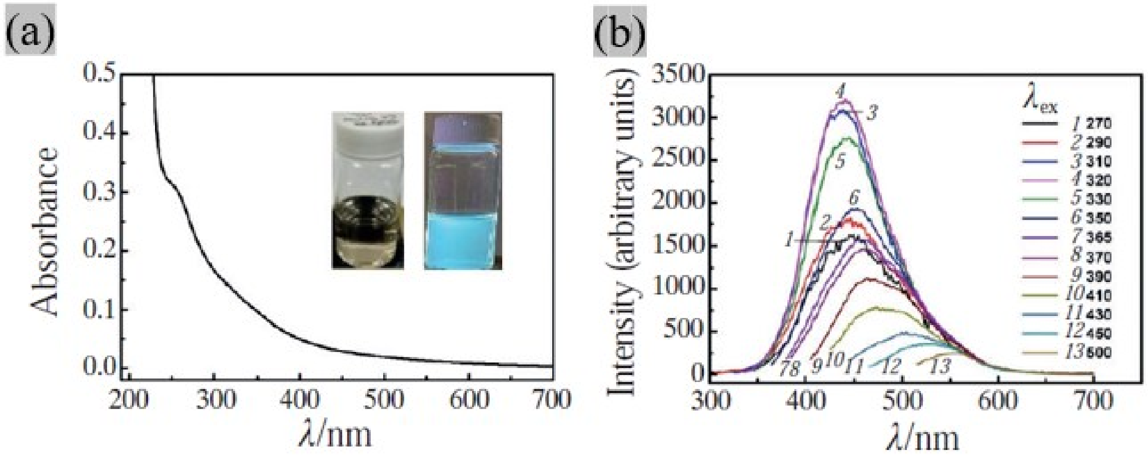

Figure 1.14 (a) UV-VIS spectrum of the CQDs solution. (b) PL spectra of CQDs. Reprinted from (Youh et al., 2021). Copyright 2021, with permission from Elsevier.

1.2 Remaining problems

After understanding the applications, PL mechanisms, and synthesis approaches of CQDs, we realize the importance of carbon source selection and synthesis method choice in determining the properties of the produced CQDs, as well as their possible applications. While the bottom-up approach faces challenges such as byproduct formation, product purification, and poor water solubility, the top-down approach effectively avoids these problems and has potential for large-scale production, despite its own challenges of broad size distribution and low efficiency (Essner et al., 2018; Ran et al., 2020; Sciortino et al., 2018). Among the various carbon sources for top-down CQDs synthesis, such as graphite, fullerenes, and carbon nanotubes, coal can be a suitable carbon source due to its abundant availability in nature, lower cost, and unique chemical structure (Hoang et al., 2018;

Mandal et al., 2023). These characteristics make coal an appropriate choice for synthesizing CQDs.

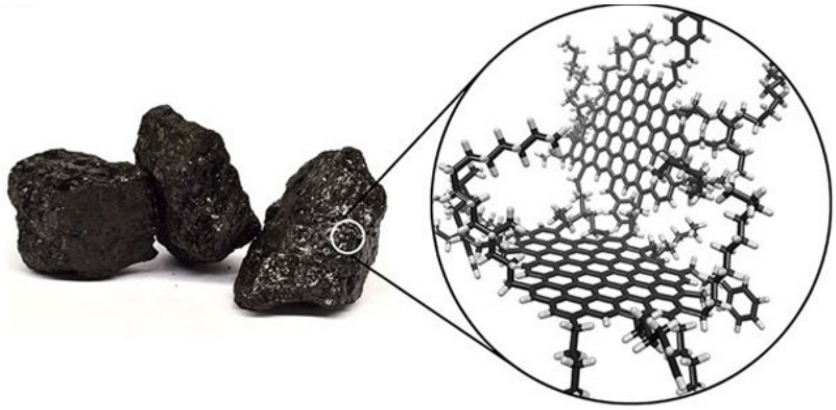

Figure 1.15 Bulk coal image and schematic nanostructure of coal. Reprinted from (Ye et al., 2013). Copyright 2013, with permission from Springer Nature.

The composition of coal is usually described by ash analysis and proximate analysis, i.e. the weight percent of ash, moisture, volatile moisture, fixed carbon, carbon, hydrogen, nitrogen, oxygen, and sulfur (Saikia et al., 2019). The result of proximate analysis, especially the weight percent of fixed carbon, is one of the reference conditions for classification of the rank of coal. The common ranking of coal types is anthracite, bituminous, sub-bituminous, and lignite coal, from highest to lowest. The structure of coal, as shown in **Figure 1.15**, contains crystalline carbon regions surrounded by loosely packed sp^3 hybridized carbon chains and other impurities. These crystalline carbon regions have similar structures with CQDs, making coal a suitable carbon source for CQDs (Mandal et al., 2023; Ye et al., 2013). The presence of crystalline carbon domains eliminates the need for carbonization when coal is used as a carbon source, distinguishing it from other natural carbon sources (Das et al., 2018).

However, the most commonly used chemical oxidation method for preparing coal-based CQDs involves the utilization of substantial quantities of strong oxidants and strong acids, resulting in the generation of toxic gases and limiting the application of the products in the biological field (Rawat et al., 2023). Furthermore, the products suffer from broad size distribution, which also restricts the application of CQDs (Ye et al., 2013). To address these problems, our attention turns to a mechanical method, ball milling. The mixture of materials to be ground and grinding media, including ceramic balls and stainless-steel balls, is ground in a ball mill. The size of the resulting product can be regulated by the dimensions of the grinding media: the smaller the grinding media, the smaller the size of the product. Ball milling has been proven to be suitable for the preparation of CQDs with various carbon sources, as illustrated in the 1.1.3.2 section. However, whether coal-based CQDs could be directly synthesized using only ball milling is still in controversy.

1.3 Previous attempts

The previous reports about preparing coal-based CQDs using ball milling have mainly focused on using ball milling as a method to reduce the size of coal particles, rather than specifically for the synthesis of CQDs (Hu et al., 2016; Prazyan; & Dyagilev;, 2021). In Hu et al.'s work, after grinding for 5 hours, the size of anthracite coal was reduced to several micrometers. The coal powder was then treated with 30% hydrogen peroxide and finally produced CQDs, which had a size under 3nm. In this process, ·OH radicals help the cleavage of graphite structure (Hu et al., 2016). This attempt still relied on the utilization of strong oxidants. Recently, Zhang and coworkers synthesized coal-based carbon nanomaterials with a diameter of 30nm by solely using ball milling (Zhang et al., 2023; Zhang et al., 2024). This work gave new insight into synthesis of coal-based CQDs by ball milling, although CQDs were not obtained. We believe that there are still some mechanisms that have not been fully understood during the process of preparing coal-based CQDs through mechanical milling (ball milling). However, the preparation of coal-based CQDs with ball milling is a macroscopic process, but the essence and key of this process is the exfoliation of the graphite layers in coal particles, which is a microscopic process. Therefore, the main problem becomes whether van der Waals (vdW) bonds between graphite layers in coal particles can be broken during ball milling. To investigate this microscopic problem, a simulation-based approach should be used rather than experimental methods. We simulate the structure of coal particles and apply shear force to observe its effects on vdW bonds between graphite layers.

1.4 Our new plan

The aim of this study is to investigate the field of coal-based CQDs generation by ball milling through the study of the mechanism behind this process. We employ a numerical simulation method to simulate the effect of shear stress on coal particles, with the aim of addressing the problem of whether vdW bonds between graphite layers in coal particles can be broken during ball milling.

A two-dimensional model with Python is built to simulate two kinds of coal: bituminous and anthracite coal. After applying shear stress, the propagation process of strain in coal particles can be shown during the iterations. Significant differences in the proportion of broken vdW bonds between the simulated bituminous and anthracite particles are observed. To further explore this process, we simulate some coal particles with certain crystal parameters to find the relation between the parameters with the exfoliation of graphite layers. As the size of the crystalline carbon domains in coal particles increases, the proportion of broken vdW bonds decreases. The results show the possibility of applying ball milling method in synthesizing coal-based CQDs and provide guidance for the selection of coal type.

2 Methodology

2.1 Derivation of the master formula

The propagation of the strain across the simulated coal particle follows the Master formula (Xu, 1992; Xu et al., 2020):

$$P_{new} = P_{old} + s\sum_{j}\left(P_j W_{ji} - P_i W_{ij}\right) \tag{1}$$

According to Newton's 2nd Law and the theory of elasticity, we have:

$$\begin{cases} F = ma = m\dfrac{\partial^2 u}{\partial t^2} \\ F = E\dfrac{\partial^2 u}{\partial x^2} \end{cases} \tag{2}$$

By combining the two equations, we get:

$$\frac{\partial^2 u}{\partial t^2} = \frac{E}{m}\frac{\partial^2 u}{\partial x^2} \tag{3}$$

where u measures the distance from the equilibrium of atom, and E is Young's modulus. The parameter u essentially measures the magnitude of the strain traveling in the material. Thus, we introduce P, a variable that changes between [-1,1], to represent the strain. The damping term, which is inversely proportional to $\frac{\partial P}{\partial t}$, is added to the equation (3). We get:

$$\frac{\partial^2 P}{\partial t^2} = \frac{E}{m}\frac{\partial^2 P}{\partial x^2} - k\frac{\partial P}{\partial t} \tag{4}$$

The equation (4) contains the acceleration term, $\frac{\partial^2 P}{\partial t^2}$. This term is bounded by the form of sine and cosine functions. Therefore, it can be dropped in the approximation:

$$\frac{\partial P}{\partial t} = \frac{E}{mk}\frac{\partial^2 P}{\partial x^2} \tag{5}$$

Leaving only the damping term, the wave equation changes into a form of diffusion equation. A propagation variable is introduced:

$$s = \frac{E}{mk}\frac{\Delta t}{\Delta x^2} \tag{6}$$

According to the equation (Xu, 1992):

$$P_{new} = P_{old} + dPi \tag{7}$$

where P_{new} represents the updated value of P at site i, P_{old} represents the previous value of P to be updated, and P_i denotes the value of P at site i.

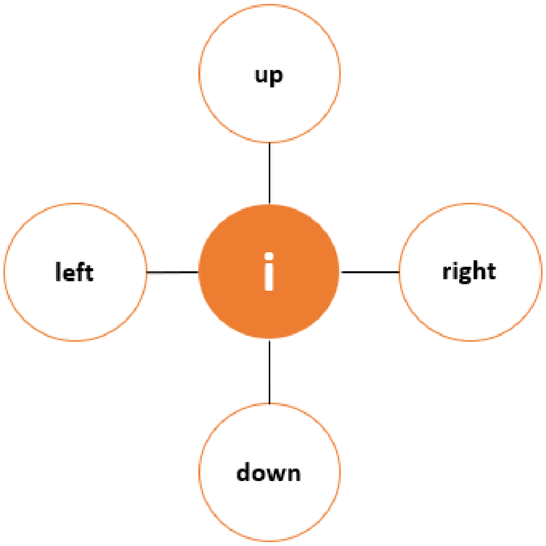

Figure 2.1 Interactions between site i and its up, right, down, and left neighbors.

As shown in **Figure 2.1**, each site is assigned a specific P value, which describes the strain of the site. Site i is binding with up, right, down, and left neighbors through the interactions which allow the propagation of strain. We introduce W_{ij}, variable changes between [0,1], as the binding of site i to the adjacent sites. As shown in **Figure 2.1**, j represents the site on the left, right, up, and down of site i:

$$dP_i = s\sum_j (P_j W_{ji} - P_i W_{ij}) \tag{8}$$

Finally, we can get the Master formula:

$$P_{new} = P_{old} + s\sum_j \left(P_j W_{ji} - P_i W_{ij}\right) \tag{1}$$

2.2 Two-dimensional model development

To have a closer look at the propagation of the strain in coal particles under shear force during ball milling, the propagation of strain is described by the Master formula (**equation (1)**) in 2D. Thus, we tried to use a model to simply simulate the cross-section structure of coal particles. The structure of graphite layers in coal particles in 3D is shown in **Figure 2.2**. Layers of graphene are connected by vdW bonds with a length of about 0.35nm. To reduce the dimension to 2D, parallel lines are used to represent the graphite layers.

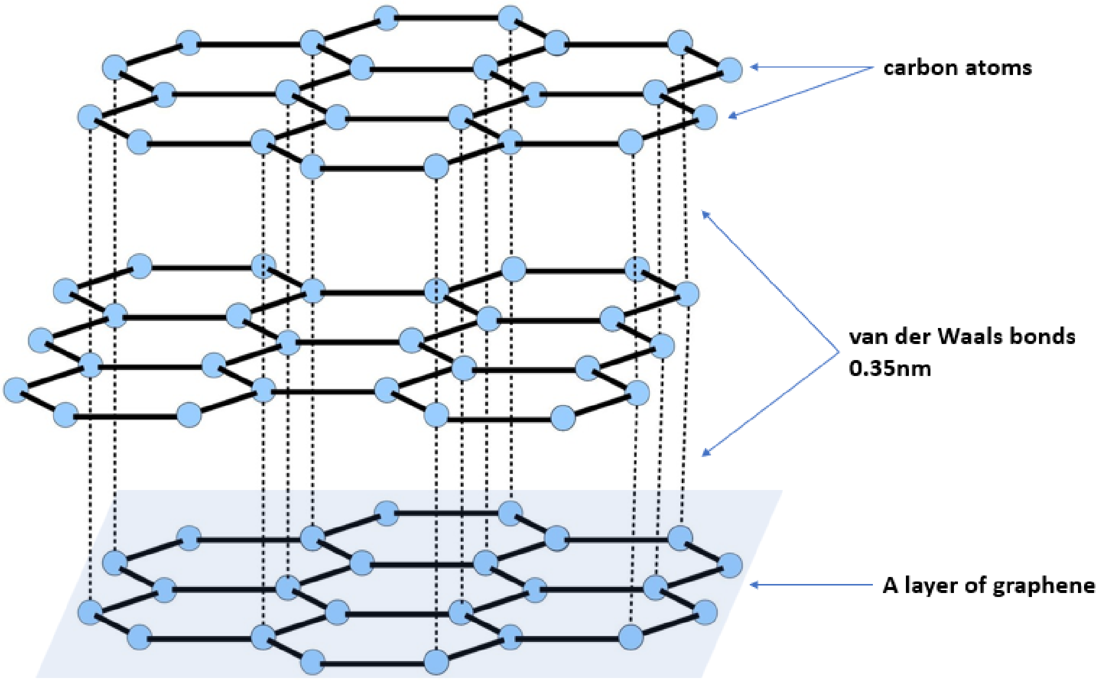

Figure 2.2 A schematic diagram of the structure of graphite layers in 3D.

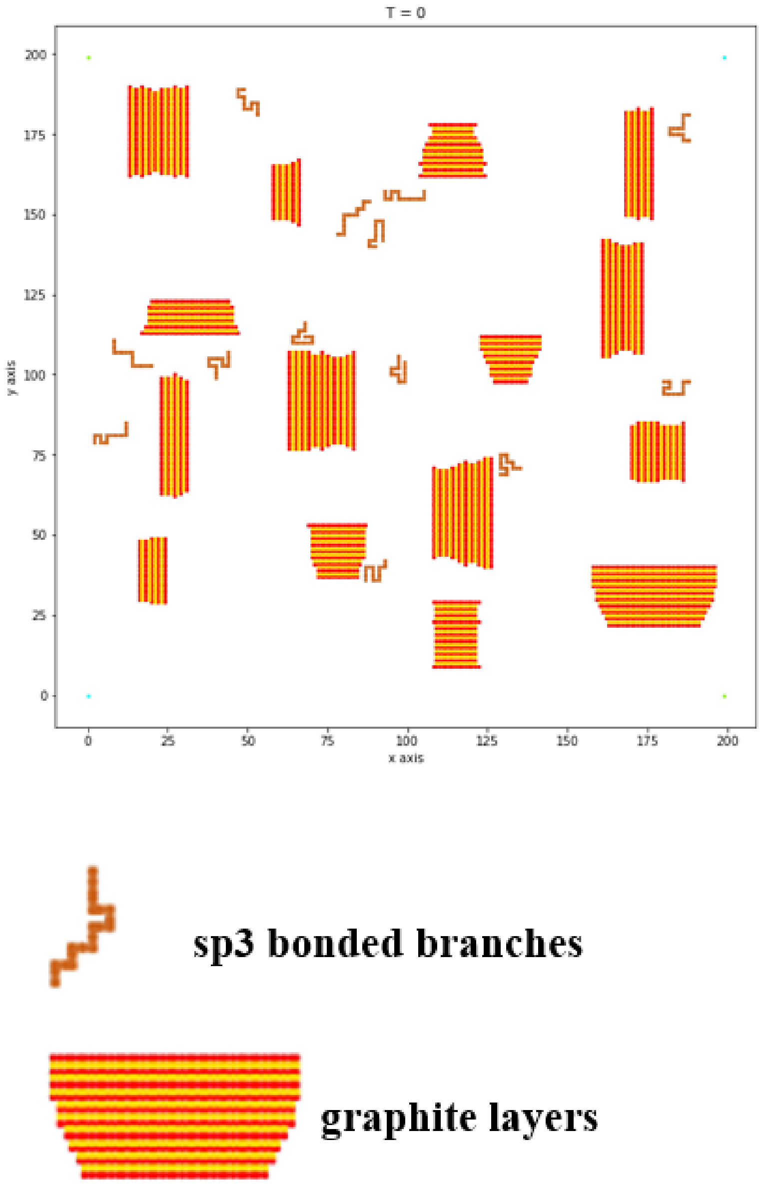

Figure 2.3 The simulated 2D 200×200 coal particle. The graphite layers and van der Waals bonds are represented by red and yellow parallel lines. The sp^3 carbon branches are represented by brown broken lines.

As mentioned before, coal contains graphite, sp^3 bonded branches, and some loosely packed impurities. **Figure 2.3** shows the coal particle under 2D approximation. The graphite layers and vdW bonds are represented by red and yellow parallel lines. The sp^3 carbon branches are represented by brown broken lines. Under certain restrictions, the size, position, and shape of graphite layers are randomly generated. The sp^3 carbon branches are generated through random walk. According to section 1.2, in nature, various ranks of coal exist, including anthracite and bituminous coal, which have different sizes and amounts of crystallized structure. These various coal types can be simulated by adjusting the size and amount of graphite layers in the model of the coal particle.

Since the cross-section of coal particles is simulated, the boundary conditions should be designed. At the left boundary of the 200×200 square, the left neighbor term in the main equation is dropped because of the absence of the left neighbor. For the other three boundaries, the situation is the same. The boundary conditions are summarized below:

$$\begin{gathered} if\ y + 1 = 200: \\ y_{up} = y \end{gathered} \tag{9}$$

$$\begin{gathered} if\ x + 1 = 200: \\ x_{right} = x \end{gathered} \tag{10}$$

$$\begin{gathered} if\ y - 1 = -1: \\ y_{down} = y \end{gathered} \tag{11}$$

$$\begin{gathered} if\ x - 1 = -1: \\ x_{left} = x \end{gathered} \tag{12}$$

Under stress, when damping is strong, the elastic wave equation is approximated by diffusion equation, as mentioned before. Before the iteration starts, i.e., at T equals 0, P values at all sites are set to be zero. To simulate shear stress, corner P values are diagonally set as ±1. Blue means that P equals 1 at the site, while color green means that P equals -1 at the site, as shown in **Figure 2.3** and **Figure 2.4**. Graphene layers (red lines) and sp^3 carbon branches (brown lines) are assumed to be unbreakable during the iterations. The W values for vdW bonds (yellow lines) are randomly set between 0.2 and 0.5, which are updated in the same domain during the iterations. W values for the white area are in the range [0,1].

During the iterations, as shown in **Figure 2.4**, P values for all sites are updated according to the Master formula (**equation (1)**) due to the propagation of the strain. The positive P value means that the point is pulling away from its neighbors on average, and vice versa. The breakage of the bonds occurs when the absolute value of P approaches 1. As shown in **Figure 2.4**, the color of the sites turns blue when P values reach 1 and turns green when P values reach -1.

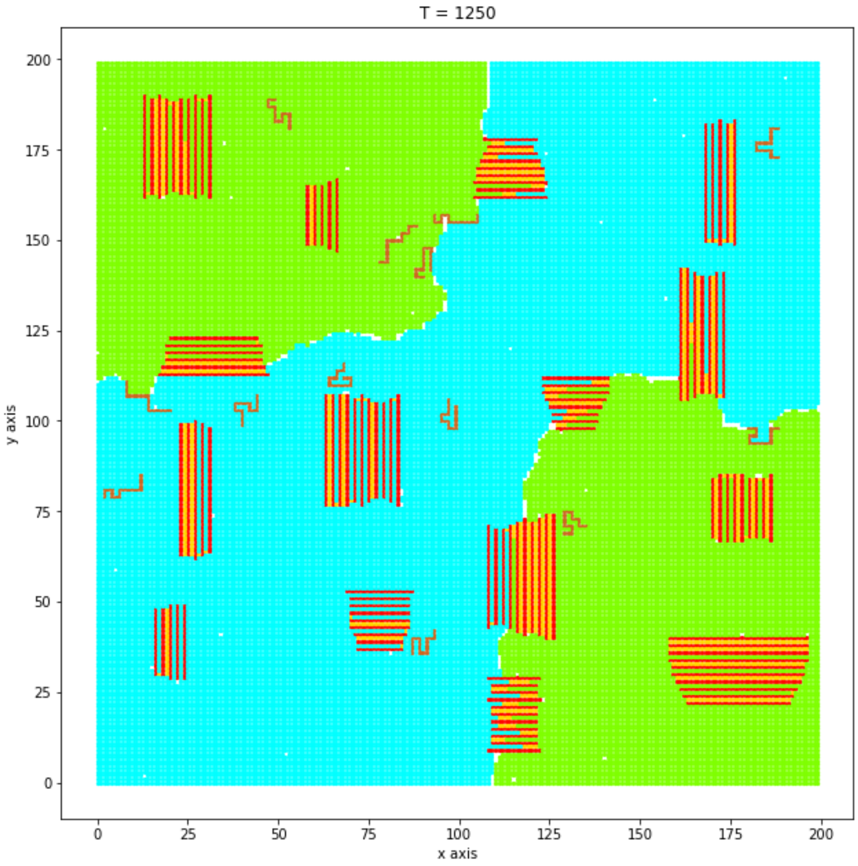

Figure 2.4 A schematic illustrating simulated coal particles during the iterations.

2.3 Quantification of the results

To quantitatively describe the propagation of the strain over time, the averaging of x coordinates is conducted utilizing the absolute value of P, denoted as <x^2>. The results are plotted against the time step by the equation:

$$< x^2 >= \sum P_i x_i^2 \tag{13}$$

Furthermore, the description of the extent of the breaking of vdW bonds between graphite layers is needed. The proportion of the broken vdW bonds over the initial number of vdW bonds is used to quantitatively express the break of bonds, and further indicate the exfoliating process of graphite layers.

2.4 Scheme of the program

A simplified flowchart of the program is provided in **Figure 2.5**.

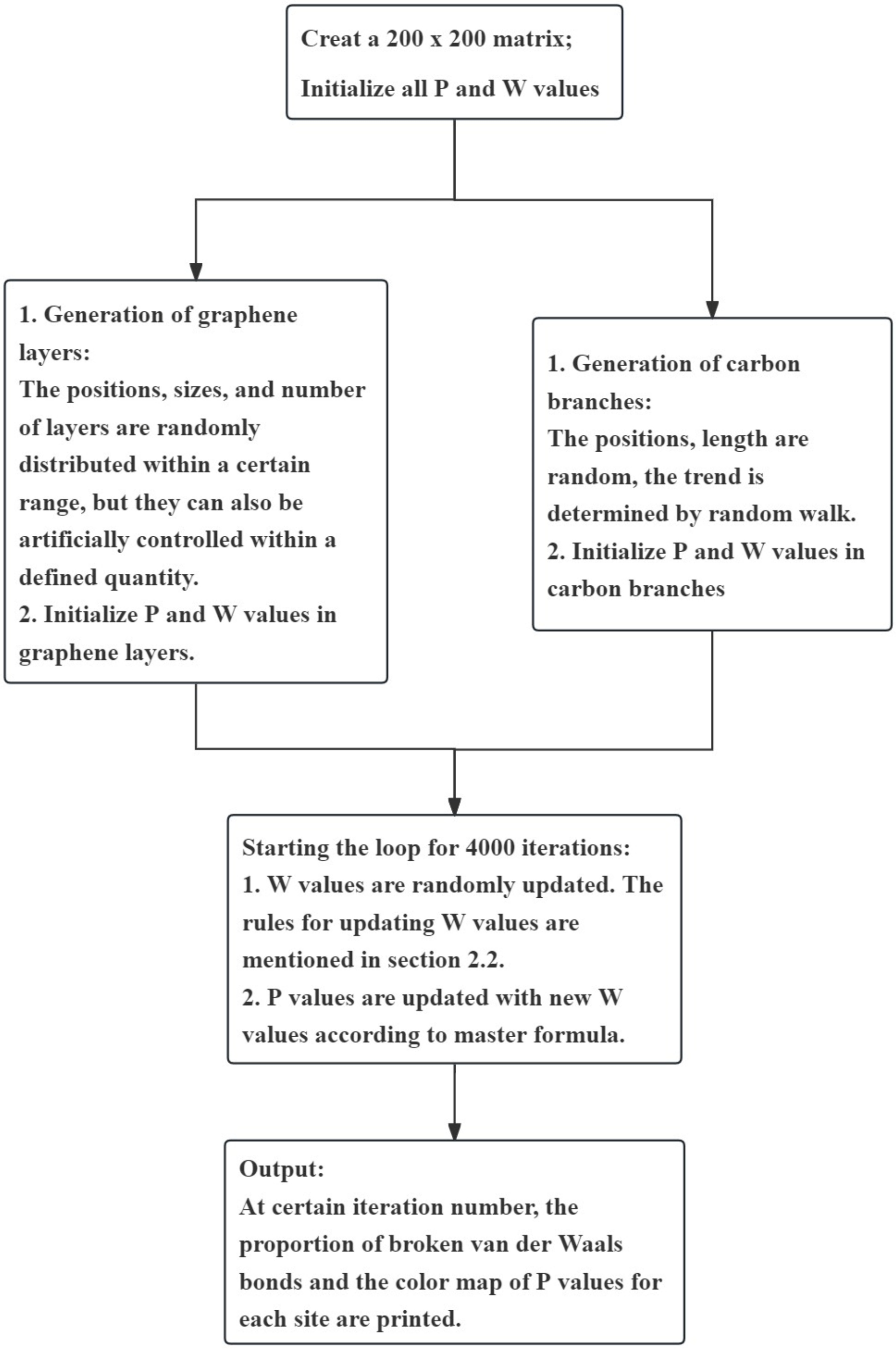

Figure 2.5 A simplified flow chart of the code.

3 Results and Discussion

3.1 Determination of appropriate s value

According to section 2.1, the propagation variable describes the ease with which strain propagates within coal particles and affects the display of the results. Therefore, an appropriate s value should be worked out before simulating different ranks of coal. We pre-simulated a smaller coal particle with a size of 100×100.

When the s value is 0.2, strain propagation is difficult (**Figure 3.1 (up)**). Due to the slow propagation speed, a relatively complete strain propagation process cannot be obtained within a reasonable simulating time scale (**Figure 3.1 (down)**). On the other hand, when the s value is 0.8, the curve diverges (**Figure 3.2 (up)**). The propagation of strain becomes uncontrollable (**Figure 3.2 (down)**). To describe the strain propagation process in coal particles more accurately and completely, the s value is set to 0.55 in the following simulations (**Figure 3.3**).

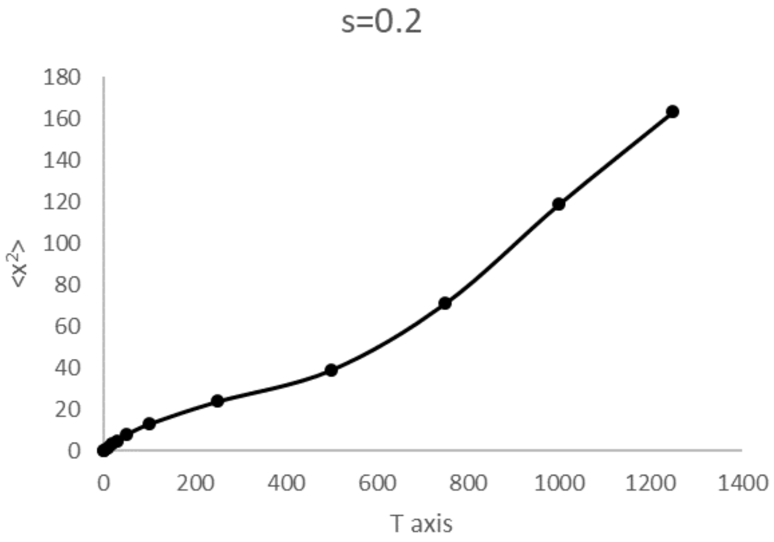

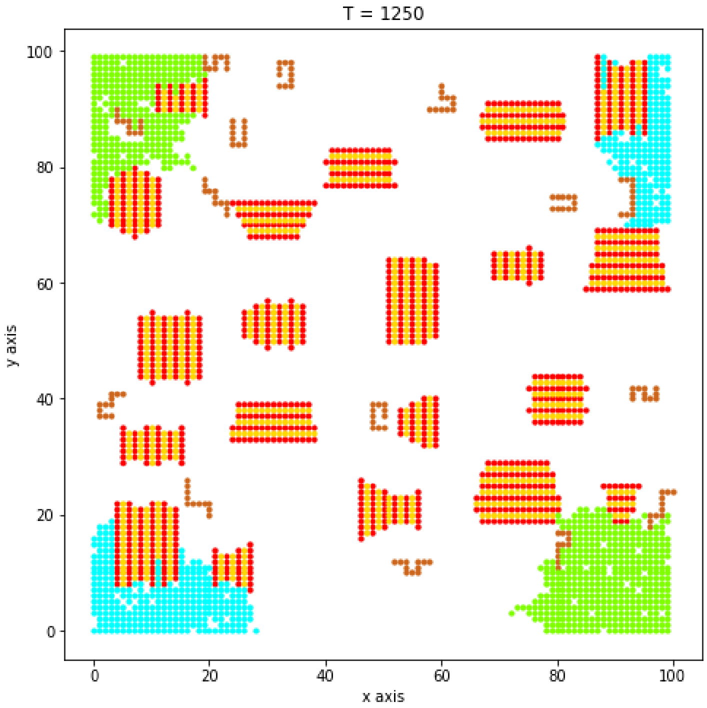

Figure 3.1 The plot of <x^2> vs T (up). When s=0.2, strain can hardly propagate. The simulated diagram shows the result diagram at T=1250 (down).

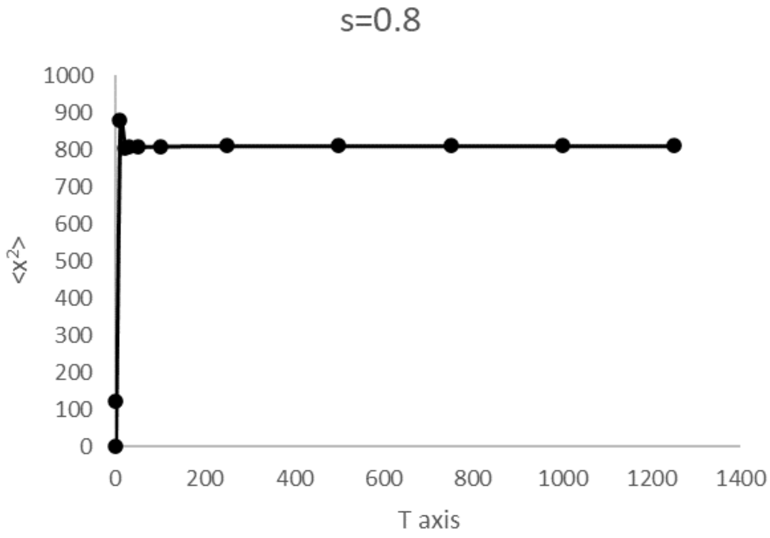

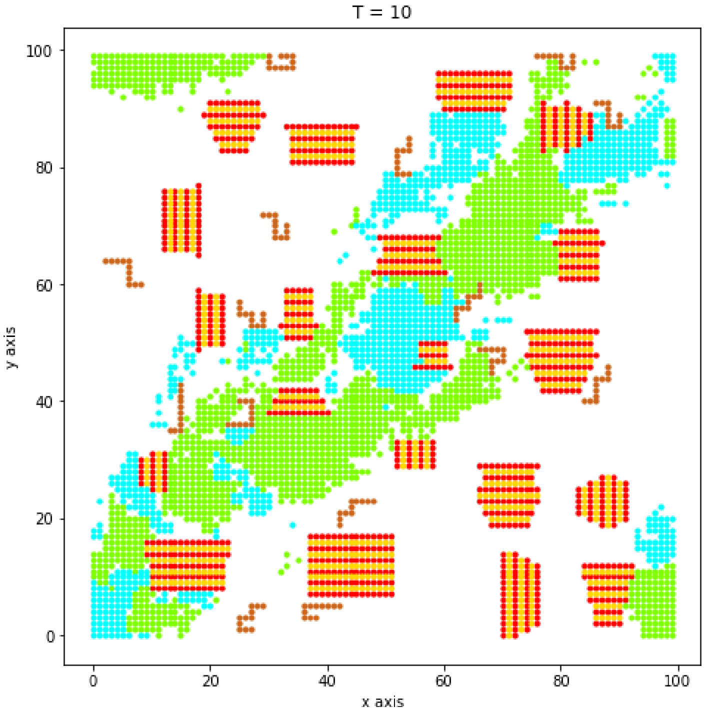

Figure 3.2 The plot of <x^2> vs T (up). When s=0.8, the curve diverges. The propagation of strain becomes uncontrollable. The simulated diagram shows the result diagram at T=10 (the jumping point in the curve) (down).

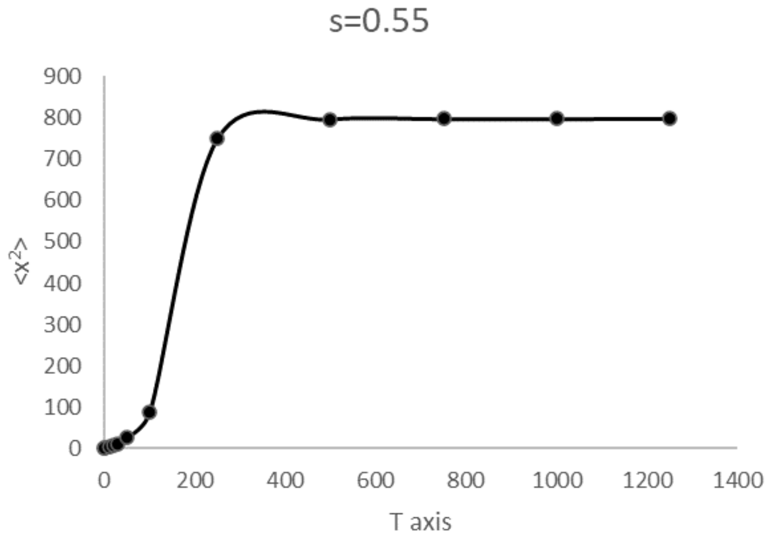

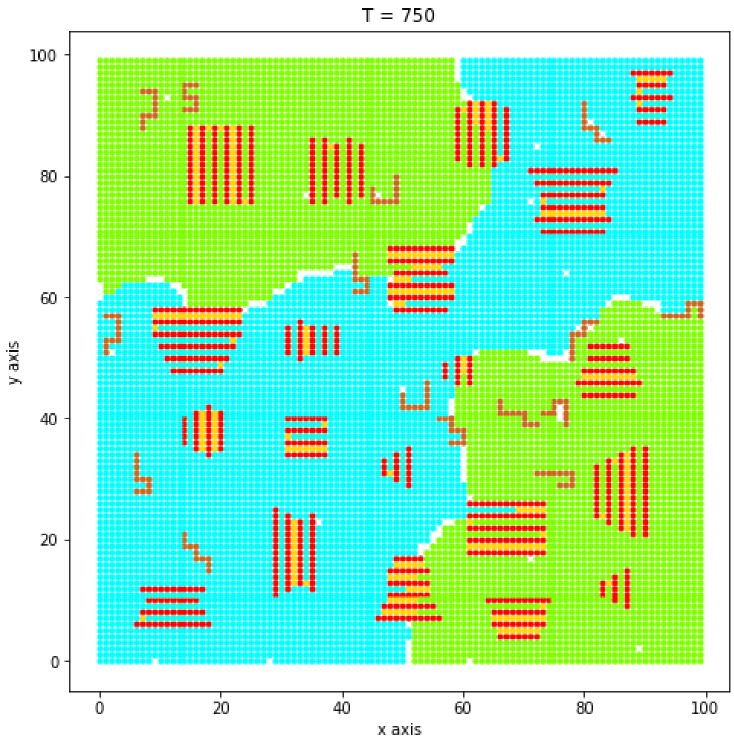

Figure 3.3 The plot of <x^2> vs T (up). When s=0.55, strain propagates in a proper speed. The simulated diagram shows the result diagram at T=750 (down).

3.2 Simulation for anthracite coal and bituminous coal

2D 200×200 square is created to simulate the propagation process of strain in different rank coal particles and study the breakage of vdW bonds between the graphite layers. **Figure 3.4-3.7** and **Figure 3.8-3.11** are the simulated diagrams of the simulated anthracite and bituminous coal particles at T=0, 100, 250, 500, 1000, 1500, 2000, and 2500 during the iterations. The graphite layers and vdW bonds are represented by red and yellow parallel lines. The sp^3 carbon branches are represented by brown broken lines. The breakage of the bonds occurs when the absolute value of P approaches 1. The blue color means P values at the sites reach 1, while the green color means P values at the sites reach -1.

Different types of coal have different sizes and amounts of crystallized structures (Saikia et al., 2019). Anthracite coal and bituminous coal particles are simulated by controlling the lateral length, vertical thickness, and the amount of graphite layers in the model of the coal particle.

In the simulation of anthracite coal particles, the lateral length and vertical thickness of graphite layers are controlled between [15, 30] units and [10,20] units, respectively. The proportion of crystal structures in the anthracite coal particle is 14.5%. As shown in **Figure 3.4-3.7**, vdW bonds start to be broken at the 250th iteration. After strain propagates through the whole particle, at the 2500th iteration, some small graphite structures can be exfoliated into single- or double-layer graphene, leading to the formation of CQDs. Meanwhile, some larger graphite structures cannot be peeled off. This result suggests that the applied shear stress cannot effectively break the vdW bonds between the graphite structures in anthracite coal.

On the other hand, when simulating bituminous coal particles, the lateral length and vertical thickness of graphite layers are controlled between [10, 20] units and [7,15] units, respectively. The proportion of crystal structures in bituminous coal particles is 10.2%. As shown in **Figure 3.8-3.11**, vdW bonds start to be broken at the 250th iteration. At the 2500th iteration, most graphite structures are exfoliated, indicating that the applied shear stress can break the vdW forces between the graphite structures in bituminous coal.

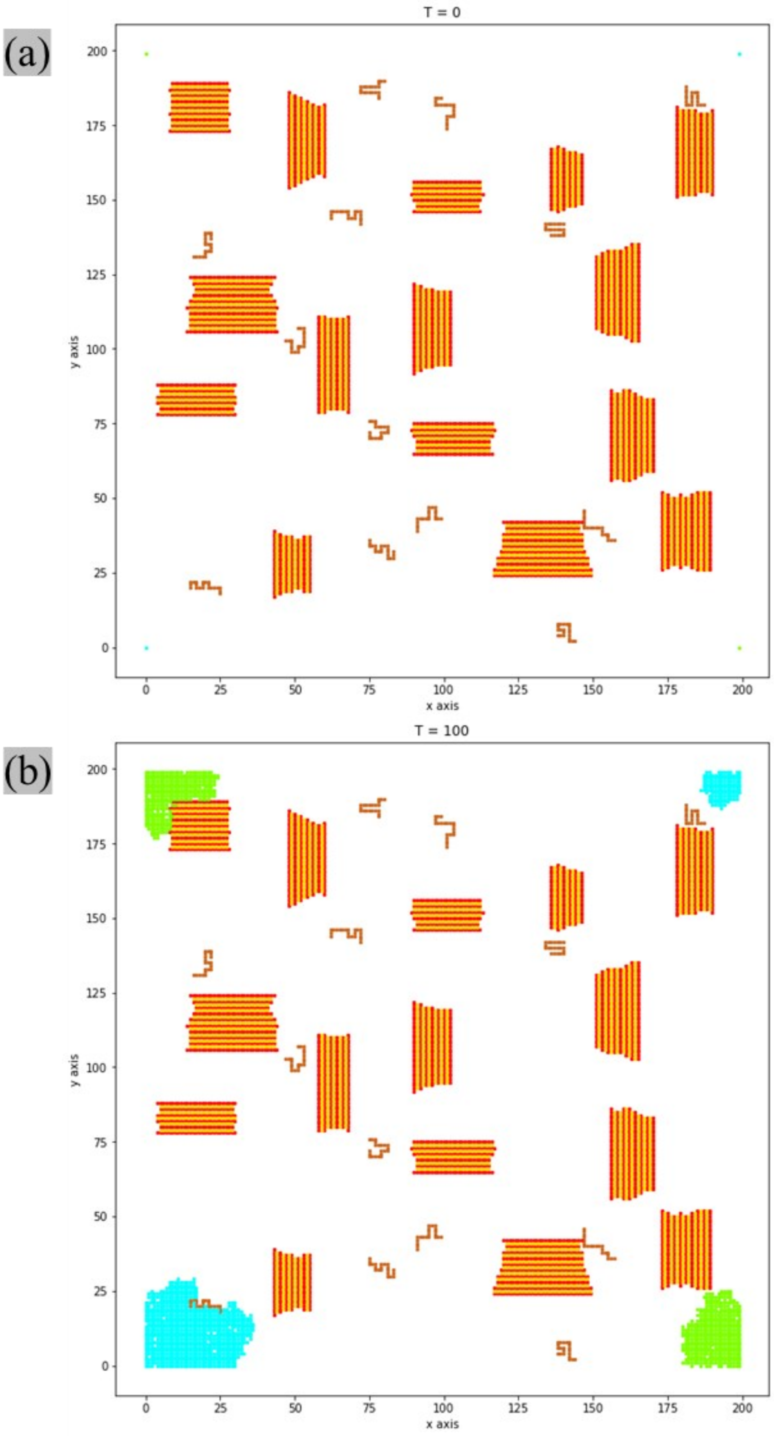

Figure 3.4 Simulated diagram of the strain propagation in anthracite particles at the (a) 0 and (b) 100th iterations.

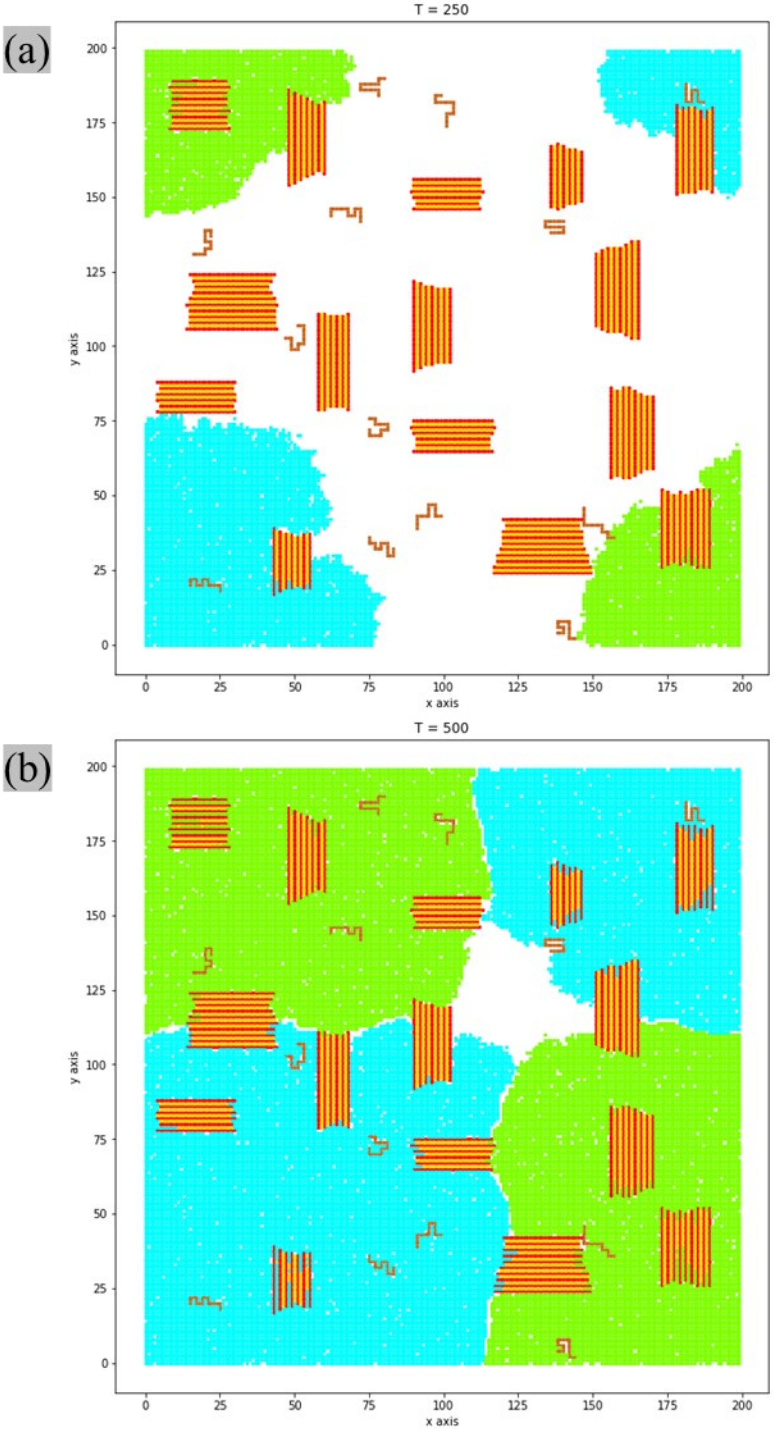

Figure 3.5 Simulated diagram of the strain propagation in anthracite particles at the (a) 250th and (b) 500th iterations.

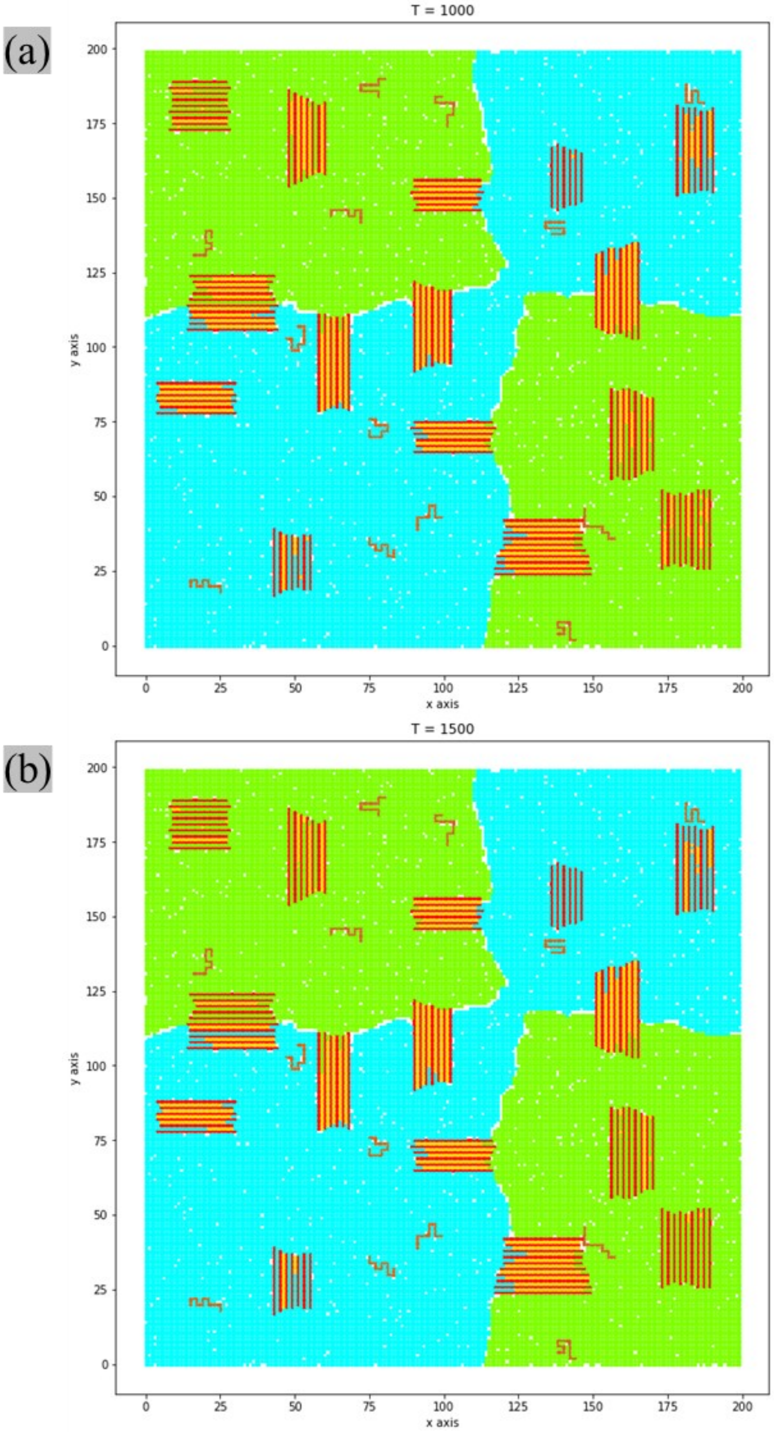

Figure 3.6 Simulated diagram of the strain propagation in anthracite particles at the (a) 1000th and (b) 1500th iterations.

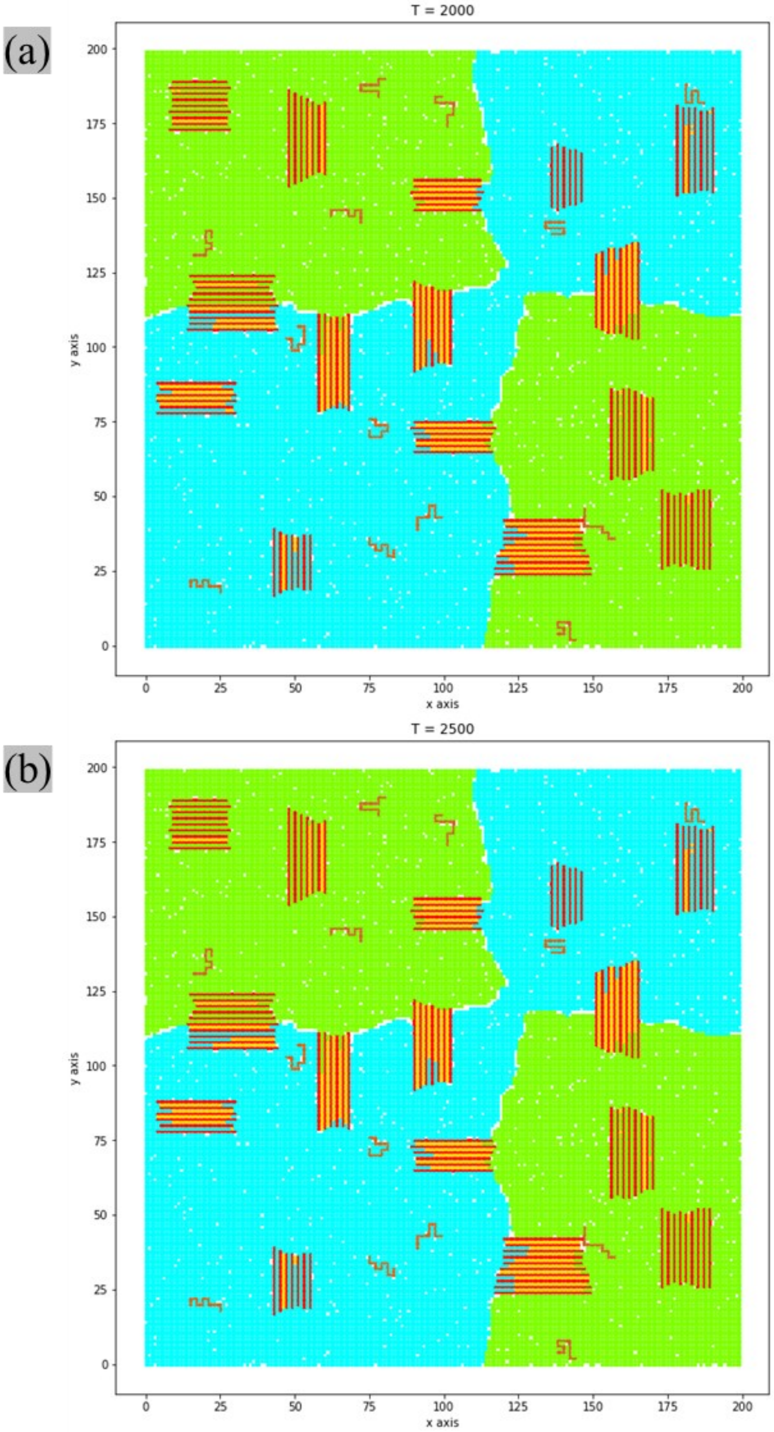

Figure 3.7 Simulated diagram of the strain propagation in anthracite particles at the (a) 2000th and (b) 2500th iterations.

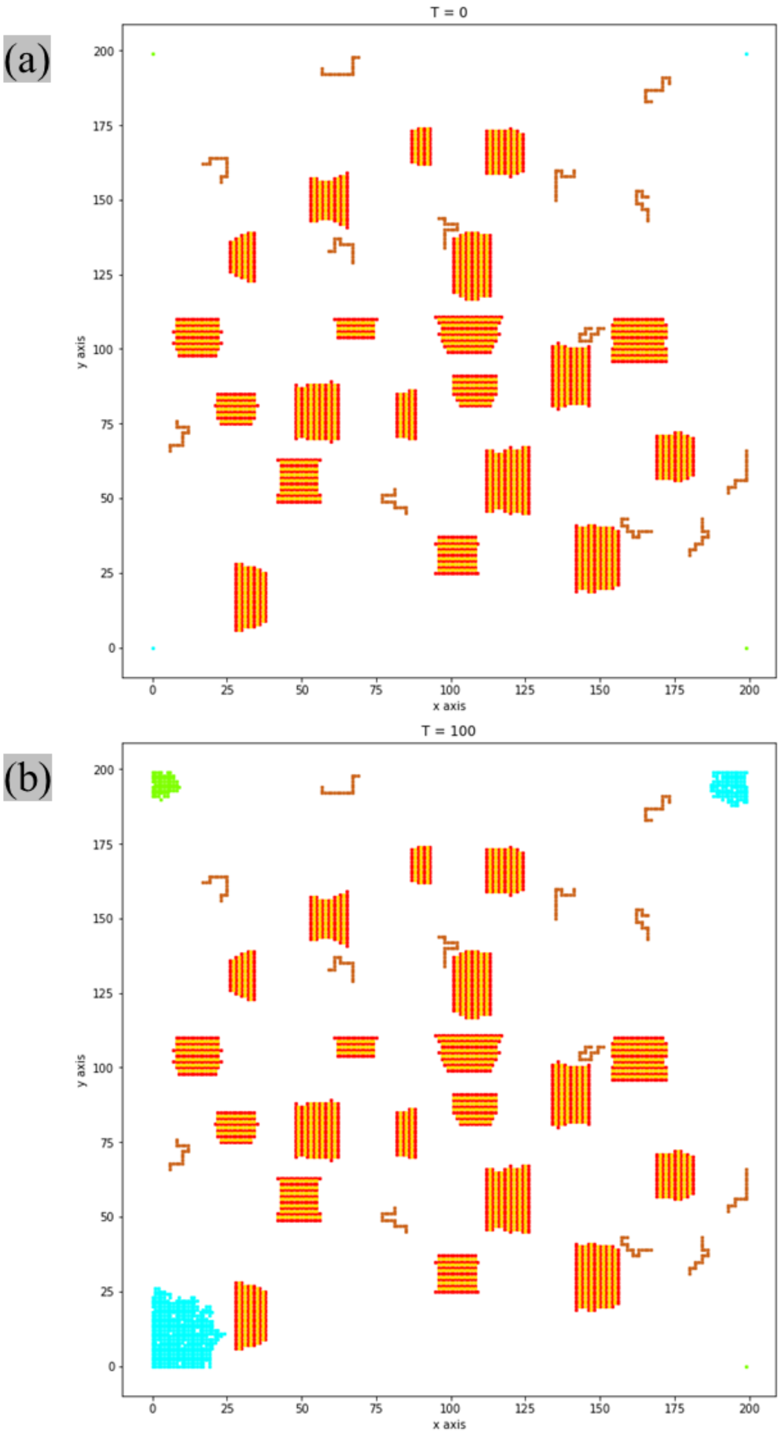

Figure 3.8 Simulated diagram of the strain propagation in bituminous particles at the (a) 0 and (b) 100th iterations.

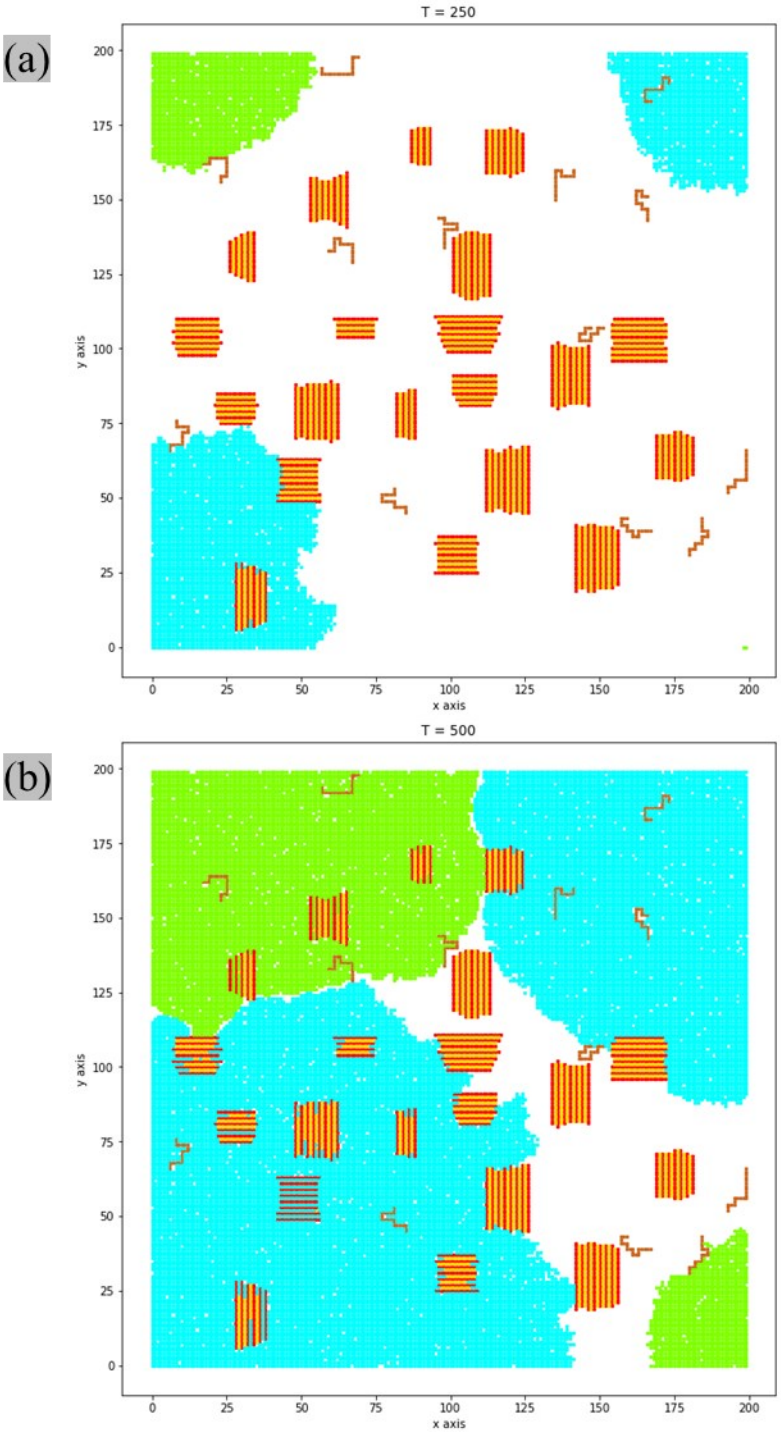

Figure 3.9 Simulated diagram of the strain propagation in bituminous particles at the (a) 250th and (b) 500th iterations.

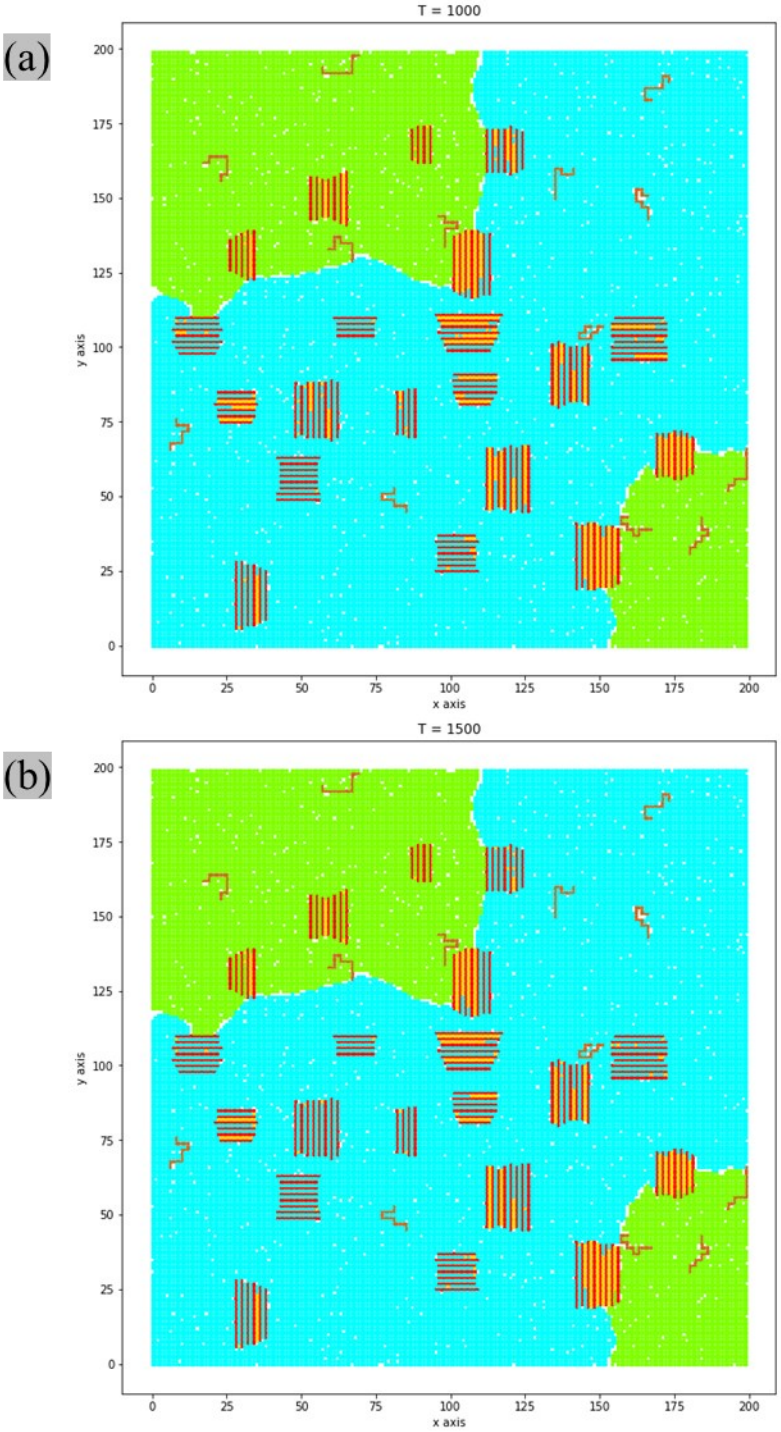

Figure 3.10 Simulated diagram of the strain propagation in bituminous particles at the (a) 1000th and (b) 1500th iterations.

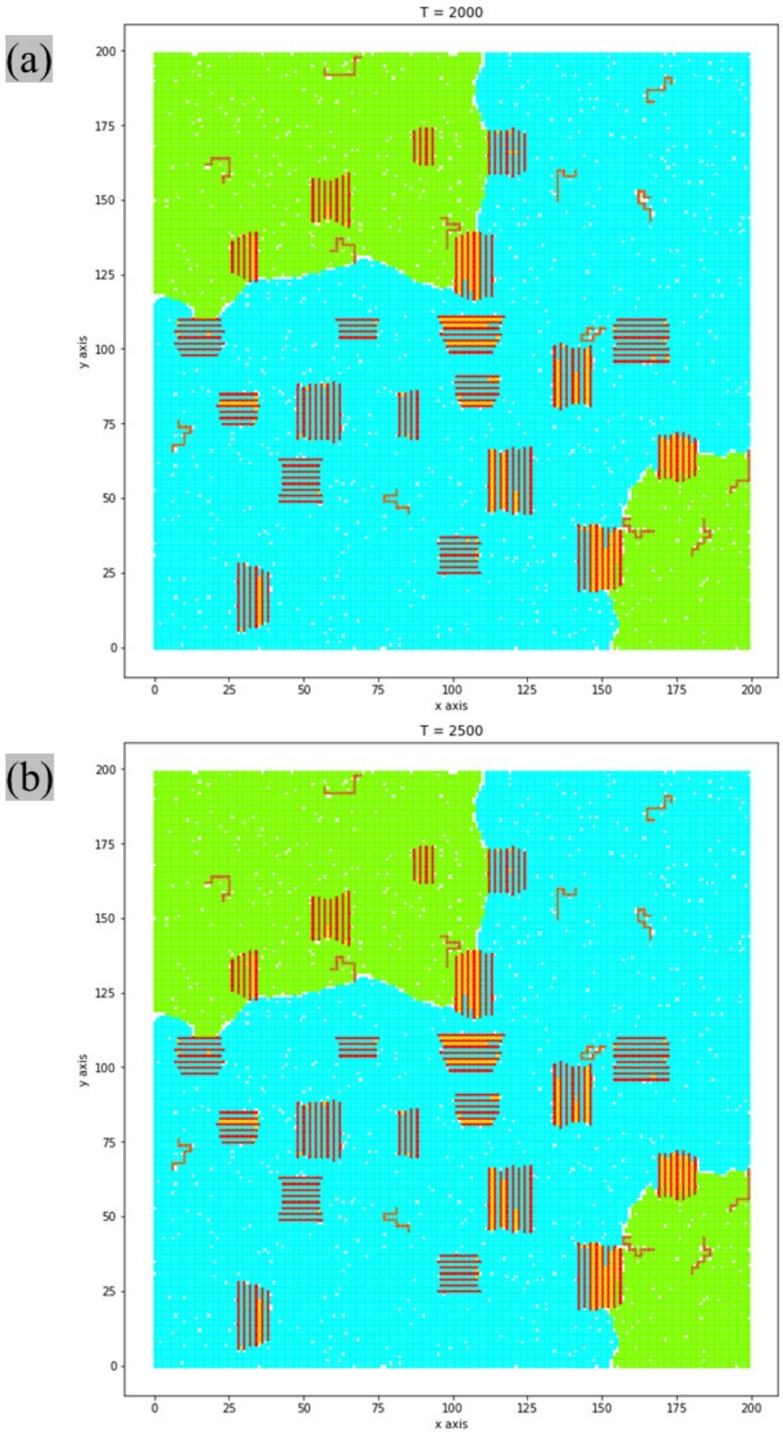

Figure 3.11 Simulated diagram of the strain propagation in bituminous particles at the (a) 2000th and (b) 2500th iterations.

To quantitatively describe the breakage of vdW bonds, a plot of the proportion of broken vdW bonds in simulated anthracite and bituminous coal particles against T is developed, as shown in **Figure 3.12**. According to the plot, the proportion of broken vdW bonds is 53.26% and 74.55% for anthracite coal and bituminous coal at T=2500. Compared with bituminous coal, anthracite coal particles have a higher proportion of crystalline structures and larger size of graphite layers. Thus, we can deduce that these differences lead to the lower proportion of broken vdW bonds in the simulated anthracite coal particles than that in the simulated bituminous coal particles.

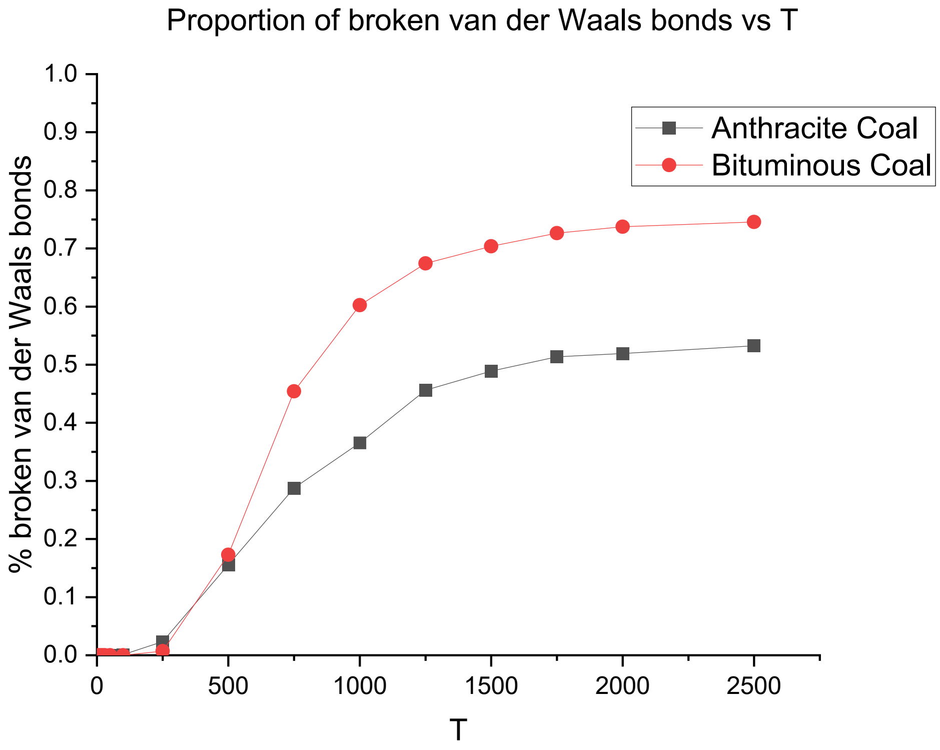

Figure 3.12 A plot of the proportion of broken van der Waals bonds in simulated anthracite and bituminous coal particles vs T.

3.3 Factors affecting the breakage of van der Waals bonds

To explore the effects of the vertical thickness and lateral length of graphite layers on vdW bonds breakage, a controlling variable method is used to simulate a series of 'fake' coal particles.

Firstly, 2D 200×200 square coal particles are generated with a fixed lateral length of 15 units. When the vertical thicknesses of graphite layers are 5, 9, 13, and 17, the proportion of broken vdW bonds is plotted against the time step T, as shown in **Figure 3.13**. The vdW bonds start to break from the 250th iteration, followed by the steeply ascending of the curve within the first 1000 iterations, eventually stabilizing after 2000 iterations. This is consistent with the simulation results in Section 3.2. At the 4000th iteration, we observe that thicker graphite structures, i.e. more layers of graphite, result in a lower proportion of vdW bonds breakage. To visually demonstrate this relationship, we plot the proportion of vdW bonds breakage against the vertical thickness ranging from 5 to 25 units at T=4000 (**Figure 3.14**). We found that as the thickness increases from 5 to around 17, the proportion of broken vdW bonds decreases from 88.9% to 80.8%. However, as the thickness continued to increase, the curve exhibited an upward trend. The reason for this might be that at this range, the length of the graphite structure is much smaller than its thickness, and such structures are less common in the natural state. The corresponding simulated diagrams are provided in **Figure 3.15-3.17**.

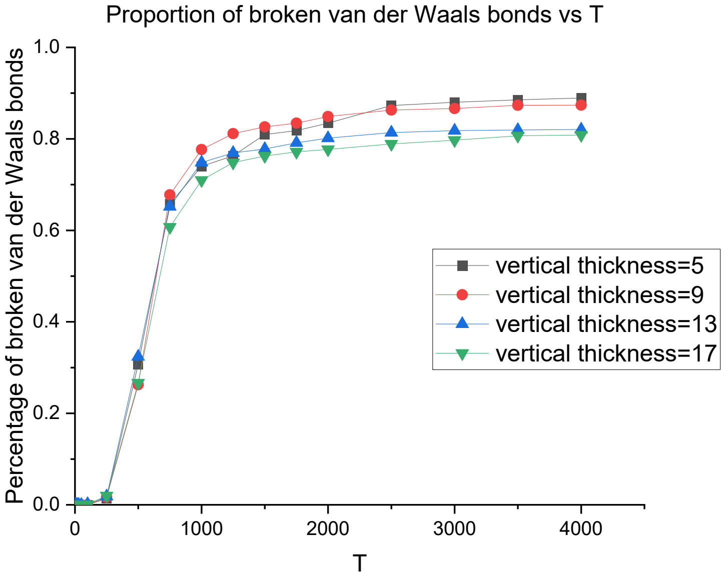

Figure 3.13 Proportion of broken van der Waals bonds against T with fixed lateral length of 15 units and vertical thickness of 5, 9, 13, 17 units.

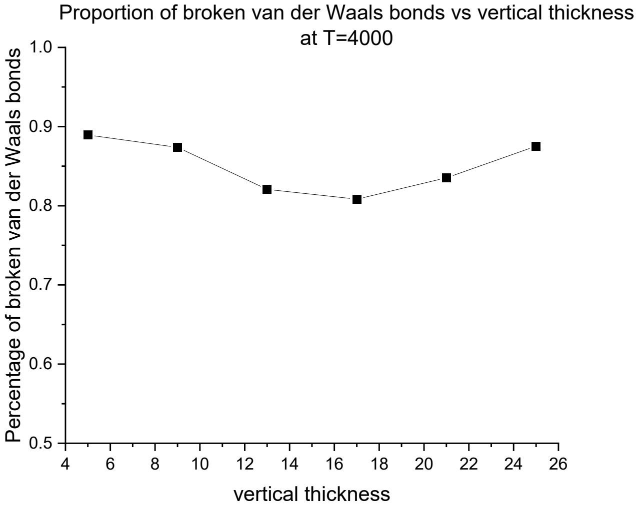

Figure 3.14 Proportion of broken van der Waals bonds against vertical thickness of graphite structures at T=4000 with fixed lateral length of 15 units.

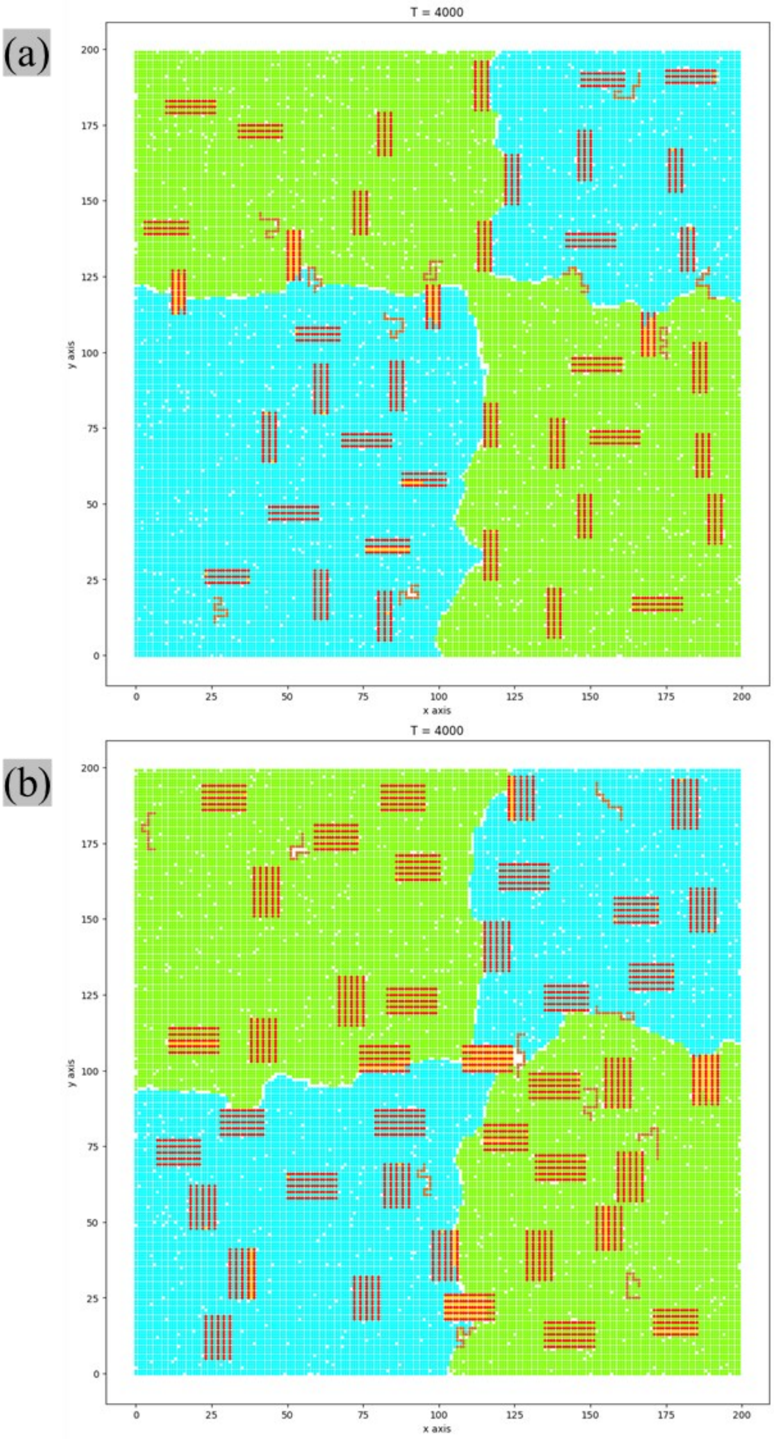

Figure 3.15 Simulated diagram of coal particle at T=4000. The parameters of graphite structures are fixed lateral length of 15 units and vertical thickness (a) 5 units, (b) 9 units.

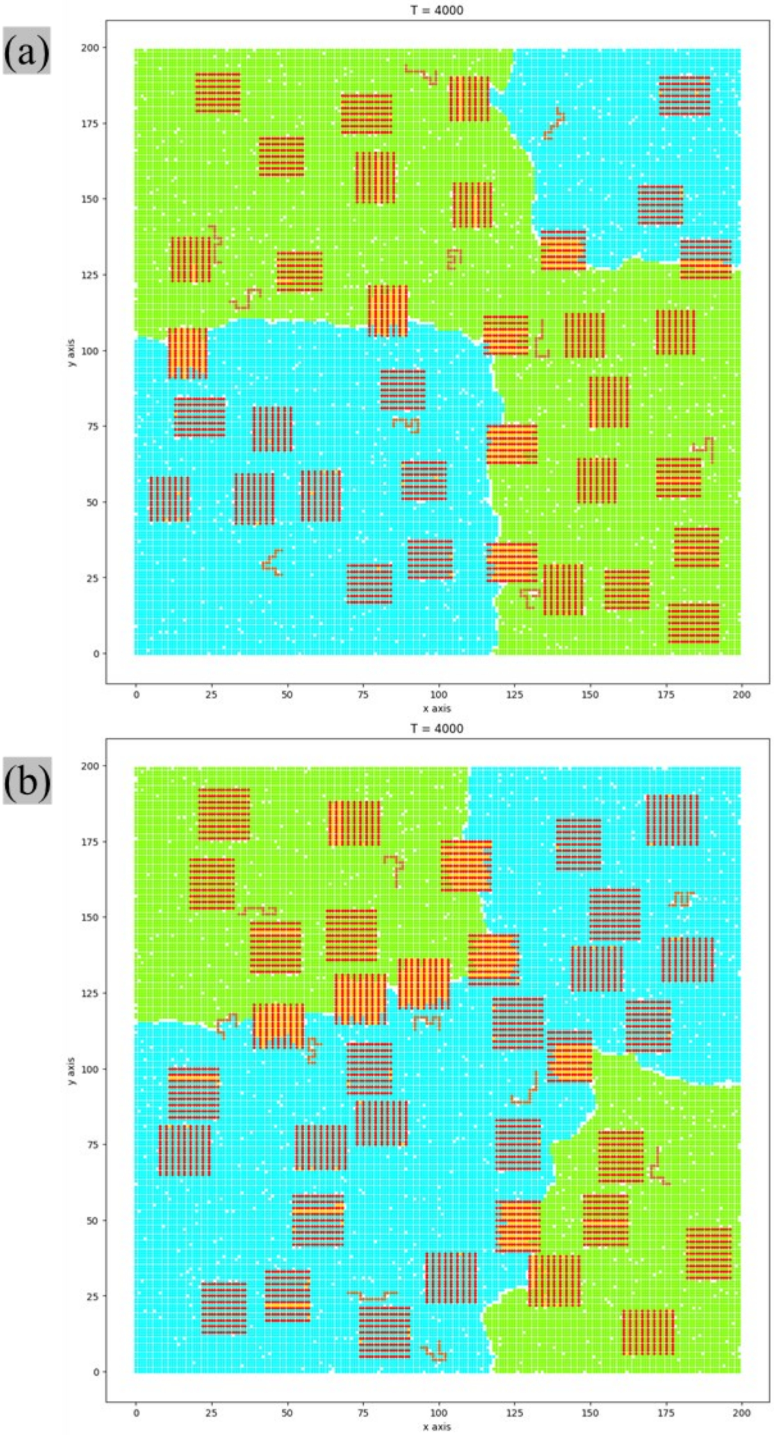

Figure 3.16 Simulated diagram of coal particle at T=4000. The parameters of graphite structures are fixed lateral length of 15 units and vertical thickness (a) 13 units, (b) 17 units.

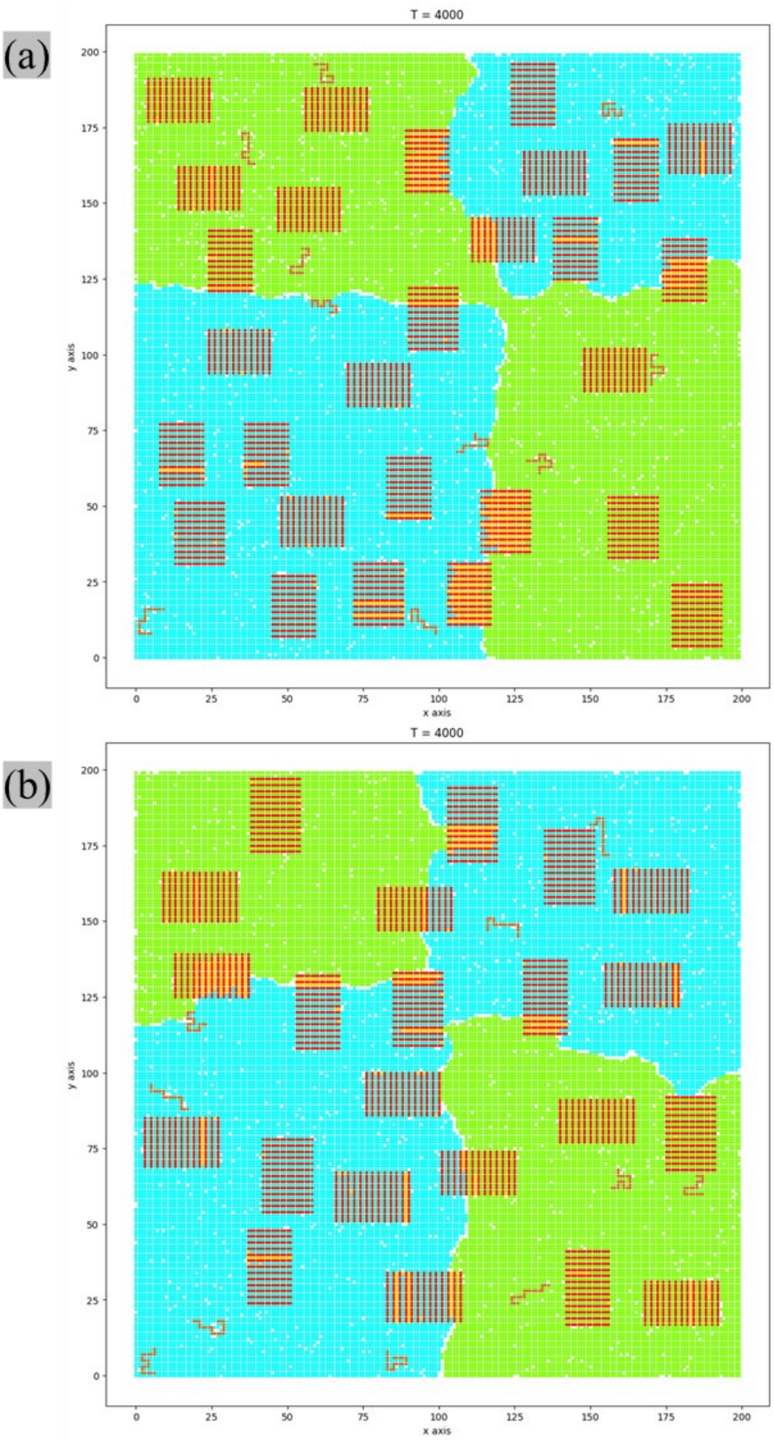

Figure 3.17 Simulated diagram of coal particle at T=4000. The parameters of graphite structures are fixed lateral length of 15 units and vertical thickness (a) 21 units, (b) 25 units.

Secondly, we fixed the thickness of graphite structures at 13 units while varying the length from 12 to 22 units. The plot of the proportion of broken vdW bonds against the T is shown in **Figure 3.18**. At the 4000th iteration, it can be induced that the longer the lateral length of graphite layers, the lower the proportion of broken vdW bonds. This relationship is revealed in **Figure 3.19**. Y-axis values drop from 85.9% to 75.0% as the lateral lengths increase from 12 to 22 units. This result indicates that the longer length of the graphite layers leads to the more difficult breakage of vdW. The corresponding simulated diagrams are provided in **Figure 3.20-3.22**.

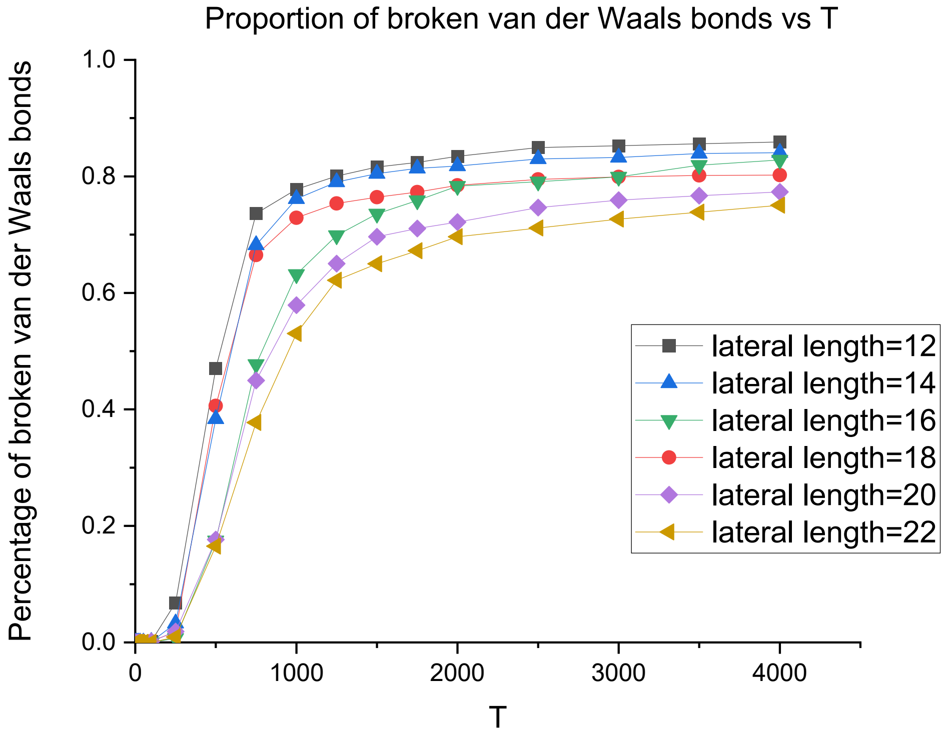

Figure 3.18 Proportion of broken van der Waals bonds against T with fixed vertical thickness of 13 units and lateral length of 12, 14, 16, 18, 20, 22 units.

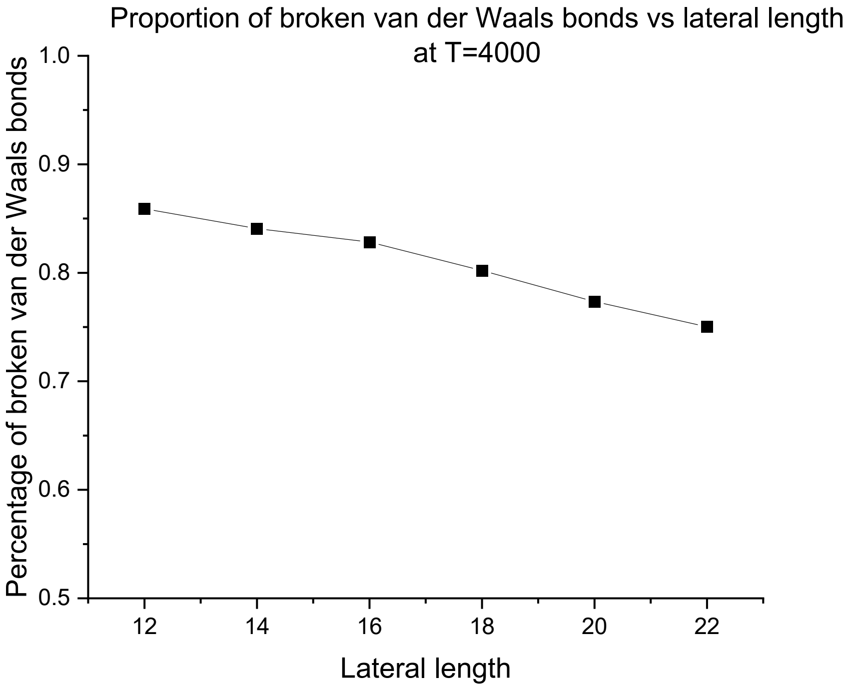

Figure 3.19 Proportion of broken van der Waals bonds against lateral length of graphite structures at T=4000 with fixed verticle thickness of 13 units.

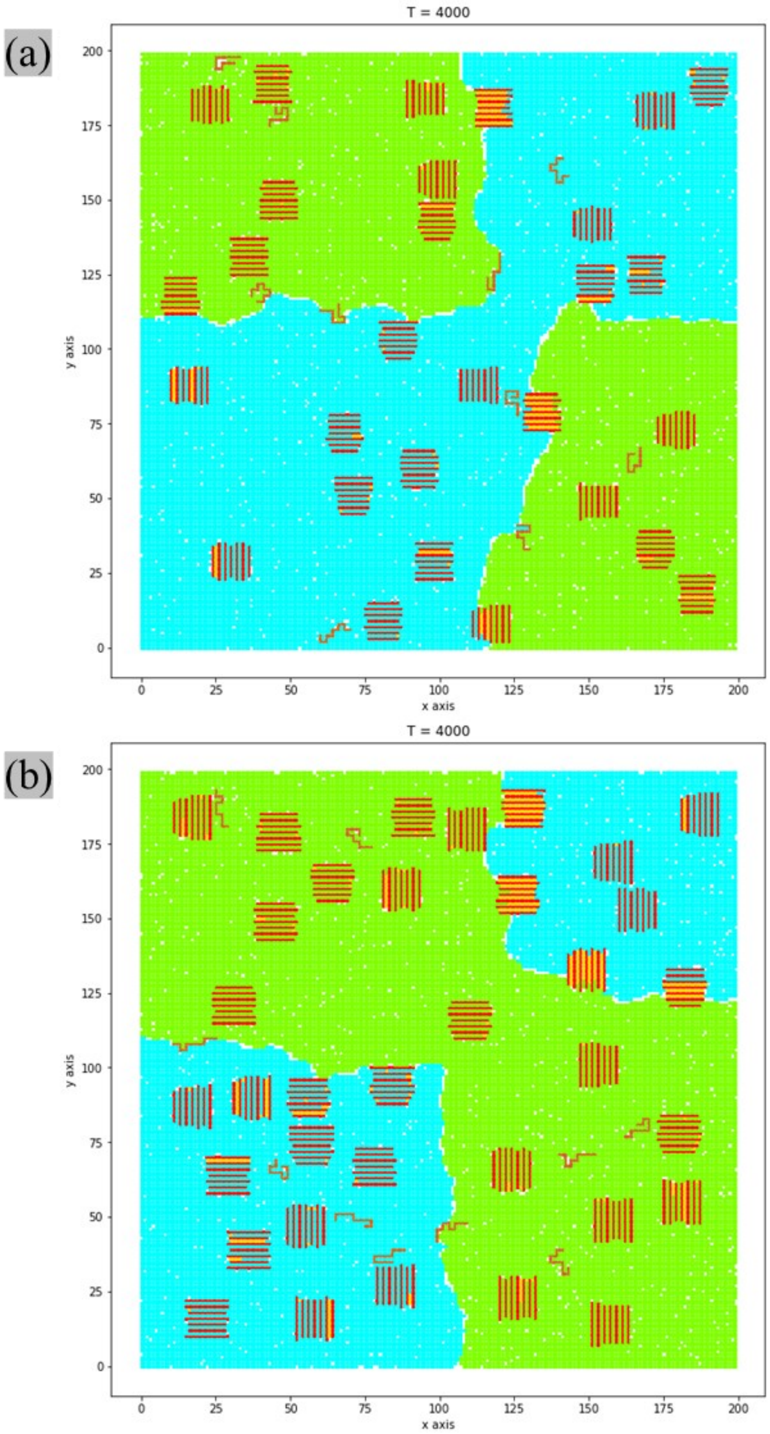

Figure 3.20 Simulated diagram of coal particle at T=4000. The parameters of graphite structures are fixed vertical thickness of 13 units and lateral length (a) 12 units, (b) 14 units.

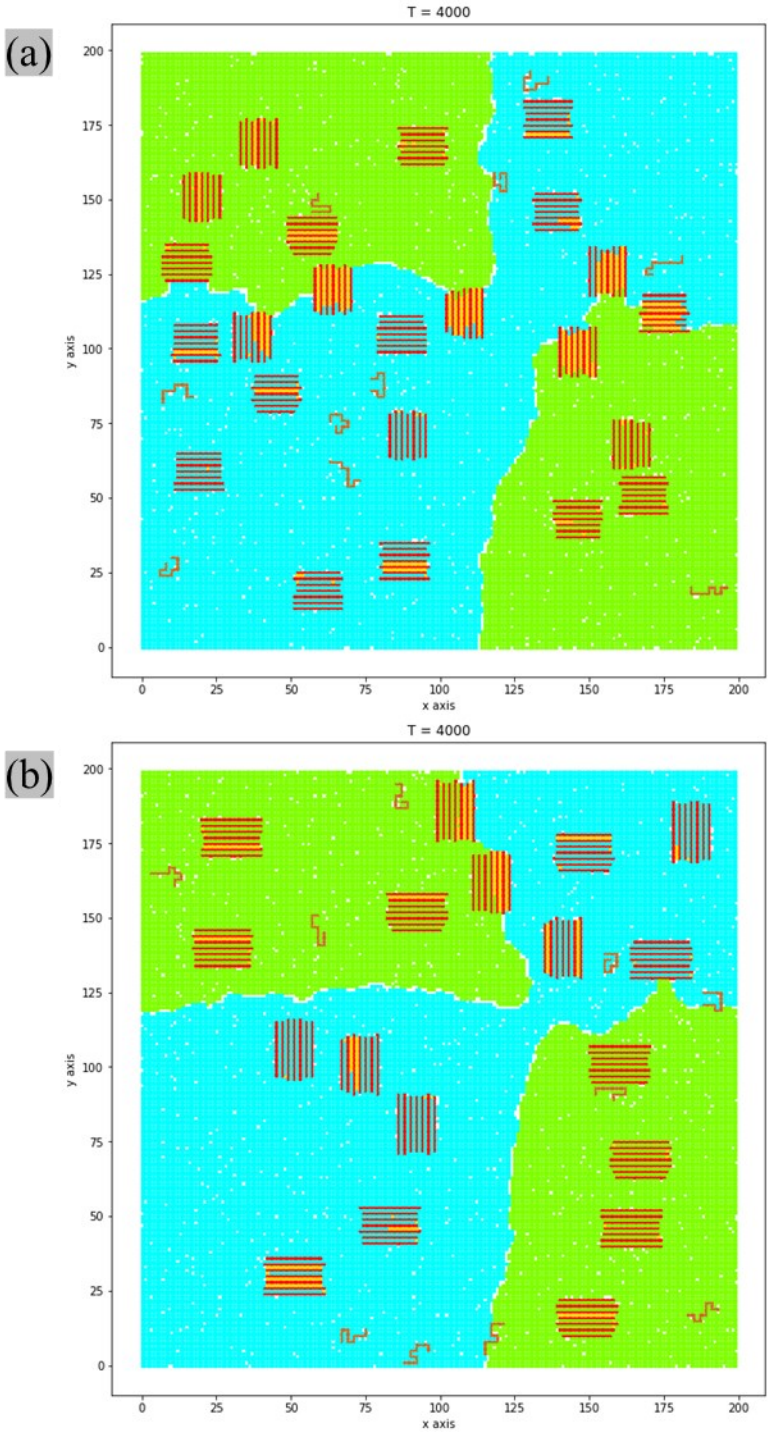

Figure 3.21 Simulated diagram of coal particle at T=4000. The parameters of graphite structures are fixed vertical thickness of 13 units and lateral length (a) 16 units, (b) 18 units.

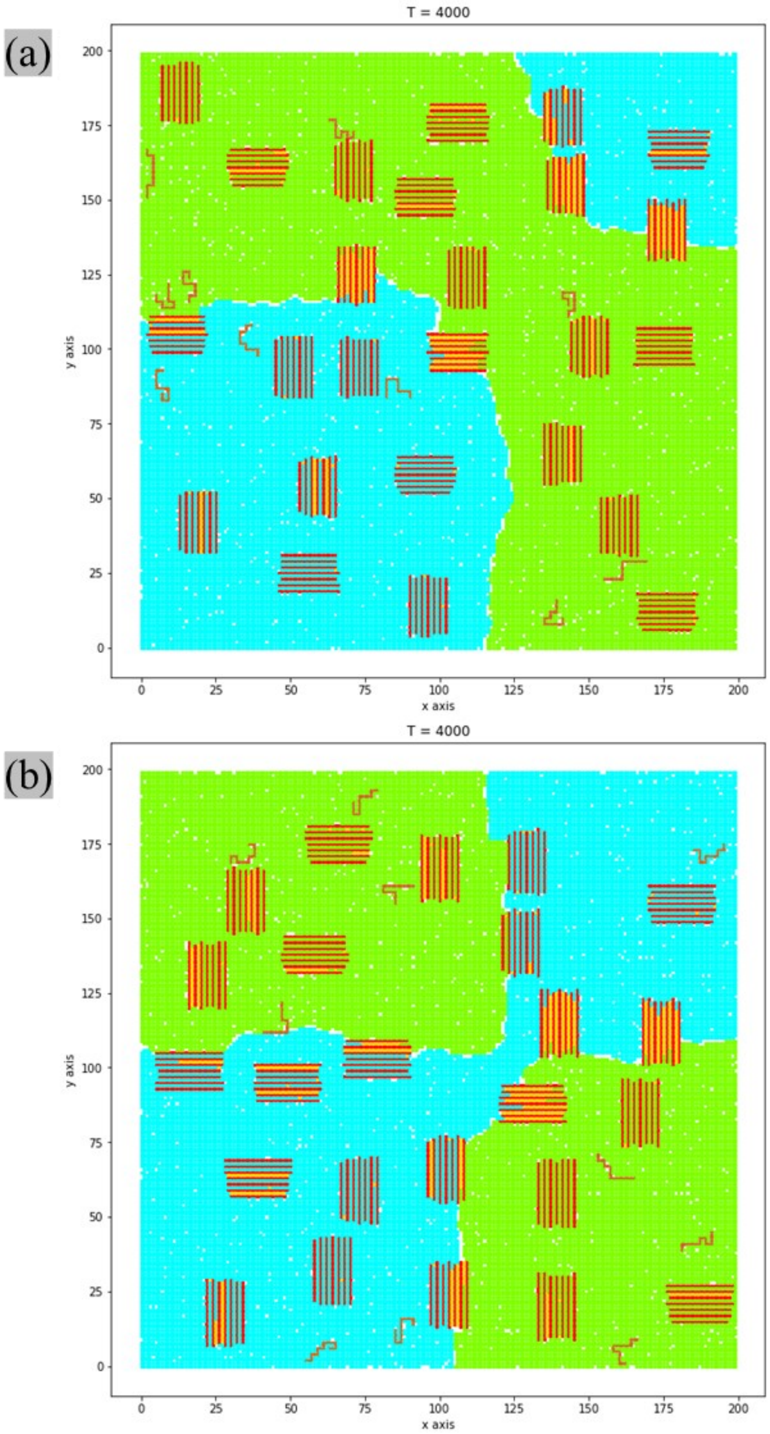

Figure 3.22 Simulated diagram of coal particle at T=4000. The parameters of graphite structures are fixed vertical thickness of 13 units and lateral length (a) 20 units, (b) 22 units.

Combining the results of the two simulations, we found that the smaller the size of the graphite layer structures within coal particles, the more amount of the interlayer vdW bonds can be broken. This finding corroborates the simulation results for bituminous and anthracite coals in section 3.2. Returning to our initial problems, the results provide evidence for the possibility of the breakage of vdW bonds between graphite layers by shear stress. However, the exfoliation of graphite layers depends on their size: the larger the graphite structure, the lower the efficiency of exfoliation. Therefore, it is advisable to select coal types with smaller graphite layer structures as raw materials to produce CQDs. In nature, coal types with smaller graphite structures typically indicate a lower rank of coal, but this also implies a reduction in the amount of crystalline carbon structures, thereby affecting the final yield. This represents a trade-off.

4 Conclusion

This study explores the microscopic mechanism of preparing coal-based CQDs by ball milling. The breakage of vdW bonds between graphite layers in coal particles was obtained by applying shear stress to the simulated coal particles. The proportions of broken vdW bonds in anthracite and bituminous coal particles were found to be 53.26% and 74.55%, respectively. The graphite layers in anthracite coal particles could not be exfoliated sufficiently. Further controlled variable simulations demonstrated that this significant difference is due to the larger size of graphite layers in anthracite coal compared to that of bituminous coal. This study offers novel insights into the feasibility of preparing CQDs from coal by ball milling and offers guidance for the selection of raw coal materials.

5 Future Work

In future work, practical experiments using ball milling for the synthesis of coal-based CQDs need to be conducted to validate our simulated results. Additionally, trying to build larger-scale simulations, such as simulating larger coal particles and employing three-dimensional models, can further improve the simulation results.

6 References

Al Jahdaly, B. A., Elsadek, M. F., Ahmed, B. M., Farahat, M. F., Taher, M. M., & Khalil, A. M. (2021). Outstanding Graphene Quantum Dots from Carbon Source for Biomedical and Corrosion Inhibition Applications: A Review. *Sustainability*, *13*(4). https://doi.org/10.3390/su13042127

Bourlinos, A. B., Stassinopoulos, A., Anglos, D., Zboril, R., Karakassides, M., & Giannelis, E. P. (2008). Surface functionalized carbogenic quantum dots. *Small*, *4*(4), 455-458. https://doi.org/10.1002/smll.200700578

Chen, G. X., Wu, S. L., Hui, L. W., Zhao, Y., Ye, J. L., Tan, Z. Q., Zeng, W. C., Tao, Z. C., Yang, L. H., & Zhu, Y. W. (2016). Assembling carbon quantum dots to a layered carbon for high-density supercapacitor electrodes. *Scientific Reports*, *6*. https://doi.org/10.1038/srep19028

Chen, Q. L., Wang, C. F., & Chen, S. (2013). One-step synthesis of yellow-emitting carbogenic dots toward white light-emitting diodes. *Journal of Materials Science*, *48*(6), 2352-2357. https://doi.org/10.1007/s10853-012-7016-8

Cui, L., Ren, X., Wang, J., & Sun, M. (2020). Synthesis of homogeneous carbon quantum dots by ultrafast dual-beam pulsed laser ablation for bioimaging. *Materials Today Nano*, *12*. https://doi.org/10.1016/j.mtnano.2020.100091

Das, R., Bandyopadhyay, R., & Pramanik, P. (2018). Carbon quantum dots from natural resource: A review. *Materials Today Chemistry*, *8*, 96-109. https://doi.org/10.1016/j.mtchem.2018.03.003

Demchenko, A. P., & Dekaliuk, M. O. (2013). Novel fluorescent carbonic nanomaterials for sensing and imaging. *Methods and Applications in Fluorescence*, *1*(4). https://doi.org/10.1088/2050-6120/1/4/042001

Ding, Y. F., Zhang, F., Xu, J. C., Miao, Y. Q., Yang, Y. Z., Liu, X. G., & Xu, B. S. (2017). Synthesis of short-chain passivated carbon quantum dots as the light emitting layer towards electroluminescence. *RSC Advances*, *7*(46), 28754-28762. https://doi.org/10.1039/c7ra02421e

Essner, J. B., Kist, J. A., Polo-Parada, L., & Baker, G. A. (2018). Artifacts and Errors Associated with the Ubiquitous Presence of Fluorescent Impurities in Carbon Nanodots. *Chemistry of Materials*, *30*(6), 1878-1887. https://doi.org/10.1021/acs.chemmater.7b04446

Gao, J., Zhao, S. Q., Guo, S. J., Wang, H. B., Sun, Y., Yao, B. W., Liu, Y., Huang, H., & Kang, Z. H. (2019). Carbon quantum dot-covered porous Ag with enhanced activity for selective electroreduction of CO_2 to CO. *Inorganic Chemistry Frontiers*, *6*(6), 1453-1460. https://doi.org/10.1039/c9qi00217k

Gao, Q. C., Yuan, Z. M., Yang, G. H., Tian, Z. J., Jiang, Z. Y., Zhang, K., Wang, C., & Chen, J. C. (2021). Enhancement of lignin-based carbon quantum dots from poplar pre-hydrolysis liquor on photocatalytic CO_2 reduction via TiO_2 nanosheets.

Industrial Crops and Products, *160*. https://doi.org/10.1016/j.indcrop.2020.113161

Gao, X. H., Du, C., Zhuang, Z. H., & Chen, W. (2016). Carbon quantum dot-based nanoprobes for metal ion detection. *Journal of Materials Chemistry C*, *4*(29), 6927-6945. https://doi.org/10.1039/c6tc02055k

Gu, Z. G., Li, D. J., Zheng, C., Kang, Y., Wöll, C., & Zhang, J. (2017). MOF-Templated Synthesis of Ultrasmall Photoluminescent Carbon-Nanodot Arrays for Optical Applications. *Angewandte Chemie-International Edition*, *56*(24), 6853-6858. https://doi.org/10.1002/anie.201702162

Han, Y. W., Chen, Y., Wang, N., & He, Z. H. (2019). Magnesium doped carbon quantum dots synthesized by mechanical ball milling and displayed Fe^{3+} sensing. *Materials Technology*, *34*(6), 336-342. https://doi.org/10.1080/10667857.2018.1556469

Hoang, V. C., Hassan, M., & Gomes, V. G. (2018). Coal derived carbon nanomaterials – Recent advances in synthesis and applications. *Applied Materials Today*, *12*, 342-358. https://doi.org/10.1016/j.apmt.2018.06.007

Hu, M. Y., Guo, D. M., Tang, J., Liu, K., Lian, H. L., Xu, C. Y., Xu, L., & Zhang, W. Q. (2022). Temperature Sensing Performance of Fluorescent Carbon Quantum Dots Prepared from Loblolly Pine Processing Waste. *Russian Journal of Physical Chemistry A*, *96*(14), 3070-3081. https://doi.org/10.1134/S0036024423030202

Hu, S., Wei, Z., Chang, Q., Trinchi, A., & Yang, J. (2016). A facile and green method towards coal-based fluorescent carbon dots with photocatalytic activity. *Applied Surface Science*, *378*, 402-407. https://doi.org/10.1016/j.apsusc.2016.04.038

Huang, J. J., Zhong, Z. F., Rong, M. Z., Zhou, X., Chen, X. D., & Zhang, M. Q. (2014). An easy approach of preparing strongly luminescent carbon dots and their polymer based composites for enhancing solar cell efficiency. *Carbon*, *70*, 190-198. https://doi.org/10.1016/j.carbon.2013.12.092

Jamila, G. S., Sajjad, S., Leghari, S. A. K., Kallio, T., & Flox, C. (2022). Glucose derived carbon quantum dots on tungstate-titanate nanocomposite for hydrogen energy evolution and solar light catalysis. *Journal of Nanostructure in Chemistry*, *12*(4), 611-623. https://doi.org/10.1007/s40097-021-00433-6

Jeong, G., Lee, J. M., Lee, J. A., Praneerad, J., Choi, C. A., Supchocksoonthorn, P., Roy, A. K., Chae, W. S., Paoprasert, P., Yeo, M. K., Murali, G., Park, S. Y., Lee, D. K., & In, I. (2021). Microwave-assisted synthesis of multifunctional fluorescent carbon quantum dots from A_4/B_2 polyamidation monomer sets. *Applied Surface Science*, *542*. https://doi.org/10.1016/j.apsusc.2020.148471

Jin, J., Chen, C., Li, H., Cheng, Y., Xu, L., Dong, B., Song, H., & Dai, Q. (2017). Enhanced Performance and Photostability of Perovskite Solar Cells by Introduction of Fluorescent Carbon Dots. *ACS Appl Mater Interfaces*, *9*(16), 14518-14524. https://doi.org/10.1021/acsami.7b02242

Karakoçak, B. B., Liang, J., Kavadiya, S., Berezin, M. Y., Biswas, P., & Ravi, N. (2018). Optimizing the Synthesis of Red-Emissive Nitrogen-Doped Carbon Dots for Use in Bioimaging. *Acs Applied Nano Materials*, *1*(7), 3682-3692. https://doi.org/10.1021/acsanm.8b00799

Ke, J., Li, X. Y., Zhao, Q. D., Liu, B. J., Liu, S. M., & Wang, S. B. (2017). Upconversion carbon quantum dots as visible light responsive component for efficient enhancement of photocatalytic performance. *Journal of Colloid And Interface Science*, *496*, 425-433. https://doi.org/10.1016/j.jcis.2017.01.121

Kim, J., Park, J., Kim, H., Singha, K., & Kim, W. J. (2013). Transfection and intracellular trafficking properties of carbon dot-gold nanoparticle molecular assembly conjugated with PEI-pDNA. *Biomaterials*, *34*(29), 7168-7180. https://doi.org/10.1016/j.biomaterials.2013.05.072

Kooshki, H., Sobhani-Nasab, A., Eghbali-Arani, M., Ahmadi, F., Ameri, V., & Rahimi-Nasrabadi, M. (2019). Eco-friendly synthesis of $PbTiO_3$ nanoparticles and $PbTiO_3$/carbon quantum dots binary nano-hybrids for enhanced photocatalytic performance under visible light. *Separation and Purification Technology*, *211*, 873-881. https://doi.org/10.1016/j.seppur.2018.10.057

Kuang, W. C., Zhong, Q., Ye, X. L., Yan, Y. Y., Yang, Y. H., Zhang, J. X., Huang, L. H., Tan, S. Z., & Shi, Q. S. (2019). Antibacterial Nanorods Made of Carbon Quantum Dots-ZnO Under Visible Light Irradiation. *Journal of Nanoscience and Nanotechnology*, *19*(7), 3982-3990. https://doi.org/10.1166/jnn.2019.16320

Li, H. L., Zhai, J. F., Tian, J. Q., Luo, Y. L., & Sun, X. P. (2011). Carbon nanoparticle for highly sensitive and selective fluorescent detection of mercury(II) ion in aqueous solution. *Biosensors & Bioelectronics*, *26*(12), 4656-4660. https://doi.org/10.1016/j.bios.2011.03.026

Li, H. L., Zhang, Y. W., Wang, L., Tian, J. Q., & Sun, X. P. (2011). Nucleic acid detection using carbon nanoparticles as a fluorescent sensing platform. *Chemical Communications*, *47*(3), 961-963. https://doi.org/10.1039/c0cc04326e

Li, H. T., Deng, Y. D., Liu, Y. D., Zeng, X., Wiley, D., & Huang, J. (2019). Carbon quantum dots and carbon layer double protected cuprous oxide for efficient visible light CO_2 reduction. *Chemical Communications*, *55*(30), 4419-4422. https://doi.org/10.1039/c9cc00830f

Li, H. T., He, X. D., Kang, Z. H., Huang, H., Liu, Y., Liu, J. L., Lian, S. Y., Tsang, C. H. A., Yang, X. B., & Lee, S. T. (2010). Water-Soluble Fluorescent Carbon Quantum Dots and Photocatalyst Design. *Angewandte Chemie-International Edition*, *49*(26), 4430-4434. https://doi.org/10.1002/anie.200906154

Lim, S. Y., Shen, W., & Gao, Z. (2015). Carbon quantum dots and their applications. *Chemical Society Reviews*, *44*(1), 362-381. https://doi.org/10.1039/c4cs00269e

Liu, M. L., Xu, Y. H., Niu, F. S., Gooding, J. J., & Liu, J. Q. (2016). Carbon quantum dots directly generated from electrochemical oxidation of graphite electrodes in alkaline alcohols and the applications for specific ferric ion detection and cell imaging. *Analyst*, *141*(9), 2657-2664. https://doi.org/10.1039/c5an02231b

Liu, R. H., Li, H. T., Kong, W. Q., Liu, J., Liu, Y., Tong, C. Y., Zhang, X., & Kang, Z. H. (2013). Ultra-sensitive and selective Hg^{2+} detection based on fluorescent carbon dots. *Materials Research Bulletin*, *48*(7), 2529-2534. https://doi.org/10.1016/j.materresbull.2013.03.015

Mandal, T., Mishra, S. R., Singh, K., Agarwalla, H., Masto, R. E., Kumar, M., & Singh, V. (2023). Fluorescent carbon nanomaterials from coal and its derivatives: structure, properties, and applications. *Journal of Nanoparticle Research*, *25*(6). https://doi.org/10.1007/s11051-023-05780-9

Mintz, K. J., Zhou, Y. Q., & Leblanc, R. M. (2019). Recent development of carbon quantum dots regarding their optical properties, photoluminescence mechanism, and core structure. *Nanoscale*, *11*(11), 4634-4652. https://doi.org/10.1039/c8nr10059d

Mondal, T. K., Mondal, S., Ghorai, U. K., & Saha, S. K. (2019). White light emitting lanthanide based carbon quantum dots as toxic Cr (VI) and pH sensor. *Journal of Colloid And Interface Science*, *553*, 177-185. https://doi.org/10.1016/j.jcis.2019.06.009

Peng, H., & Travas-Sejdic, J. (2009). Simple Aqueous Solution Route to Luminescent Carbogenic Dots from Carbohydrates. *Chemistry of Materials*, *21*(23), 5563-5565. https://doi.org/10.1021/cm901593y

Prazyan;, T. L., & Dyagilev;, D. V. (2021). The Kuzbass Basin coals as a raw material for the preparation of carbon quantum dots. *Journal of Physics: Conference Series*, *1749*, 012046. https://doi.org/doi:10.1088/1742-6596/1749/1/012046

Qu, Q., Zhu, A. W., Shao, X. L., Shi, G. Y., & Tian, Y. (2012). Development of a carbon quantum dots-based fluorescent Cu^{2+} probe suitable for living cell imaging. *Chemical Communications*, *48*(44), 5473-5475. https://doi.org/10.1039/c2cc31000g

Qu, S. N., Chen, H., Zheng, X. M., Cao, J. S., & Liu, X. Y. (2013). Ratiometric fluorescent nanosensor based on water soluble carbon nanodots with multiple sensing capacities. *Nanoscale*, *5*(12), 5514-5518. https://doi.org/10.1039/c3nr00619k

Qu, S. N., Wang, X. Y., Lu, Q. P., Liu, X. Y., & Wang, L. J. (2012). A Biocompatible Fluorescent Ink Based on Water-Soluble Luminescent Carbon Nanodots. *Angewandte Chemie-International Edition*, *51*(49), 12215-12218. https://doi.org/10.1002/anie.201206791

Ran, Y., Wang, S. Y., Yin, Q. Y., Wen, A. L., Peng, X. X., Long, Y. F., & Chen, S. (2020). Green synthesis of fluorescent carbon dots using chloroplast dispersions as precursors and application for Fe^{3+} ion sensing. *Luminescence*, *35*(6), 870-876. https://doi.org/10.1002/bio.3794

Rawat, P., Nain, P., Sharma, S., Sharma, P. K., Malik, V., Majumder, S., Verma, V. P., Rawat, V., & Rhyee, J. S. (2023). An overview of synthetic methods and applications of photoluminescence properties of carbon quantum dots. *Luminescence*, *38*(7), 845-866. https://doi.org/10.1002/bio.4255

Saikia, M., Hower, J. C., Das, T., Dutta, T., & Saikia, B. K. (2019). Feasibility study of preparation of carbon quantum dots from Pennsylvania anthracite and Kentucky bituminous coals. *Fuel*, *243*, 433-440. https://doi.org/10.1016/j.fuel.2019.01.151

Sciortino, A., Cannizzo, A., & Messina, F. (2018). Carbon Nanodots: A Review—From the Current Understanding of the Fundamental Photophysics to the Full Control of the Optical Response. *C*, *4*(4), 67-67. https://doi.org/10.3390/c4040067

Sikiru, S., Oladosu, T. L., Kolawole, S. Y., Mubarak, L. A., Soleimani, H., Afolabi, L. O., & Toyin, A. O. O. (2023). Advance and prospect of carbon quantum dots synthesis for energy conversion and storage application: A comprehensive review. *Journal of Energy Storage*, *60*. https://doi.org/10.1016/j.est.2022.106556

Sun, Y. P., Zhou, B., Lin, Y., Wang, W., Fernando, K. A. S., Pathak, P., Meziani, M. J., Harruff, B. A., Wang, X., Wang, H., Luo, P. G., Yang, H., Kose, M. E., Chen, B., Veca, L. M., & Xie, S. Y. (2006). Quantum-sized carbon dots for bright and colorful photoluminescence. *Journal of the American Chemical Society*, *128*(24), 7756-7757. https://doi.org/10.1021/ja062677d

Thambiraj, S., & Shankaran, D. R. (2016). Green synthesis of highly fluorescent carbon quantum dots from sugarcane bagasse pulp. *Applied Surface Science*, *390*, 435-443. https://doi.org/10.1016/j.apsusc.2016.08.106

Tian, J., Liu, R. Y., Zhen, L., Yu, C. L., & Liu, M. C. (2017). Boosting the photocatalytic performance of Ag_2CO_3 crystals in phenol degradation coupling with trace N-CQDs. *Chinese Journal of Catalysis*, *38*(12), 1999-2008. https://doi.org/10.1016/S1872-2067(17)62926-7

Wang, L., Chen, X., Lu, Y., Liu, C., & Yang, W. (2015). Carbon quantum dots displaying dual-wavelength photoluminescence and electrochemiluminescence prepared by high-energy ball milling. *Carbon*, *94*, 472-478. https://doi.org/10.1016/j.carbon.2015.06.084

Wang, Y. F., & Hu, A. G. (2014). Carbon quantum dots: synthesis, properties and applications. *Journal of Materials Chemistry C*, *2*(34), 6921-6939. https://doi.org/10.1039/c4tc00988f

Xie, S. L., Su, H., Wei, W. J., Li, M. Y., Tong, Y. X., & Mao, Z. W. (2014). Remarkable photoelectrochemical performance of carbon dots sensitized TiO_2 under visible light irradiation. *Journal of Materials Chemistry A*, *2*(39), 16365-16368. https://doi.org/10.1039/c4ta03203a

Xu, G. (1992). *The effects of chain segment motion on ionic diffusion in solid polymer electrolytes* (01672738/92). (Solid State Ionics, Issue.

Xu, J., Xue, Y., Cao, J., Wang, G., Li, Y., Wang, W., & Chen, Z. (2016). Carbon quantum dots/nickel oxide (CQDs/NiO) nanorods with high capacitance for supercapacitors. *RSC Advances*, *6*(7), 5541-5546. https://doi.org/10.1039/c5ra24192h

Xu, K. J., Wang, R. T., Xu, A. F., Chen, J. Y., & Xu, G. (2020). Hysteresis and Instability Predicted in Moisture Degradation of Perovskite Solar Cells. *ACS Applied Materials and Interfaces*, *12*(43), 48882-48889. https://doi.org/10.1021/acsami.0c17323

Xu, X. Y., Ray, R., Gu, Y. L., Ploehn, H. J., Gearheart, L., Raker, K., & Scrivens, W. A. (2004). Electrophoretic analysis and purification of fluorescent single-walled carbon nanotube fragments. *Journal of the American Chemical Society*, *126*(40), 12736-12737. https://doi.org/10.1021/ja040082h

Yadav, P. K., Chandra, S., Kumar, V., Kumar, D., & Hasan, S. H. (2023). Carbon Quantum Dots: Synthesis, Structure, Properties, and Catalytic Applications for Organic Synthesis. *Catalysts*, *13*(2). https://doi.org/10.3390/catal13020422

Yang, M. J., Shi, J. X., Yin, Y., & Shi, C. G. (2021). Preparation of Carbon Nanodots with Ultraviolet Emission by Pulsed Laser Ablation. *Physica Status Solidi B-Basic Solid State Physics*, *258*(10). https://doi.org/10.1002/pssb.202100110

Yang, S. T., Cao, L., Luo, P. G. J., Lu, F. S., Wang, X., Wang, H. F., Meziani, M. J., Liu, Y. F., Qi, G., & Sun, Y. P. (2009). Carbon Dots for Optical Imaging in Vivo. *Journal of the American Chemical Society*, *131*(32), 11308. https://doi.org/10.1021/ja904843x

Ye, R., Xiang, C., Lin, J., Peng, Z., Huang, K., Yan, Z., Cook, N. P., Samuel, E. L. G., Hwang, C. C., Ruan, G., Ceriotti, G., Raji, A. R. O., Martí, A. A., & Tour, J. M. (2013). Coal as an abundant source of graphene quantum dots. *Nature Communications*, *4*, 1-7. https://doi.org/10.1038/ncomms3943

Youh, M. J., Chung, M. C., Tai, H. C., Chen, C. Y., & Li, Y. Y. (2021). Fabrication of carbon quantum dots via ball milling and their application to bioimaging. *Mendeleev Communications*, *31*(5), 647-650. https://doi.org/10.1016/j.mencom.2021.09.018

Younis, M. R., He, G., Lin, J., & Huang, P. (2020). Recent Advances on Graphene Quantum Dots for Bioimaging Applications. *Frontiers in Chemistry*, *8*(June), 1-25. https://doi.org/10.3389/fchem.2020.00424

Zhang, B., Chen, H., Huang, Y., Lau, W.-M., & Zhou, D. (2023). Solar-driven evaporation device based on coal-derived nanomaterials for efficient and stable desalination. *Chemical Engineering Journal*, *468*. https://doi.org/10.1016/j.cej.2023.143689

Zhang, B., Chen, H., Huang, Y., Liu, Z., Lau, W.-M., He, X., & Zhou, D. (2024). A coal-based multifunctional membrane for solar-driven seawater desalination and power generation. *Desalination*, *578*. https://doi.org/10.1016/j.desal.2024.117451

Zhang, B., Liu, C. Y., & Liu, Y. (2010). A Novel One-Step Approach to Synthesize Fluorescent Carbon Nanoparticles. *European Journal of Inorganic Chemistry*(28), 4411-4414. https://doi.org/10.1002/ejic.201000622

Zhang, H. C., Ming, H., Lian, S. Y., Huang, H., Li, H. T., Zhang, L. L., Liu, Y., Kang, Z. H., & Lee, S. T. (2011). Fe_2O_3/carbon quantum dots complex photocatalysts and their enhanced photocatalytic activity under visible light. *Dalton Transactions*, *40*(41), 10822-10825. https://doi.org/10.1039/c1dt11147g

Zhang, L., Yang, X., Yin, Z., & Sun, L. (2022). A review on carbon quantum dots: Synthesis, photoluminescence mechanisms and applications. *Luminescence*, *37*(10), 1612-1638. https://doi.org/10.1002/bio.4351

Zhang, W. F., Yu, S. F., Fei, L. F., Jin, L. M., Pan, S. S., & Lin, P. (2015). Large-area color controllable remote carbon white-light light-emitting diodes. *Carbon*, *85*, 344-350. https://doi.org/10.1016/j.carbon.2014.12.107

Zhang, Y. H., Zhao, Y. Y., Xu, Z. L., Su, H. M., Bian, X. Y., Zhang, S. S., Dong, X. P., Zeng, L. X., Zeng, T., Feng, M. B., Li, L. X. Y., & Sharma, V. K. (2020). Carbon quantum dots implanted CdS nanosheets: Efficient visible-light-driven photocatalytic reduction of Cr(VI) under saline conditions. *Applied Catalysis B-Environmental*, *262*. https://doi.org/10.1016/j.apcatb.2019.118306

Zhao, D., Chen, C. X., Lu, L. X., Yang, F., & Yang, X. R. (2015). A dual-mode colorimetric and fluorometric "light on" sensor for thiocyanate based on fluorescent carbon dots and unmodified gold nanoparticles. *Analyst*, *140*(24), 8157-8164. https://doi.org/10.1039/c5an01926e

Zhao, F. X., Li, X. Y., Zuo, M. X., Liang, Y. S., Qin, P. F., Wang, H., Wu, Z. B., Luo, L., Liu, C., & Leng, L. J. (2023). Preparation of photocatalysts decorated by carbon quantum dots (CQDs) and their applications: A review. *Journal of Environmental Chemical Engineering*, *11*(2). https://doi.org/10.1016/j.jece.2023.109487

Zhao, H., Yu, X. T., Li, C. F., Yu, W. B., Wang, A. G., Hu, Z. Y., Larter, S., Li, Y., Kibria, M. G., & Hu, J. G. (2022). Carbon quantum dots modified TiO_2 composites for hydrogen production and selective glucose photoreforming. *Journal of Energy Chemistry*, *64*, 201-208. https://doi.org/10.1016/j.jechem.2021.04.033

Zheng, M., Liu, S., Li, J., Qu, D., Zhao, H. F., Guan, X. G., Hu, X. L., Xie, Z. G., Jing, X. B., & Sun, Z. C. (2014). Integrating Oxaliplatin with Highly Luminescent Carbon Dots: An Unprecedented Theranostic Agent for Personalized Medicine. *Advanced Materials*, *26*(21), 3554-3560. https://doi.org/10.1002/adma.201306192

Zhou, J. G., Booker, C., Li, R. Y., Zhou, X. T., Sham, T. K., Sun, X. L., & Ding, Z. F. (2007). An electrochemical avenue to blue luminescent nanocrystals from multiwalled carbon nanotubes (MWCNTs). *Journal of the American Chemical Society*, *129*(4), 744-745. https://doi.org/10.1021/ja0669070

Zhou, L., Lin, Y. H., Huang, Z. Z., Ren, J. S., & Qu, X. G. (2012). Carbon nanodots as fluorescence probes for rapid, sensitive, and label-free detection of Hg^{2+} and biothiols in complex matrices. *Chemical Communications*, *48*(8), 1147-1149. https://doi.org/10.1039/c2cc16791c

Zhu, S. J., Song, Y. B., Zhao, X. H., Shao, J. R., Zhang, J. H., & Yang, B. (2015). The photoluminescence mechanism in carbon dots (graphene quantum dots, carbon nanodots, and polymer dots): current state and future perspective. *Nano Research*, *8*(2), 355-381. https://doi.org/10.1007/s12274-014-0644-3

Zhu, S. J., Wang, L., Li, B., Song, Y. B., Zhao, X. H., Zhang, G. Y., Zhang, S. T., Lu, S., Zhang, J. H., Wang, H. Y., Sun, H. B., & Yang, B. (2014). Investigation of photoluminescence mechanism of graphene quantum dots and evaluation of their assembly into polymer dots. *Carbon*, *77*, 462-472. https://doi.org/10.1016/j.carbon.2014.05.051

Zhu, X., Sun, J., Yuan, S., Li, N., Qiu, Z., Jia, J., Liu, Y., Dong, J., Lv, P., & Cao, B. (2019). Efficient and stable planar perovskite solar cells with carbon quantum dots-doped PCBM electron transport layer. *New Journal of Chemistry*, *43*(18), 7130-7135. https://doi.org/10.1039/c8nj06146g

Zhu, Y. R., Ji, X. B., Pan, C. C., Sun, Q. Q., Song, W. X., Fang, L. B., Chen, Q. Y., & Banks, C. E. (2013). A carbon quantum dot decorated RuO_2 network: outstanding supercapacitances under ultrafast charge and discharge. *Energy & Environmental Science*, *6*(12), 3665-3675. https://doi.org/10.1039/c3ee41776j

7 Appendix

7.1 Determination of s value

To determine the appropriate s value, the plots of average value of x square against T, obtained at s equals 0.15, 0.25, 0.35, 0.45, 0.55, 0.65, 0.75, and 0.85, and the corresponding simulated diagrams are shown in **Figure 7.1-7.8**.

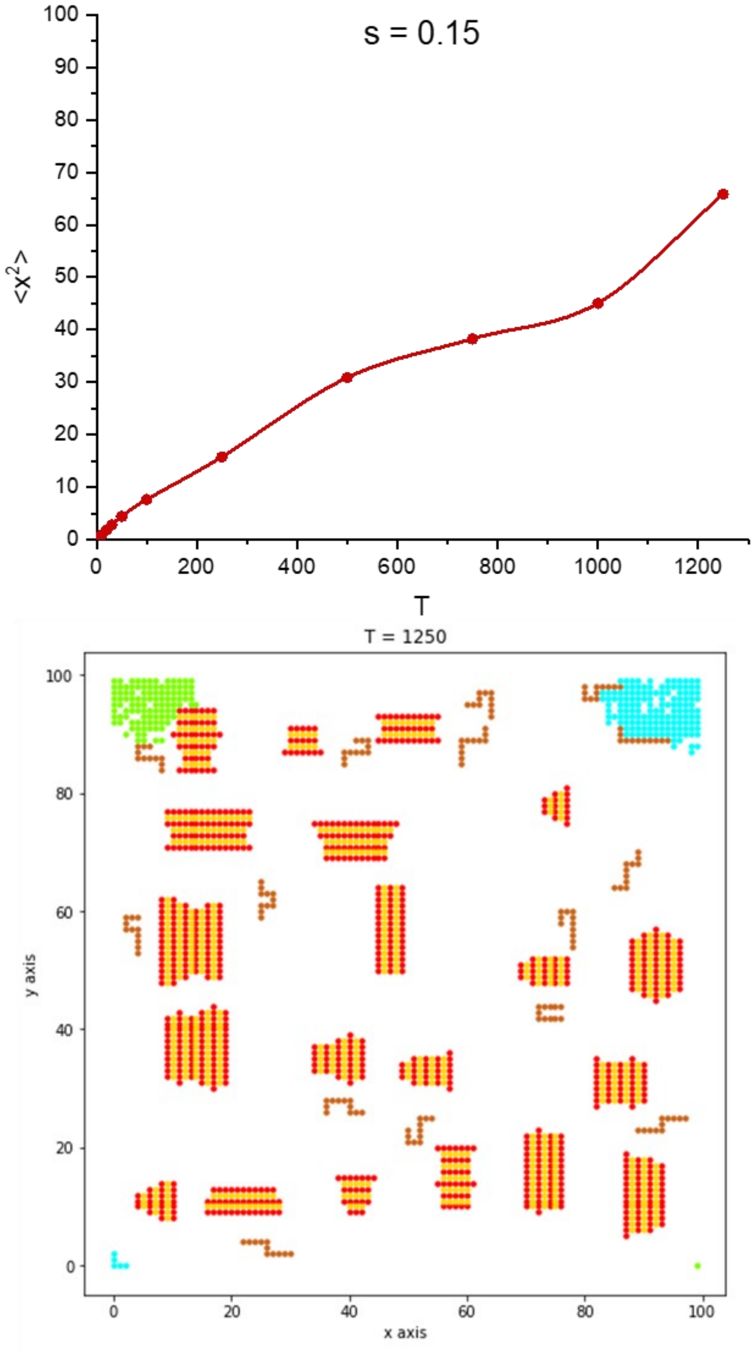

Figure 7.1 The plot of $<x^2>$ vs T with s = 0.15 (up). The simulated diagram of the strain propagation in 100×100 square at T = 1250 (down).

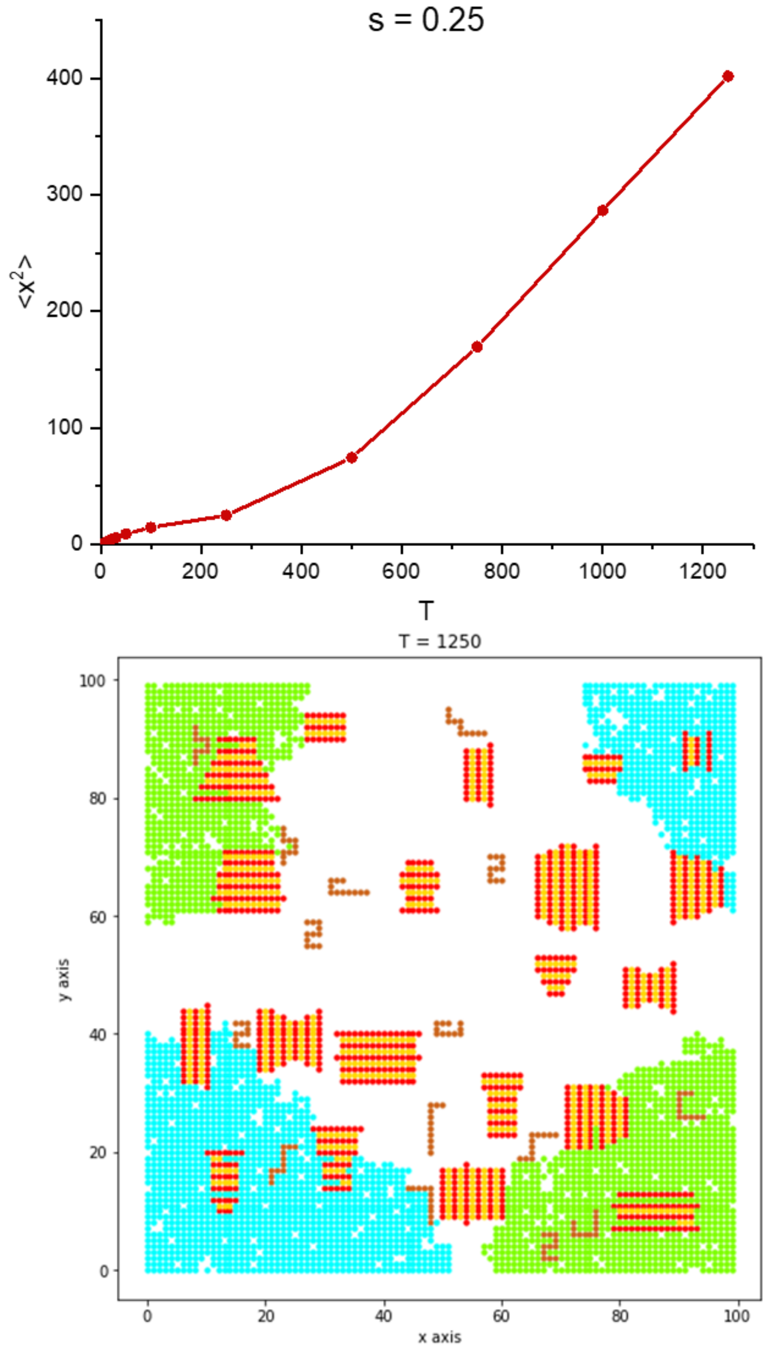

Figure 7.2 The plot of <x^2> vs T with s = 0.25 (up). The simulated diagram of the strain propagation in 100×100 square at T = 1250 (down).

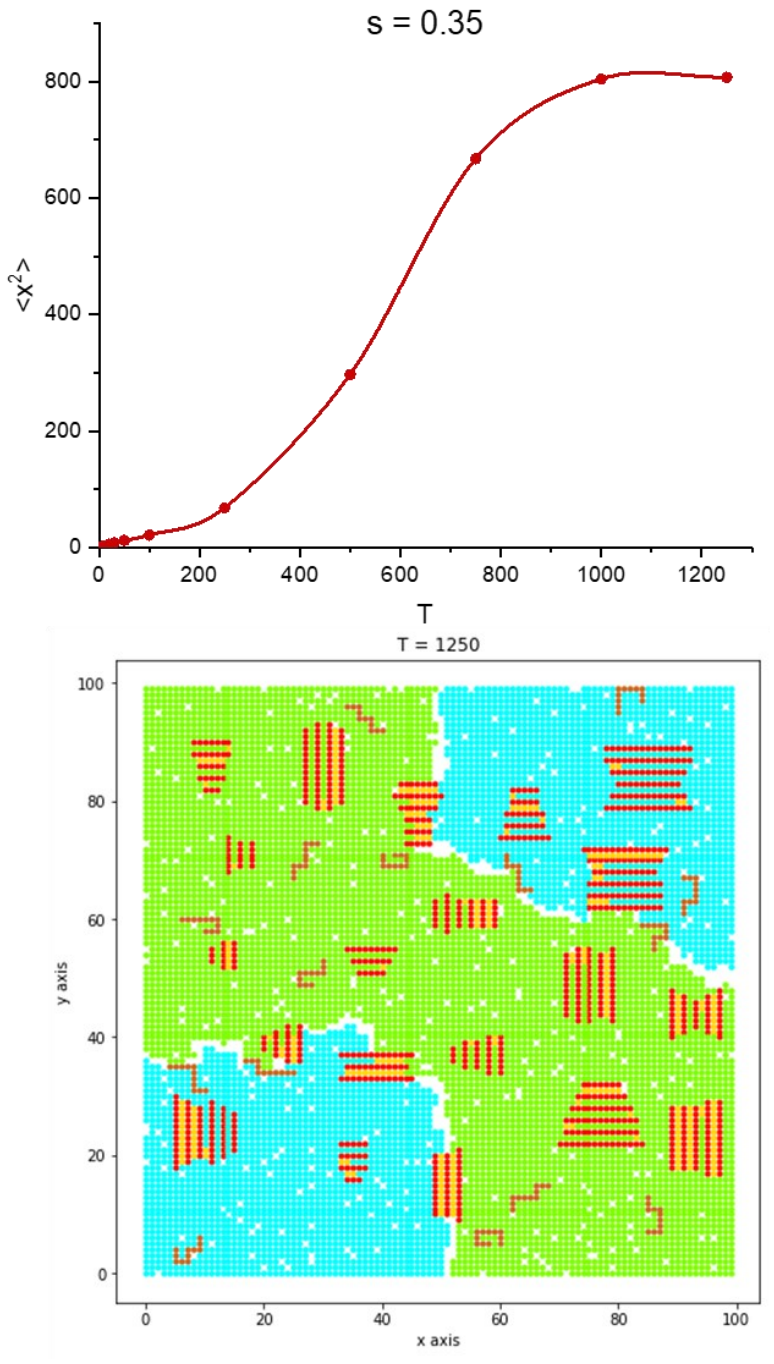

Figure 7.3 The plot of <x^2> vs T with s = 0.35 (up). The simulated diagram of the strain propagation in 100×100 square at T = 1250 (down).

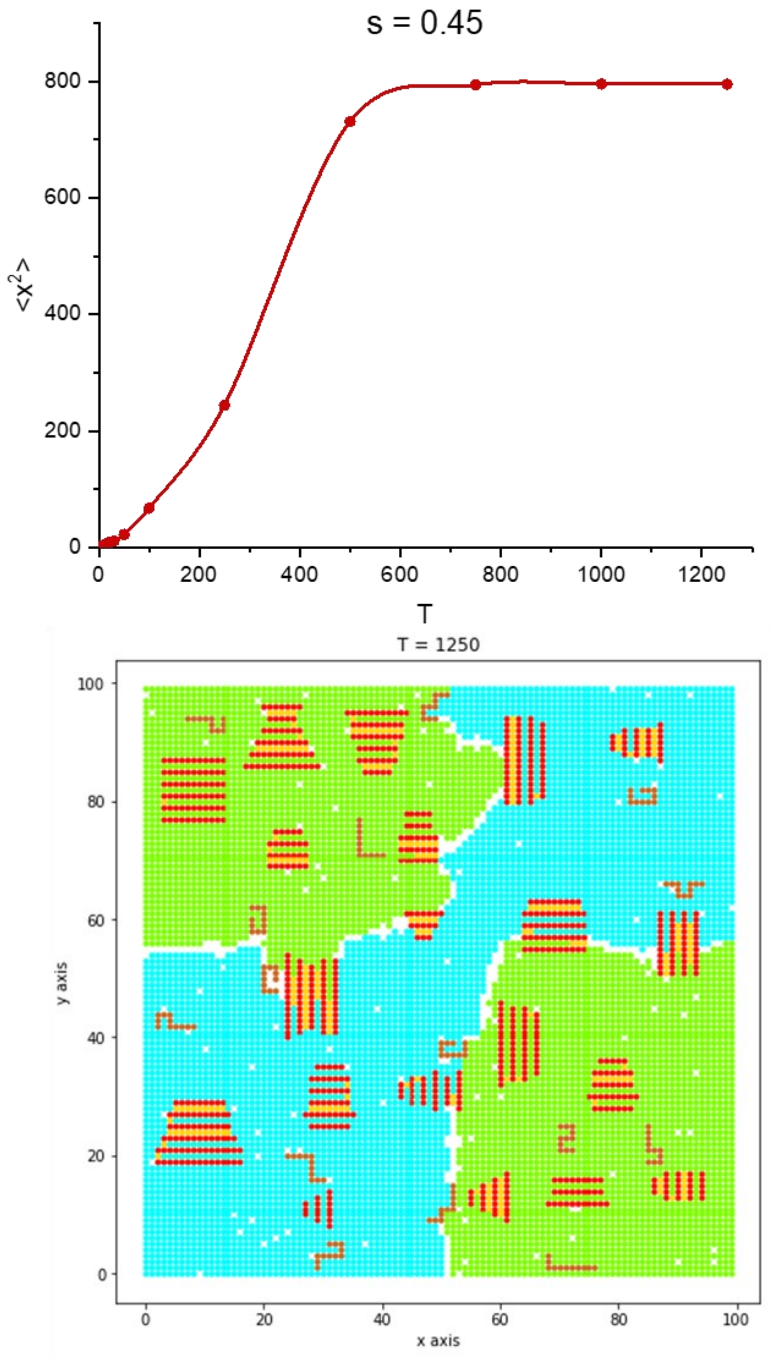

Figure 7.4 The plot of $<x^2>$ vs T with s = 0.45 (up). The simulated diagram of the strain propagation in 100×100 square at T = 1250 (down).

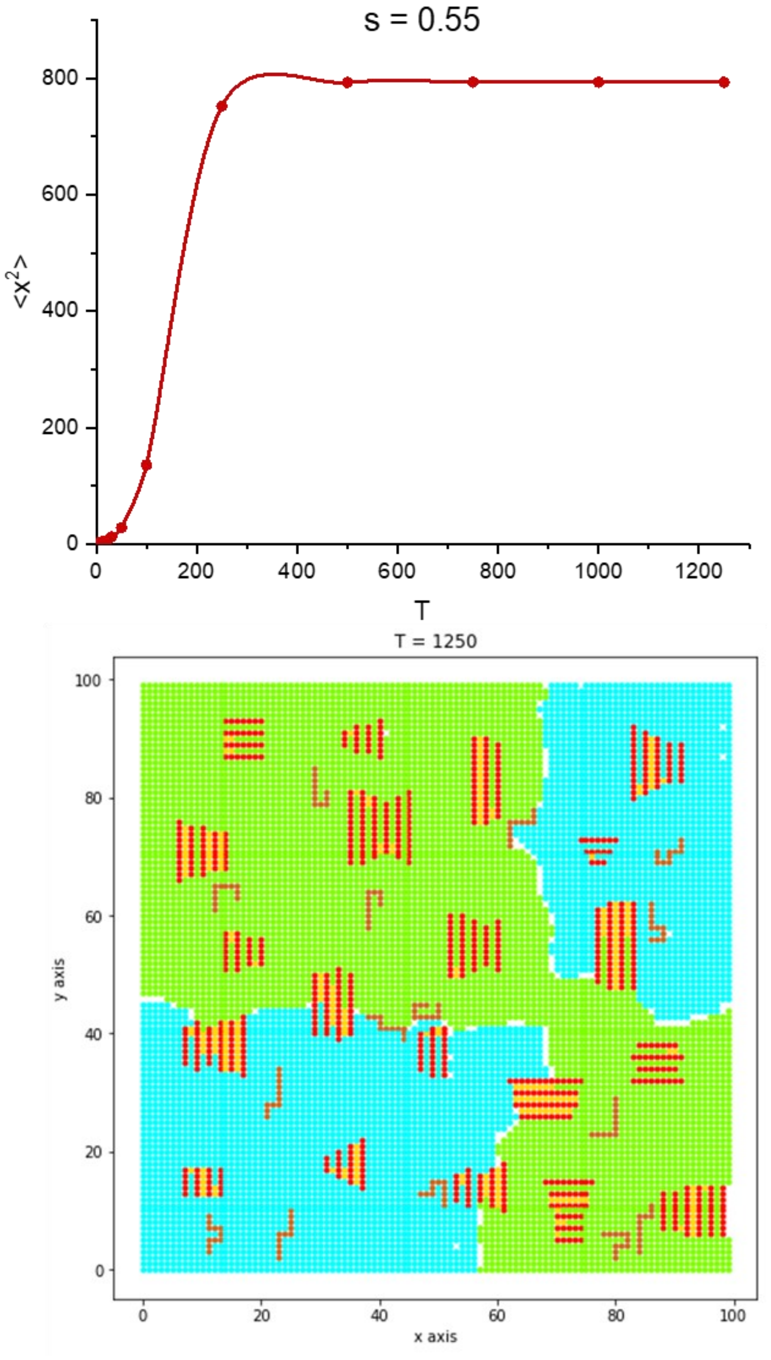

Figure 7.5 The plot of <x^2> vs T with s = 0.55 (up). The simulated diagram of the strain propagation in 100×100 square at T = 1250 (down).

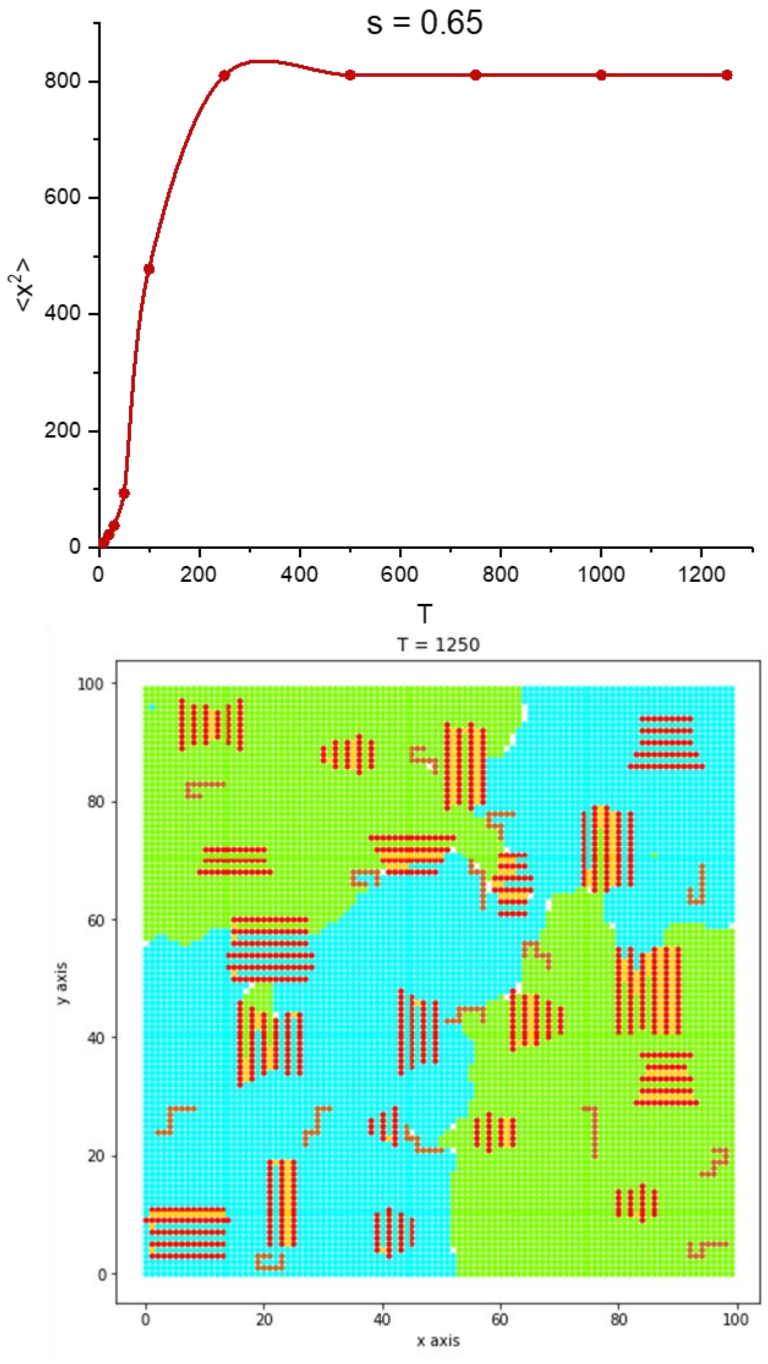

Figure 7.6 The plot of <x^2> vs T with s = 0.65 (up). The simulated diagram of the strain propagation in 100×100 square at T = 1250 (down).

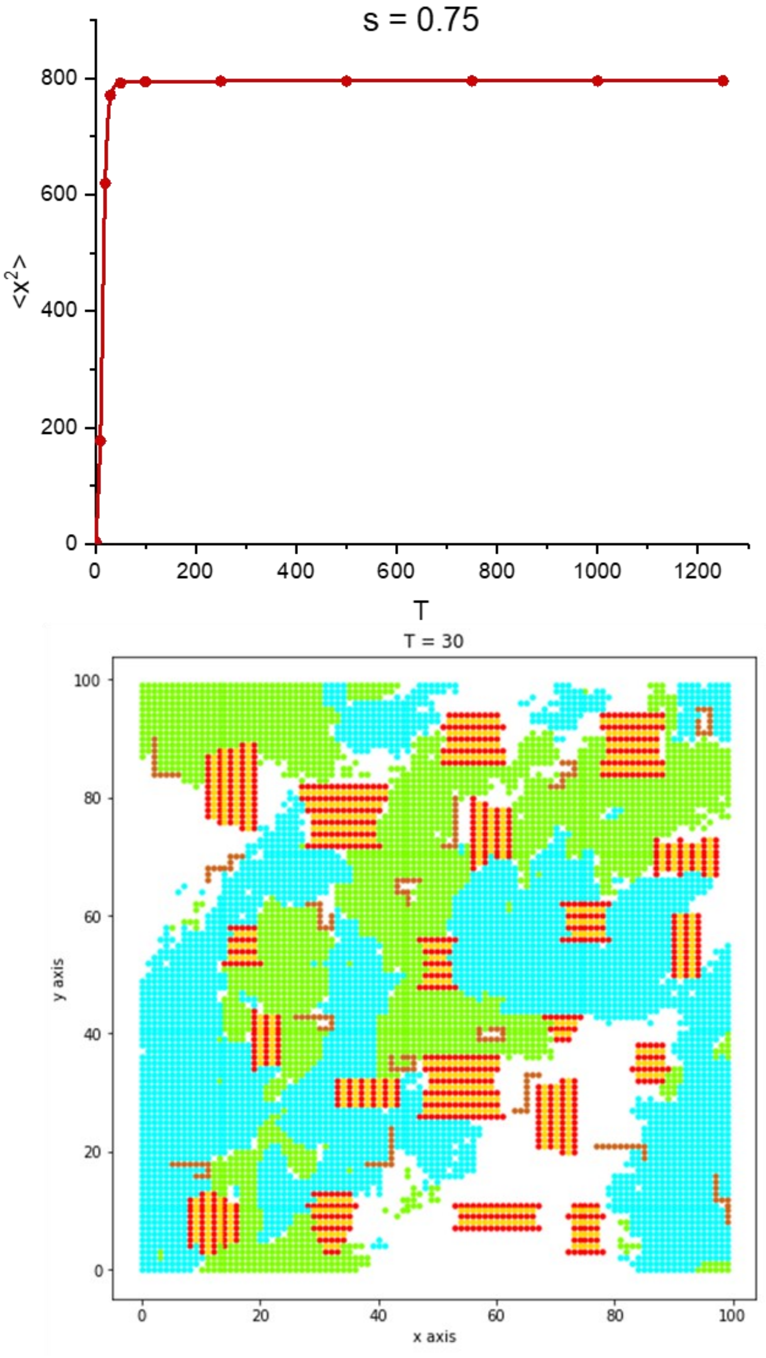

Figure 7.7 The plot of $<x^2>$ vs T with s = 0.75 (up). The simulated diagram of the strain propagation in 100×100 square at T = 30 (down).

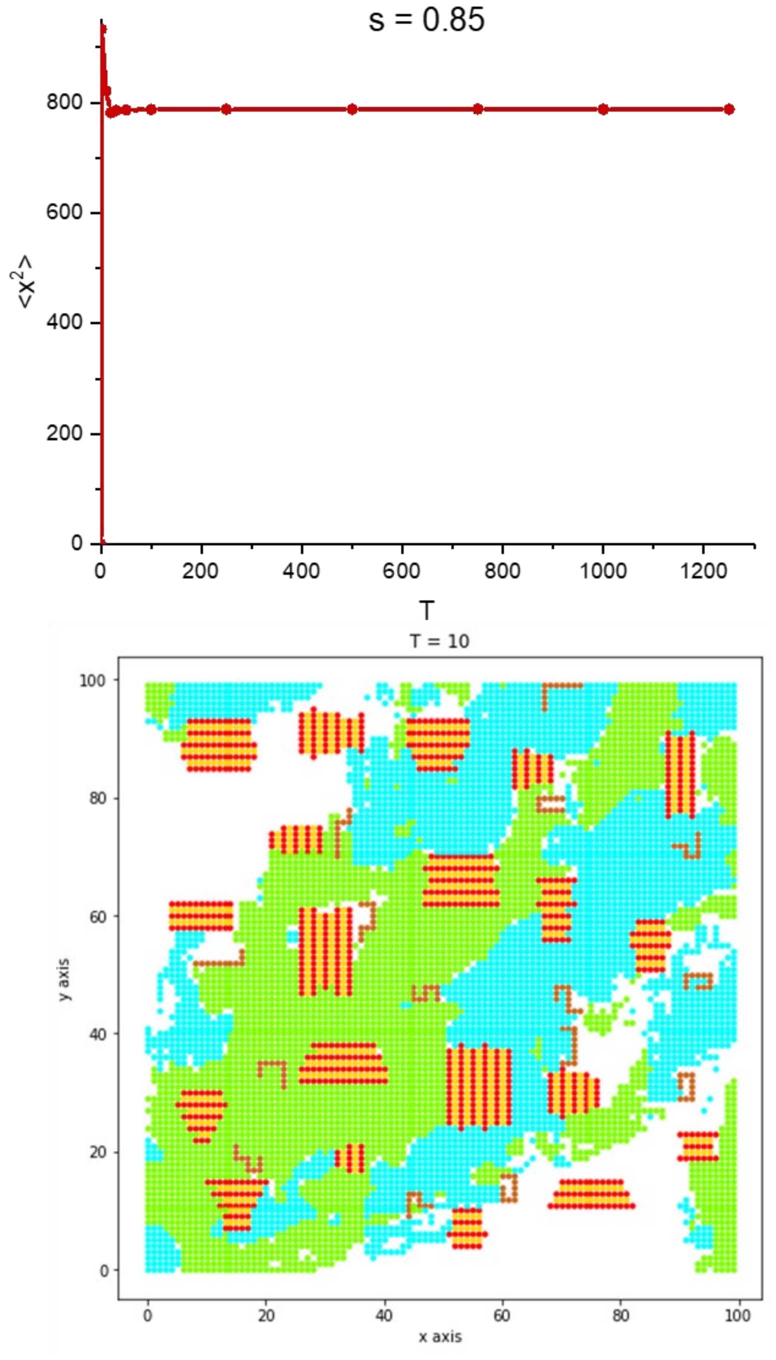

Figure 7.8 The plot of <x^2> vs T with s = 0.85 (up). The simulated diagram of the strain propagation in 100×100 square at T = 10 (down).

7.2 <x^2> for anthracite and bituminous coal

The plots of average x^2 against T for anthracite and bituminous coal particles simulated in section 3.2 are shown in **Figure 7.9** and **Figure 7.10**, respectively.

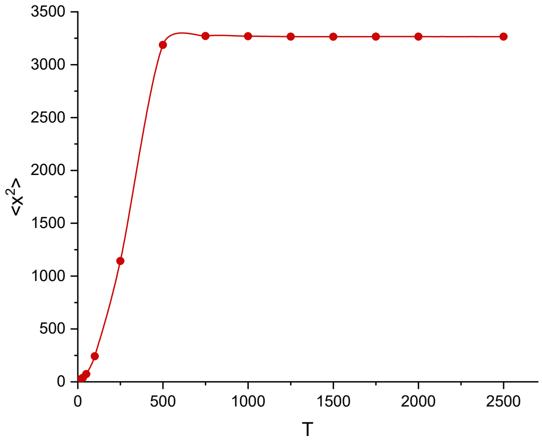

Figure 7.9 The plot of <x^2> vs T for simulated anthracite coal particle with s = 0.55.

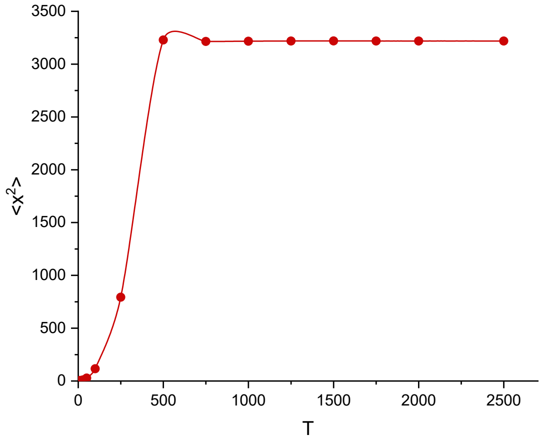

Figure 7.10 The plot of <x^2> vs T for simulated bituminous coal particle with s = 0.55.

7.3 Program code

Program of anthracite coal, modified from Kevin Xu (Xu et al., 2020). The programs were written in the Python language and run with Spyder 5.1.5, which was launched through Anaconda Navigator.

```
import numpy as np

import csv

import random

import matplotlib.pyplot as plt

def snapshot(title):

  green_x = []

  blue_x = []

  green_y = []

  blue_y =[]

  for i in range(m):

      for j in range(n):

          if (P[i][j]>=1):
```

```
                blue_x.append(i)
                blue_y.append(j)
            elif (P[i][j]<=-1):
                green_x.append(i)
                green_y.append(j)
    fig=plt.figure()
    ax=fig.add_axes([0,0,2,2])
    ax.scatter(yelx, yely, color = '#FFD700', s=5)
    ax.scatter(green_x, green_y, color='#7FFF00', s=5)
    ax.scatter(blue_x, blue_y, color='#01FFFF', s=5)
    ax.scatter(x_sp3, y_sp3, color = '#CD661D', s=5)
    ax.scatter(redx, redy, color = 'r', s=5)
    ax.set_xlabel('x axis')
    ax.set_ylabel('y axis')
    ax.set_title(title)
    ax.set_aspect('equal')
```

```
    plt.show()

def rand():

    return random.random()

m = 200

n = 200

P = np.zeros((m,n))

P_i = 0.0

P[0][0]=1.0

P[m-1][n-1]=1.0

P[0][n-1]=-1.0

P[m-1][0]=-1.0

W = []

M = []

for i in range(m):

    W.append([None]*n)

    M.append([None]*n)
```

```
p = 0.5

q = 0.7

for x in range(m):

    for y in range(n):

        li = []

        for i in range(4):

            if rand() < p:

                li.append(q)

            else:

                li.append(0)

        M[x][y] = li[:]

        W[x][y] = [rand(),rand(),rand(),rand()]

lmin = 7

lmax= 15

x_gr = []

y_gr = []
```

```
x_gr.append(random.randint(lmax+1,m-lmax))

y_gr.append(random.randint(lmax+1,n-lmax))

n_sp2 = 15

i=1

while i<n_sp2:

    x= random.randint(lmax+1,m-lmax)

    y= random.randint(lmax+1,n-lmax)

    flag1 = False

    for j in range (i):

        if (x > x_gr[j]+2*lmax+2) or (x < x_gr[j]-2*lmax+2) or (y > y_gr[j]+2*lmax+2) or (y
< y_gr[j]-2*lmax+2):

            flag1=True

        else:

            flag1=False

            break

    if (flag1):
```

```
        x_gr.append(x)

        y_gr.append(y)

        i += 1

n_layer = np.empty(1000,int)

red1x = []

yel1x = []

red0x = []

yel0x= []

red1y = []

yel1y= []

red0y = []

yel0y = []

sum=0

for i in range (0,n_sp2):

    n_layer[i] = random.randint(3, 5)

    ori= random.randint(0,1)
```

```
if (ori == 1):
    for y in range (y_gr[i]-n_layer[i], y_gr[i]+n_layer[i]+1,2):
        if (y==y_gr[i]-n_layer[i]):
            length = random.randint(lmin,lmax+1)
            for x in range (x_gr[i]-length, x_gr[i]+length+1):
                red1x.append(x)
                red1y.append(y)
        else:
            edg = random.randint(-1,1)
            while length+edg<lmin+1 or length+edg>lmax+1:
                edg = random.randint(-1,1)
            length = length + edg
            for x in range (x_gr[i]-length, x_gr[i]+length+1):
                red1x.append(x)
                red1y.append(y)
            if (edg == 1):
```

```
                for x in range (x_gr[i]-length+1, x_gr[i]+length):
                    yel1x.append(x)
                    yel1y.append(y-1)
            else:
                for x in range (x_gr[i]-length, x_gr[i]+length+1):
                    yel1x.append(x)
                    yel1y.append(y-1)
    else:
        for x in range (x_gr[i]-n_layer[i], x_gr[i]+n_layer[i]+1,2):
            if (x==x_gr[i]-n_layer[i]):
                length = random.randint(lmin,lmax+1)
                for y in range (y_gr[i]-length, y_gr[i]+length+1):
                    red0x.append(x)
                    red0y.append(y)
            else:
                edg = random.randint(-1,1)
```

```
        while length+edg<lmin+1 or length+edg>lmax+1:
            edg = random.randint(-1,1)
        length = length + edg
        for y in range (y_gr[i]-length, y_gr[i]+length+1):
            red0x.append(x)
            red0y.append(y)
        if (edg == 1):
            for y in range (y_gr[i]-length+1, y_gr[i]+length):
                yel0x.append(x-1)
                yel0y.append(y)
        else:
            for y in range (y_gr[i]-length, y_gr[i]+length+1):
                yel0x.append(x-1)
                yel0y.append(y)
redx = red1x + red0x
redy = red1y + red0y
```

```
yelx = yel1x + yel0x

yely = yel1y + yel0y

red1 = list(zip(red1x,red1y))

yel1 = list(zip(yel1x,yel1y))

red0 = list(zip(red0x,red0y))

yel0 = list(zip(yel0x,yel0y))

red = list(zip(redx,redy))

yel = list(zip(yelx,yely))

print('% of crystal:', (len(redx)+len(yelx))/(m*n))

for x in range (m):

    for y in range (n):

        if (x,y) in red1:

            W[x][y]=[0.0]*4

        elif (x,y) in yel1:

            W[x][y][1] = random.uniform(0.2,0.5)

            W[x][y][3] = random.uniform(0.2,0.5)
```

```
            W[x][y][0] = 0.0

            W[x][y][2] = 0.0

        elif (x,y) in red0:

            W[x][y] = [0.0]*4

        elif (x,y) in yel0:

            W[x][y][0] = random.uniform(0.2,0.5)

            W[x][y][2] = random.uniform(0.2,0.5)

            W[x][y][1] = 0.0

            W[x][y][3] = 0.0

print('sp2 finished')

n_sp3 = 10

x_sp3 =[]

y_sp3 =[]

x_head = np.zeros(n_sp3)

y_head = np.zeros(n_sp3)

i=0
```

```
while i<n_sp3:

    x= random.randint(1,m)

    y= random.randint(1,n)

    flag2 = False

    flag3 = False

    if ((x,y) in red) and ((x,y) in yel):

        flag2 = False

    elif (((x-1,y-1) in red) or ((x-1,y+1) in red) or ((x+1,y-1) in red) or ((x+1,y+1) in red) or

          ((x-1,y-1) in yel) or ((x-1,y+1) in yel) or ((x+1,y-1) in yel) or ((x+1,y+1) in yel)):

        flag2 = False

    else:

        flag2 = True

    if i == 0:

        flag3 = True

    else:

        for j in range (0,i):
```

```
            if ((x-x_head[j])**2+(y-y_head[j])**2 >=100):

                flag3 = True

            else:

                flag3 = False

                break

    if (flag2 and flag3):

        x_head[i]=x

        y_head[i]=y

        i += 1

h=0

for k in range (n_sp3):

    x_sp3.append(x_head[k])

    y_sp3.append(y_head[k])

    i=1

    while i < 20:

        step = random.randint(0,3)
```

```
if (step == 0):

   x1 = x_sp3[h+i-1]

   x2 = x_sp3[h+i-1]

   y1 = y_sp3[h+i-1]+1

   y2 = y_sp3[h+i-1]+2

elif (step == 1):

   x1 = x_sp3[h+i-1]+1

   x2 = x_sp3[h+i-1]+2

   y1 = y_sp3[h+i-1]

   y2 = y_sp3[h+i-1]

elif (step == 2):

   x1 = x_sp3[h+i-1]

   x2 = x_sp3[h+i-1]

   y1 = y_sp3[h+i-1]-1

   y2 = y_sp3[h+i-1]-2

else:
```

```
   x1 = x_sp3[h+i-1]-1

   x2 = x_sp3[h+i-1]-2

   y1 = y_sp3[h+i-1]

   y2 = y_sp3[h+i-1]

flag4 = False

flag5 = False

flag6 = False

for j in range (0,h+i):

   if (x1 == x_sp3[j] and y1 == y_sp3[j]) or (x2 == x_sp3[j] and y2 == y_sp3[j]):

      flag4 = False

      break

   else:

      flag4 = True

if ((x1,y1) in red) or ((x1,y1) in yel) or ((x2,y2) in red) or ((x2,y2) in yel):

   flag5 = False

elif (((x2-1,y2-1) in red) or ((x2-1,y2+1) in red) or ((x2+1,y2-1) in red) or
```

```
((x2+1,y2+1) in red) or
          ((x2-1,y2-1) in yel) or ((x2-1,y2+1) in yel) or ((x2+1,y2-1) in yel) or ((x2+1,y2+1) in yel)):
        flag5 = False
    else:
        flag5 = True
    if (x1 >= m or x1 <= 0) or (y1 >= n or y1 <= 0) or (x2 >= m or x2 <= 0) or (y2 >= n or y2 <= 0):
        flag6 = False
    else:
        flag6 = True
    if (flag4 and flag5 and flag6):
        x_sp3.append(x1)
        x_sp3.append(x2)
        y_sp3.append(y1)
        y_sp3.append(y2)
```

```
            i = i+2

    x = list(map(int,x_sp3))

    y = list(map(int,y_sp3))

    h = h+21

sp3 = list(zip(x_sp3,y_sp3))

for i in range(m):

    for j in range(n):

        if (i,j) in sp3:

            W[i][j]=[0.0]*4

print('sp3 finished')

'''

with open('scatter.csv',mode='w') as file:

    writer = csv.writer(file)

    writer.writerows((x_start, x_end, y_start, y_end, x_head, y_head, x_sp3, y_sp3))

'''

sz = 10
```

```
T = 2500

x_avg = []

vdw_break = []

for i in range(T):

    if i == 0:

        snapshot('T = 0')

    for x in range(m):

        for y in range(n):

            if (P[x][y]>=1) or (P[x][y]<=-1):

                W[x][y][:]=W[x][y][:]

            elif (x,y) in red1:

                W[x][y]=[0.0]*4

            elif (x,y) in yel1:

                W[x][y][1] = random.uniform(0.2,0.5)

                W[x][y][3] = random.uniform(0.2,0.5)

                W[x][y][0] = 0.0
```

```
    W[x][y][2] = 0.0

elif (x,y) in red0:

    W[x][y] = [0.0]*4

elif (x,y) in yel0:

    W[x][y][0] = random.uniform(0.2,0.5)

    W[x][y][2] = random.uniform(0.2,0.5)

    W[x][y][1] = 0.0

    W[x][y][3] = 0.0

elif (x,y) in sp3:

    W[x][y] = W[x][y]

else:

    if rand() < 0.5:

        W[x][y] = M[x][y][:]

        W[x][y][0] = 0.9

        W[x][y][2] = 0.9

    else:
```

```
            W[x][y] = M[x][y][:]

            W[x][y][1] = 0.9

            W[x][y][3] = 0.9

for x in range(m):

    for y in range(n):

        u = (y+1)%n

        d = (y-1)%n

        l = x-1

        r = x+1

        if x+1 == m:

            r = x

        if x-1 == -1:

            l = x

        if y+1 ==n:

            u = y

        if y-1 ==-1:
```

```
            d = y
          if (P[x][y]>=1) or (P[x][y]<=-1):
            P[x][y]=P[x][y]
          else:
            dP = P[x][u]*W[x][y][0] + P[r][y]*W[x][y][1] + P[x][d]*W[x][y][2] + P[l][y]*W[x][y][3] - P[x][y]*W[x][d][0] - P[x][y]*W[l][y][1] - P[x][y]*W[x][u][2] - P[x][y]*W[r][y][3]
            D = 0.55
            P[x][y] = P[x][y]+ D*dP
      if (i+1) in [1,10,20,30,50,100,250,500,750,1000,1250,1500,1750,2000,2500]:
        snapshot('T = ' + str(i+1))
        num = 0
        den = 0
        br = 0
        for x in range(0,m):
          x_summ = 0
```

```
      for y in range(n):

        x_summ += (P_i -abs(P[x][y]))

      if (x<m/2):

        num += x_summ*(x**2)

        den += x_summ

      else:

        num += x_summ*((m-1-x)**2)

        den += x_summ

    x_avg.append((num/den))

    for (a,b) in yel:

      if (P[a][b]>=1) or (P[a][b]<=-1):

        br+=1

    print((br/len(yelx)))

    vdw_break.append((br/len(yelx)))

  if (i+1)%100 == 0:

    print(i+1)
```

```
fig=plt.figure()

ax=fig.add_axes([0,0,1,1])

ax.scatter([1,10,20,30,50,100,250,500,750,1000,1250,1500,1750,2000, 2500], x_avg, color='#000000', s = sz)

ax.set_xlabel('T axis')

ax.set_ylabel('X squared avg axis')

ax.set_title('plot of <x^2> vs t')

plt.show()

fig=plt.figure()

ax=fig.add_axes([0,0,1,1])

ax.scatter([1,10,20,30,50,100,250,500,750,1000,1250,1500,1750,2000, 2500], vdw_break, color='#000000', s = sz)

ax.set_xlabel('T axis')

ax.set_ylabel('percentage of broken vdw bonds')

ax.set_title('percentage of broken vdw bonds vs t')

plt.show()
```

```
file_path = 'anthracite.txt'

with open(file_path, 'a') as file:

    file.write(','.join(map(str, vdw_break)) + '\n')
```